AERODYNAMIC INTERACTIONS OF NON-PLANAR ROTORS

A thesis submitted to the University of Manchester
for the degree of Doctor of Philosophy
in the Faculty of Science and Engineering

2017

By
Alexander Bennetts
School of Mechanical, Aerospace and Civil Engineering

Contents

Word Count: 20,000

List of Tables

List of Figures

Nomenclature

α	Effective angle of attack [rad]
δT	Inter-frame time
$\dot{m}$	Mass flow rate [kg/s]
ω	Rotational speed [rad/s]
ϕ	Induced angle of attack [rad]
ρ	Density [kg/m^3]
A_x	Cross sectional area [mm^2]
C_P	Coefficient of power
C_Q	Coefficient of torque
C_T	Coefficient of thrust
D	Rotor disc diameter [mm]
d	Rotor hub spacing [mm]
F_x	Force measured along X-axis [N]
F_y	Force measured along Y-axis [N]
F_z	Force measured along Z-axis [N]
m	Mass [kg]
N_b	Number of rotor blades
Q	Torque [N.m]
Q_x	Torque measured about X-axis [N.m]
Q_y	Torque measured about Y-axis [N.m]
Q_z	Torque measured about Z-axis [N.m]

R	Rotor disc radius [mm]
r	Distance from rotor hub [mm]
Re	Reynolds number
T	Thrust [N]
U_P	Out-of-plane velocity component [m/s]
U_{total}	Total velocity through disc [m/s]
U_T	In-plane velocity component [m/s]
v_i	Induced velocity [m/s]
V_{cc}	Supply voltage [V]
w	Exit velocity [m/s]

Acronyms

ALM Additive Layer Manufacturing.

AoA Angle of Attack.

BEMT Blade Element Momentum Theory.

BET Blade Element Theory.

BLDC Brushless Direct Current.

CFD Computational Fluid Dynamics.

CMM Coordinate Measuring Machine.

CNC Computer Numerical Control.

COTS Commercial off-the-shelf.

DAQ Data Acquisition (system).

ESC Electronic Speed Controller.

EVP Electric Variable Pitch.

FOM Figure of Merit.

LDA Laser Doppler Anemometry.

LSB Least Significant Bit.

MAV Micro Air Vehicle.

PIV Particle Image Velocimetry.

PWM Pulse Width Modulation.

RPM Revolutions Per Minute.

Abstract

Abstract of thesis submitted by Alexander Bennetts for the Degree of Doctor of Philosophy entitled "Aerodynamic interactions of non-planar rotors"

The aim of this thesis is to improve understanding of the effects of rotor-rotor interference on small scale rotor systems used on Micro Air Vehicles (MAVs). Previous research on rotor-rotor interactions has focused primarily on planar co-axial and tandem rotors of large scale rotorcraft. The work presented is distinct from prior research not only in its consideration of non-planar rotor systems, but also because of the lower Reynolds numbers and the use of fixed-pitch variable-speed propulsion systems.

A design for a novel adjustable rotor interaction test-rig is presented along with a methodology for acquiring accurate and repeatable steady state performance data for two interacting rotor systems. Two six-axis force balances are used to acquire instantaneous and time averaged force and torque data and PIV is used to derive instantaneous and time-averaged flow field data for single and interacting rotor cases. The resulting performance and flow field data represents a unique dataset that can be used in the analysis of small scale rotor interactions, and in the validation of CFD investigations.

Results show that for disc angles of between 180 degrees and 90 degrees interactions between rotors are negligible. As the disc angle is reduced from the orthogonal case to the coaxial case interactions significantly effect thrust, pitching moment, and efficiency.

It is recommended that in the design of non-planar multirotor vehicles disc angles greater than 75 degrees are utilised to avoid the strong rotor-rotor interactions seen at lower disc angles. A review of existing non-planar multirotor concepts shows that the majority avoid significant rotor interactions by virtue of large disc angles.

Declaration

No portion of the work referred to in this thesis has been submitted in support of an application for another degree or qualification of this or any other university or other institute of learning.

Copyright

and commercialisation of this thesis, the Copyright and any Intellectual Property and/or Reproductions described in it may take place is available in the University IP Policy (see `http://documents.manchester.ac.uk/DocuInfo.aspx?DocID=487`), in any relevant Thesis restriction declarations deposited in the University Library, The University Library's regulations (see `http://www.manchester.ac.uk/library/aboutus/regulations`) and in The University's policy on presentation of Theses

Acknowledgements

This thesis marks the end of a 4 year period, yet encompasses only a fraction of what I have been part of as a member of the UAV Research Group.

I would like to start by thanking Bill Crowther for giving me this opportunity, and for giving me a freedom rarely seen from other supervisors. I would also like to thank Peter Hollingsworth for his guidance and endless meandering discussions. Without your help I would not be here today.

I extend my deep gratitude to Mark Quinn for his support over the final years of my PhD, and for teaching me everything I know about PIV in an afternoon!

My thanks to Khris, Gareth, and Will for making our office an endlessly exciting place to work. You have all been instrumental in my time here and I hope we can work together in the future.

Thanks to all the other basement dwellers of George Begg for your help and commiserations as the situation required. In particular to Dave Golding for putting up with my constant requests, and to Ian Lunnon for your help and advice on all things electrical. Jeff, thank you for your endless support over the past 9 years. Pete, thanks for keeping me tied to engineering reality.

The last twelve months have been a juggling act between UAV, PhD, and life. My thanks to Sigita for your patience, support, and criticism on my inability to maintain font between diagrams and prose.

Thank you to my parents who have quietly accepted my almost complete absence for the past 12 months, and have given up asking when I'll get a real job.

Good luck to all other experimentalists swimming against the flow.

Alex

Chapter 1

Introduction

1.1 Motivation

Rotary-wing aircraft have developed over the past century from cumbersome machines that could barely lift their own weight, to efficient aircraft which occupy an indispensable niche in modern society. Helicopters find use in a wide range of roles including construction, surveillance, rescue, defence, and transport. The helicopter is undoubtedly the most flexible platform available in the modern world.

Despite this wide ranging use and seemingly simple design, airflow through and around the helicopter rotor is one of the most difficult aerodynamic problems to solve. After many years of study, whilst a full description of rotor aerodynamics remains elusive, a number of methods for defining and predicting rotor aerodynamics have been developed.

One recent development in rotorcraft is the hovering Micro Air Vehicle (MAV). A MAV is a small aircraft (defined variously as having a maximum dimension of between 15 cm and 50 cm) that is usually designed to meet a number of specific mission requirements at an affordable cost. Their small size and low observability has seen them frequently used in data acquisition and surveillance roles. Hovering MAVs with multiple rotors are generically referred to as multirotors and multicopters in literature, or more specifically as quad- or hex- depending on the number of rotors. Colloquially all multiple rotor hovering MAVs are referred to as 'drones'. In this thesis the term multirotor will be used.

The rise of the multirotor has been somewhat limited by their low aerodynamic efficiency. The rotors of these vehicles are typically operating at Reynolds numbers of under a hundred thousand, significantly lower than a full-scale helicopter rotors which will typically operate at Reynolds numbers of several million. At Reynolds numbers of a hundred thousand and lower the formation of a laminar separation bubble and subsequent thick boundary layers results in increased drag. This gives a poor lift-to-drag ratio and subsequently results in a low figure of merit. Providing the required power and endurance for vehicles of this scale is difficult. Internal Combustion engines of appropriate size tend to be heavy and inefficient, whilst electric propulsion systems lack the typical endurance desired. Thus the success of multirotors relies in part on innovation and improvement of propulsion systems.

As the popularity of multirotors has risen the vehicle planforms have also evolved to become more specialised. A modern multirotor designed for lifting heavy payloads may consist of a number of large diameter partially overlapping rotors. Alternatively the platform may be designed for high manoeuvrability with rotor discs oriented in different planes. Such specialised platforms can result in more significant rotor-rotor interactions, and with propulsion system performance being crucial it is important to understand and quantify these interactions.

Figure 1.1: Vulcan Airlift multirotor designed for large payloads (Vulcan UAV Ltd, 2017).

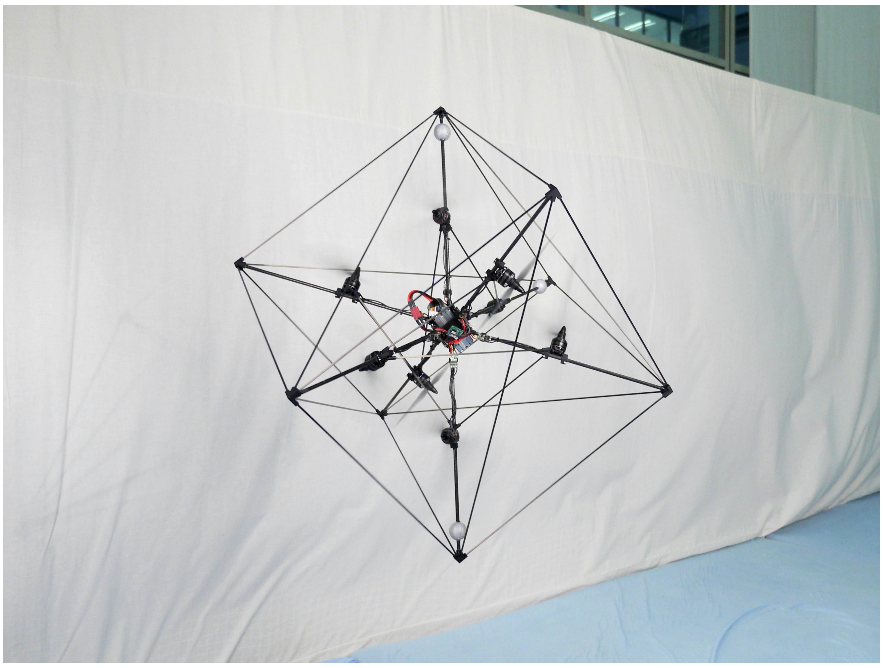

Figure 1.2: ETH Omni-copter - an overactuated multirotor (Brescianini and D'Andrea, 2016).

1.2 Background

The focus of this study is on the interactions between rotors on non-planar multirotor vehicles. A multirotor is a hovering MAV, consisting of three or more small rotors acting in concert to lift and manoeuvre the vehicle. The multirotor differs from conventional helicopters in that it uses differential thrust and torque to provide control, rather than the traditional cyclic method. This vastly simplifies both the mechanical and control complexity of the rotorcraft.

Multirotors have experienced an increase in popularity in recent years as improvements in battery technology have increased the payload and endurance of their electric propulsion systems. Despite this popularity the conventional multirotor design, consisting of a number of fixed-pitch rotors operating in a single plane, has several limitations. In its conventional configuration, in order to generate a force in any plane other than that of the rotor axis, a multirotor vehicle must first rotate around a central axis. The result of this rotation is that generation of the force is delayed, and will likely not resolve entirely in the desired direction. These multirotor configurations can also only hover in a single orientation and find their maximum translational flight speed limited by the 'nose-up' pitching moment generated by the hingeless fixed pitched rotors (Langkamp, 2011). A multirotor without these restrictions would be able to hover in any orientation, and apply a force in any arbitrary direction almost instantly. The result would be a vehicle that is an ideal platform for holding both sensors and tools, and able to respond rapidly to outside disturbances such as wind gusts.

As highlighted, the development and utilisation of MAVs has been limited in part by their poor efficiency. Therefore, to promote the use of rotary wing MAVs it is important to work towards increasing their efficiency at performing the tasks they are designed for.

Non-planar multirotor configurations allow for the arbitrary force generation desired. However, the vehicle would be significantly less efficient than a conventional multirotor carrying an equivalent payload.

The development of the non-planar multirotor is limited by several factors, one of which is the lack of understanding of the rotor interactions resulting from such an arrangement. By investigating these interactions this PhD aims to improve the understanding of non-planar rotor systems with the aim of increasing the efficiency and controllability of such propulsion systems.

The investigation uses laboratory experiments to investigate the effects of interactions between two identical rotor systems on force generation and power requirements. Force, torque, RPM, and power data will be collected to quantify the performance of the rotors, whilst PIV will be used to generate qualitative and quantitative flow field data.

1.3 Rationale

One of the biggest challenges facing MAV development is improving propulsive efficiency. This becomes even more important when considering non-planar rotor configurations where rotor orientation may mean a significant thrust overhead is required to achieve flight and therefore the propulsion system is likely not optimal.

Prior work (Langkamp, 2011) has noted the lack of experimental data on multirotor performance. Whilst there has been an increase in the study of aerodynamics of multirotor vehicles in recent years the experiments are frequently limited in scope and the accuracy and uncertainty of the results is often not discussed. In addition there is limited flow field data available for MAV scale rotors, especially considering interactions between two or more rotor systems.

1.4 Aim and objectives

1.4.1 Aim of this work

The work presented in this thesis is intended to further the understanding of multirotor performance through investigation of the aerodynamic interactions of closely aligned rotor discs.

To date in the development of non-planar multirotor configurations, rotor interactions have often been ignored or treated as transient disturbances like gusts of wind (Brescianini and D'Andrea, 2016). A more complete understanding of the interactions between non-planar rotors and the resultant flow fields will aid in the design of more efficient non-planar configurations and allow for more robust control laws to be developed.

1.4.2 Objectives

1. Develop a structurally appropriate thrust testing apparatus for measuring performance data of one or more rotors.

2. Obtain reliable instantaneous and time averaged performance data for MAV scale rotors.

3. Obtain quantitative and qualitative flow field data for isolated and interacting rotors.

4. Examine how non-planar rotor interactions affect rotor performance and the implications for the design of non-planar mulitrotor vehicles.

1.4.3 Scope and limitations

The focus of this work is the acquisition and analysis of repeatable performance and flow field data that will increase understanding of aerodynamic interactions between non-planar rotor systems. The work focuses on the time averaged steady state condition. An intentionally simplified rotor system is used to ease comparison between the experimental data and numerical simulations. A single blade pitch representative of Commercial off-the-shelf (COTS) rotors is considered.

1.4.4 Thesis summary

The concept of the multirotor and the history of its development is presented in brief in Chapter 2, covering early flying vehicle concepts of the 19th century to the modern ubiquitous quadrotor configuration. It is discussed in particular that majority of modern multirotor research is carried out from the perspective of autonomy, control, and application. In comparison aerodynamic studies of multirotors are uncommon and can be limited in detail and rigour.

To understand the experimental results presented in this thesis, a small amount of general theory on the aerodynamics of rotor craft is useful. Chapter 3 provides the requisite helicopter theory to allow an unfamiliar reader to understand the methodologies used to predict rotor performance, and assess performance from experimental data. A brief explanation of Particle Image Velocimetry is provided to provide understanding of the limitations of the approach used in this investigation.

The experimental apparatus and technique required for the experimental investigation is detailed exhaustively in Chapter 4. The specifics of the hardware used in the experiment are provided, and the MATLAB code is included in Appendix A.

The results of the experimental investigation are summarised in a series of combined force vector and flow field vector figures at the beginning of Chapter 5. A more detailed analysis follows, exploring the relationship between disc angle and the resultant forces and moments. A novel approach is taken to extracting a conventional helicopter performance characteristic from the dataset Chapter 6 takes the main findings of the investigation and applies them to existing non-planar multirotor designs, and recommendations for how future vehicle designs can exploit non-planar rotor systems are made.

Chapter 7 completes the thesis with a summary of the conclusions and suggestions for further work.

1.5 Contributions

The main contributions of this thesis are:

1. Analysis of the interaction effects of non-planar rotor systems and the potential impact on the design and development of non-planar multirotor vehicles.

2. A unique experimental dataset providing performance data for small-scale fixed pitched rotors both in isolation and whilst interacting aerodynamically with another rotor.

3. Instantaneous and time averaged flow field velocity data for small-scale fixed pitch rotors in isolation and interaction cases.

4. Development of an extensible adjustable rotor interaction rig that can be used to position one or more rotor systems into numerous orientations and acquire performance data.

Chapter 2

State of the Art

2.1 Multirotors

2.1.1 Development of the multirotor

Recent years have seen a significant rise in popularity of the fixed-pitch multirotor, favoured over other rotorcraft configurations for their mechanical simplicity, low cost, and ease of use. Whilst this boom in popularity could easily be taken to indicate the multirotor is a new concept, in reality it predates the “conventional” helicopter design we are familiar with.

In 1843 Sir George Cayley published details of his ‘convertiplane’, a plane with four circular lifting surfaces which opened into 8 bladed rotors for ascent or descent. The rotors were arranged in two counter rotating pairs and driven by a centrally mounted engine, however no engine of sufficient power was available at that time.

The first manned, powered, rotorcraft flight was achieved in 1907 by the Breguet-Richet Gyroplane, an uncontrolled quadrotor design. Gyroplane I and II were followed in 1920 by the Oehimichen No. 2 and in 1922 by the de Bothezat

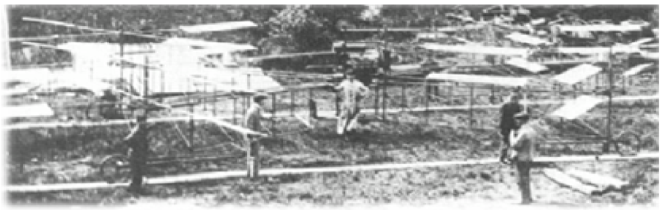

Figure 2.1: Breguet-Richet Gyroplane circa 1907 (Leishman, 2002).

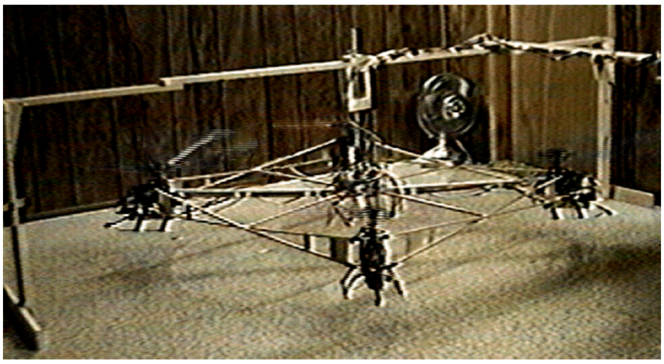

Figure 2.2: The HoverBot prototype (Borenstein, 1992).

helicopter, both consisting of four rotors in a layout that is reminiscent of a modern quadrotor. Rotorcraft development rapidly converged on single main rotor designs and the quadrotor was largely abandoned, with the exception of a brief revival in the 1950s with the Convertawings Model A and Curtiss-Wright VZ-7 concepts.

The late 1990s saw a resurgence in multirotor vehicles as advances in battery technology and electric motors delivered the power to weight ratios required for a viable aircraft. Borenstein (1992) identified the difficulty in autonomously stabilising a model scale helicopter due to the technological limitations of the time and proposed as a solution a four rotor platform, that varied both motor speed and rotor pitch to achieve the high response speeds required for stabilisation. A Stanford project (Kroo et al., 2000) sought to demonstrate the feasibility of a 'Mesicopter', a sub-10 cm scale four rotor fixed pitch multirotor, however concluded before unconstrained flight was achieved. The introduction of the

Draganflyer in 1999 signalled the arrival of the modern "commercial off the shelf" multirotor, combining cheap motors, rotors, and MEMS gyros. The early 2000s saw growth of the multirotor as both remote control toys and tools for research, however growth was somewhat limited by the need for manual stabilisation the aircraft. Over the following decade significant advances in onboard stabilisation and autonomy were made that allowed the widespread proliferation that is seen today.

2.1.2 Studies of multirotor aerodynamics

The main body of multirotor research has focused on applications and control theory, and whilst difficulties associated with rotor interactions are often noted, there remains limited detailed research on the aerodynamics of multirotors.

Hoffmann et al. (2004) at Stanford University were amongst the first to recognise the potential applications of COTS multirotors as a platform for autonomous vehicle testing, as part of the STARMAC project which incorporated attitude stability controllers with Draganflyer multirotors. Waslander et al. (2005) noted that the interactions between rotors resulted in a highly destabilising effect that must be overcome by the control software, however the interactions were not included in their modelling work due to a lack of relevant literature on quadrotor rotor interactions. Later publications from the STARMAC project (Hoffmann et al., 2007; Hoffmann, 2008; Huang et al., 2009) highlight the lack of attention paid to rotor interference effects, and noted the continued difficulty in achieving stable attitude control due to rotor wake interference. The authors contribute to this area by modelling blade flapping and its effect on pitch control, however this does not sufficiently account for rotor interactions.

Pounds et al. (2004) presents a detailed design approach for larger multirotors making several significant contributions to the understanding of quadrotor vehicle dynamics. As part of this work a theoretical rotor model for multirotors is developed based on the work by Prouty's on conventional helicopters. Pounds identifies the value of teetering rotors to achieving favourably flight dynamics, and also suggested the use of variable pitch rotor systems to overcome the scaling issues that hindered larger fixed pitch multirotors. Ultimately improvements in brushless motor control resulted in variable speed fixed pitch systems prevailing over variable pitch systems and their increased mechanical complexity. As with other studies rotor aerodynamics are modelled simply and do not consider rotor-rotor interactions. Later work by Pounds et al. (2010) emphasises the simplistic nature of multirotor aerodynamic research, with the state of the art being Blade Element Momementum Theory models that may or may not consider flapping effects. Pounds identifies how this lack of knowledge complicates development of large multirotors where actuator bandwidth is too low to 'brute force' a stability solution.

Bouabdallah et al. presented several papers (2004b; 2004a; 2005; 2005; 2007; 2007) of work on modelling and design of multirotors as part of the "OS4" project, a 0.5 kg four rotor aircraft with 100% thrust margin. The OS4 simulation model improved upon others through the inclusion of forces and moments derived using Blade Element Momentum Theory, as described by Leishman (2006) and applied by Gay to the Stanford Mesicopter. A focus of the work was achieving autonomous take-off and landing, and therefore the model presented makes an allowance for the effect of ground proximity. No other effects on rotor inflow, such as forward flight or rotor interactions, are considered, although the authors do note the difficulty in miniaturising and controlling quad rotors due the aerodynamic interactions between rotors (Bouabdallah et al., 2006).

Figure 2.3: The OS4 Quadrotor (Bouabdallah, 2007)

A more detailed multirotor model is presented in the work by Martinez (2007) on the Draganflyer XPro quadrotor. As part of the comprehensive work on quadrotor flight dynamics Martinez presents a Blade Element Momentum Theory model with a more detailed consideration of Prouty's rotor flapping model than seen in Pounds et al. Martinez considers the effects of forward flight and vortex ring states by simple modification of the inflow velocity, based on a 'modified' momentum theory approach and empirical data derived from wind tunnel experiments. Martinez's work included one of the first experimental wind tunnels studies of a multirotor rotor system and considering a rotor in hover, climb, and forward flight. However the experimental investigation was limited by equipment and time constraints and whilst useful for development of the model it was ultimately considered unreliable by the author. Neither the experimental or analytical investigations presented considered rotor interaction effects.

Bristeau et al. (2009) presented one of the first studies specifically considering the aerodynamics of multirotor rotors. As in other studies the authors presented classical helicopter modelling techniques applied to a multirotor vehicle, unlike other studies the authors claim to consider forward flight speed in their model however rotor interactions are ignored.

Langkamp (2011) presents an experimental and analytical investigation of a four rotor multirotor in hover and forward flight, including what appears to be the first published experimental study on multirotor aerodynamics. The investigation was conducted inside a wind tunnel, with the orientation of the test subject adjusted to simulate hover, vertical flight (rotors perpendicular to free stream), and forward flight conditions. Despite being a full size model, the test arrangement had a significantly smaller total disc area to tunnel area ratio than typical tandem rotor experiments, and efforts were made to keep overall blockage area down. Langkamp investigated the impact of rotor-rotor interference in the form of rotor tip spacing and found a lack of measurable change in rotor efficiency with spacing in hover, and a small but ultimately negligible net effect in forward flight. These findings agree with existing research on tandem rotor aircraft.

A similar study was carried out by Harrington (2011) who attempted to derive an 'optimal' quadrotor propulsion system using analytical and experimental techniques. A custom rotor system was manufactured however the use of 3D printing resulted in a rotor with significantly flexible blades. To account for this Harrington expands the typical BEMT approach by using Finite Element Analysis to determine the deflection of the blade. Harrington conducts a similar rotor interaction experiment to Langkamp, varying rotor tip clearance from 0.02 to 1 rotor radii. Unlike Langkamp, Harrington considers the rotors in isolation from the body of the quadrotor and only in the static thrust condition, however Harrington also considers the direction of rotation of the rotors and obtains simple qualitative flow field data using smoke visualisation. Harrington concludes that tip spacing has a negligible effect on power loading (thrust per unit power, T/P), although they also state that a thrust penalty of 6 percent is seen with four rotors arranged in a representative quadrotor configuration. The flow visualisation carried out showed that for two adjacent planar rotors with tip spacing as low as 0.1R, there was a shared inflow with two distinct wake regions that did not interact. The description of the experimental setup does not include information on the proximity of the rotors under test to other structures or on any blockages, or lack thereof, in the inflow or wake regions. Therefore, it is difficult to judge the reliability of this experimental data, especially as the rotor-rotor interference results do not agree with Langkamp or historic investigations on tandem rotor aircraft.

Similarly to Langkamp and Harrington, Otsuka and Nagatani (2016) replicated the classic tandem rotor spacing experiment with COTS multirotor rotors in an effort to reduce the overall planform size of an eight rotor multirotor. The authors concluded that the lower rotor in a pair of overlapping rotors experiences a decrease in thrust due to a reduction in inflow velocity, whilst the upper rotor experiences no noticeable change in thrust. For coplanar rotors no significant effects are seen as with Harrington's work.

More recently, Russell et al. (2016) and Foster and Hartman (2017) have published results from comprehensive wind tunnel campaigns on multirotors operating under various flight conditions. Russell et al. consider a number of different COTS multirotor aircraft, and also individual rotors from these aircraft, operating under hover and forward flight conditions. Whilst their investigation does not directly consider rotor interactions the authors do note the contribution of rotor-rotor interactions towards vehicle vibration. Foster and Hartman consider a single COTS quadrotor in greater detail, acquiring data on vehicle aerodynamics and propulsion at a large variety of wind incidences. The authors acknowledge the importance of rotor-rotor and rotor-body interactions, but do not report any findings. Both these investigations are significant as they are part of a small number of sources of high quality experimental data on multirotor aerodynamics.

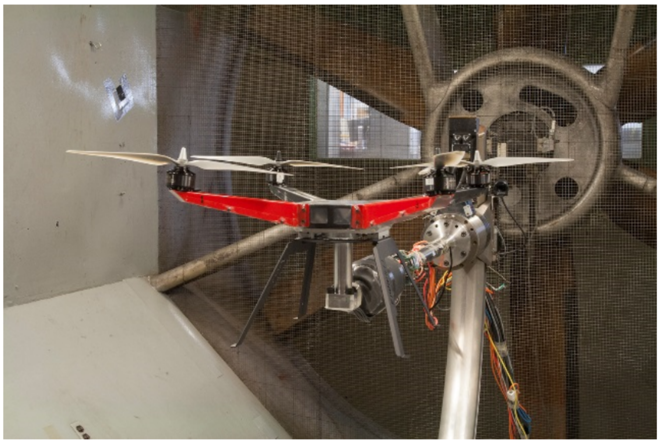

Figure 2.4: Wind tunnel testing of a multirotor (Foster and Hartman, 2017).

Zhou et al. (2017) also studied the effects of rotor tip spacing during their research on aerodynamic and aeroacoustic performance of small multirotor UAVs. This research is notable as being the first to provide detailed flow field data on two planar multirotor scale rotors, through the use of PIV. As in the previous investigations detailed above, Zhou et al. concluded that tip spacing had a very small effect on the thrust coefficient of the rotor, however fluctuations in thrust increased significantly as tip spacing was reduced. The PIV measurements revealed the complex flow field that the authors believed to be responsible for these fluctuations.

Yeo et al. (2015, 2017) have carried out a number of experimental investigations in the rotor wake region as part of their research on detecting downwash from rotorcraft in order to avoid, or better respond to, the effects of flying into the downwash of another rotorcraft. The work is also applicable to lone rotorcraft operating in gusty conditions. The focus of the group's research is onboard aerodynamic sensing for small rotorcraft as an enabler for improved attitude control and trajectory planning. Whilst the aims of the research differ from that of this thesis, the experimental results are relevant as they represent one of the few available sources of quantitative flow field data for both a typical multirotor scale rotor and for a complete COTS quadrotor system.

2.1.3 Non-planar multirotors

A small number of particularly novel multirotor configurations have been developed that merit further attention due to their “non-planar” rotor arrangements. In this context non-planar refers to rotors that are designed with a significant angle between their rotor discs such that the wake from one rotor is likely to interact directly with another rotor disc. A number of multirotors exist that are designed with a motor ‘dihedral’, where the motor thrust lines are angled inwards by a few degrees, these are not considered to be a non-planar arrangement. Similarly multirotors with one or more rotors located in a higher or lower plane than the other rotors are also not considered to be non-planar. One of the first modern non-planar multirotors designs was published by Salazar et al. (2008) and consists of a conventional four rotor multirotor vehicle, with an additional lateral rotor located at each corner. These four additional rotors are used to perform lateral movements, allowing a decoupling of attitude and translation dynamics. Salazar et al. acknowledge that there will be interaction between the lateral and main rotor wakes, and attempt to model this through consideration of the lateral rotors’ effect on the induced velocity of the main rotor.

A UK Patent filed by Crowther et al. (2008) describes a rotary wing concept vehicle which uses multiple pairs of rotors capable of sustaining hovering flight whilst also producing an arbitrary force or torque vector. An example vehicle known as Tumbleweed is shown, comprised of six fixed-pitch rotors driven by individual motors. By locating each rotor at a determined angle it is possible to generate arbitrary forces and torques, allowing the vehicle to translate and rotate in a manner a normal multirotor is unable to. A subsequent publication

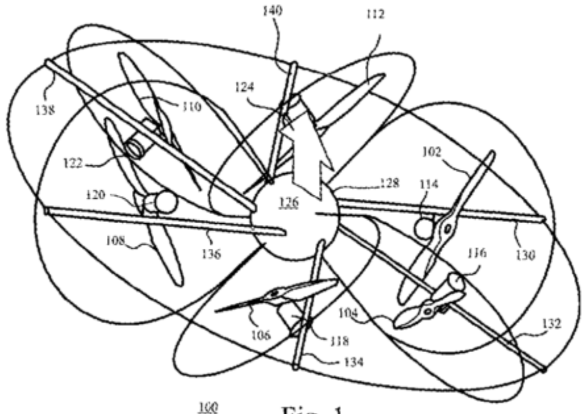

Figure 2.5: A non-planar rotary wing vehicle described in Crowther et al. (2008).

(Crowther et al., 2011) details the kinematic analysis and control design for the non-planar fixed pitch multirotor vehicle as described in the patent. As part of the vehicle modeling it was assumed that all rotors acted independently in a hover condition, and so an experiment was conducted to evaluate the interference between the six rotors. From the presented results it is clear that for low thrust levels required for level hover rotor interactions were negligible, but at higher thrust levels the effects of are more pronounced. The authors indicate that further work is required in this area to enable the vehicle to be accurately modelled when under the more extreme flying conditions it is designed for. In another publication Langkamp et al. (2011) report a successful hovering flight of the fixed-pitch design, and a new development presented utilising Electric Variable Pitch (EVP) propulsion systems. This new propulsion system allowed each rotor to generate thrust in both directions and increasing the control authority of the vehicle, as well as increasing the interactions between rotors. Vehicle sizing and propulsion system analysis placed the required propulsion system at the limit of commercially available EVP systems, and successful flight was not achieved.

A non-planar multirotor is presented by Jiang and Voyles (2013) consisting of an almost entirely conventional six rotor multirotor, where the motors have been displaced angularly by a ‘cant’ angle. Much like the concept detailed above, aligning the motors in this way allows for different thrust vectors to be resolved without rotating the entire airframe. Jiang goes on to optimise this cant angle to 20 degrees, and demonstrate experimentally full controllability of the six degrees of freedom of the multirotor (Jiang, 2013). The relatively low cant angle means rotor-rotor interactions are limited, with the primary drawback of the vehicle design being the reduced power efficiency.

The most accomplished non-planar multirotor representing the current state of the art is the Omni-Directional Aerial Vehicle developed at ETHZ (Brescianini and D’Andrea, 2016). Similarly to Langkamp et al, Brescianini and D’andrea realise the benefits of reverse thrust and implement a reversible fixed pitch propulsion system. As with the variable pitch development of the Tumbleweed vehicle, this propulsion system significantly increases the interactions between rotor systems. In the development of the control system it is noted by the authors that the aerodynamic interactions between the non-planar rotors are likely to have a significant impact on vehicle dynamics, however modeling these effects is very challenging. As a result, these interactions are treated as disturbances, like gusts of wind, and compensated for by the controller.

2.1.4 Experimental methods

Relevant literature on multirotor aerodynamics and control often refers to data validation by way of comparison to thrust test stand data (Pounds et al., 2004; Bouabdallah et al., 2004b; Pounds, 2007; Lei et al., 2016). Few investigations document their thrust test stand and the quality and reliability of the data is rarely discussed, others remark on the cost and complexity of developing a test

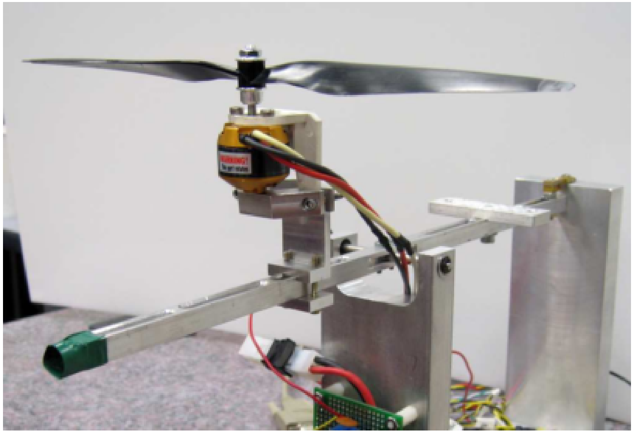

Figure 2.6: Thrust testing stand from Hoffmann et al. (2007).

stand [Wu, 2014]. Of the published test stand designs a significant number do not appear to have considered the proximity and blockage effects or exhibit poor mechanical design, putting the reliability of the reported data into question.

A thrust testing stand is presented by Hoffmann et al. (2007) as part of the work on the STARMAC project, the stand is shown in Figure 2.6. Few details are presented about the stand beyond its capacity to measure thrust, torque, current, and voltage at a rate of 400 Hz. Available images of the stand show that blockage is likely to significantly effect results.

Stepaniak (2008) describes a simple thrust test standing using a hinged lever and digital scales. Despite the limited nature of the setup Stepaniak notes the difficulties created by induced airflow impinging on the test stand. Hrishikeshavan et al. (2012) presents another test stand that uses a digital scale to measure thrust, as shown in Figure 2.7. The accuracy of this balance configuration is not addressed in either study.

Cutler (2012) presents a compact test setup shown in Figure 2.8 for capturing thrust, RPM, current and voltage. No information is provided on the accuracy or calibration of the setup, although it is clear from the image that the rotor will operating in close proximity to the ground and other objects.

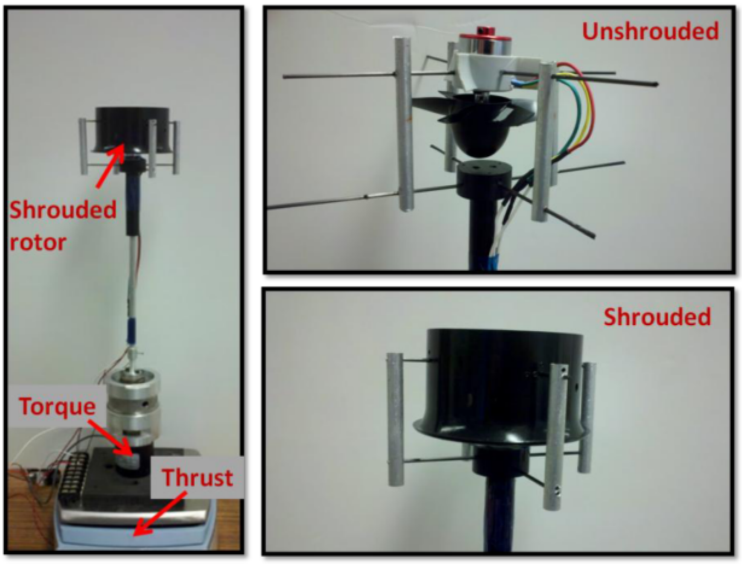

Figure 2.7: Thrust testing stand from Hrishikeshavan et al. (2012).

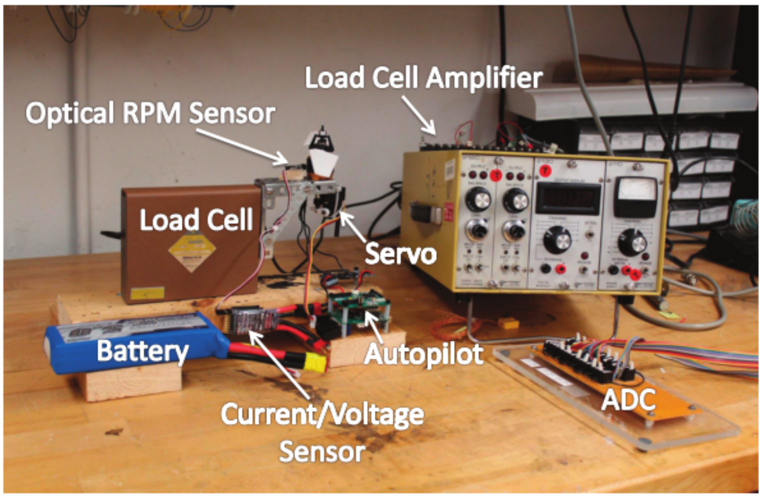

Figure 2.8: Thrust testing stand from Cutler (2012).

A detailed report on test stand development can be found in the work by Beharie (2013) who developed a test stand for analysis of multirotor scale propulsion systems, Figure 2.9. It is unclear from the paper how torque is measured although the author notes that torque measurement was problematic and unreliable. Several methodologies for measuring rotor RPM are presented, however all interfere with the experimental data by either increasing load on the motor or creating a blockage in the rotor wake. Current was measured by monitoring the voltage across a shunt resistor, accuracy of this methodology depends on suitable resistor selection and cooling. Under operation the thrust testing rig exhibited significant oscillation when operating at rotor RPMs near the the resonant frequency of the rig. It can be seen from the images that a significant amount of equipment and structure is located in the wake of the rotor, including the lever arm for the torque sensing apparatus. The effects of blockage on thrust measurement and of wake impingement on the torque measurement are not addressed in the work.

Brazinskas et al. (2016) present an experimental setup and procedure for investigating the effects of rotor overlap on multirotor scale rotors, shown in Fig 2.10. The study is more encompassing than previous work and includes efforts to determine the 3D profile of the rotor blades used. The test rig improves on previous rigs by allowing simultaneous thrust and torque measurements of two rotors that can be varied in axial and radial separation. RPM is measured by sensing the back EMF from the motor. This approach requires sufficient back EMF to be generated by the motor and therefore may lose accuracy at lower RPM. The method may also misrepresent RPM if the motor loses synchronisation with the ESC although such an event is unlikely in the described setup.

Thrust measurements are made at the root of the support arm meaning that the measurements include a component due to support arm drag. Readings are therefore trimmed to account for this offset. A 2% scatter is noted in the thrust

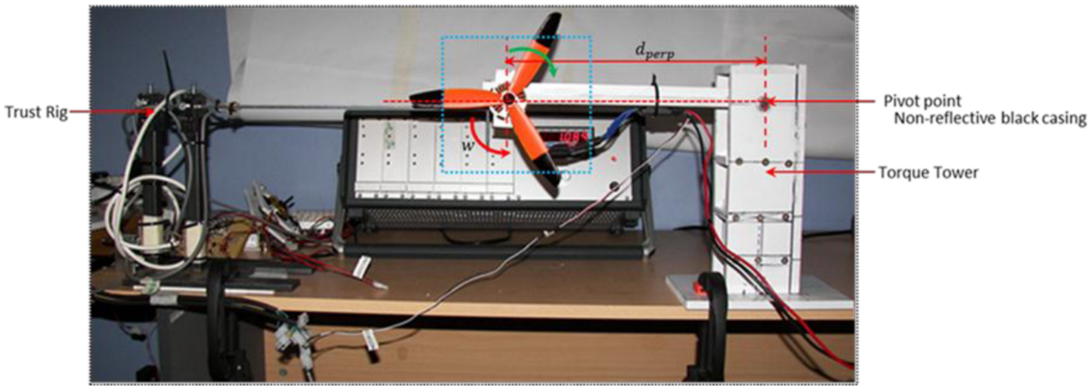

(a) Thrust and torque measurement configuration

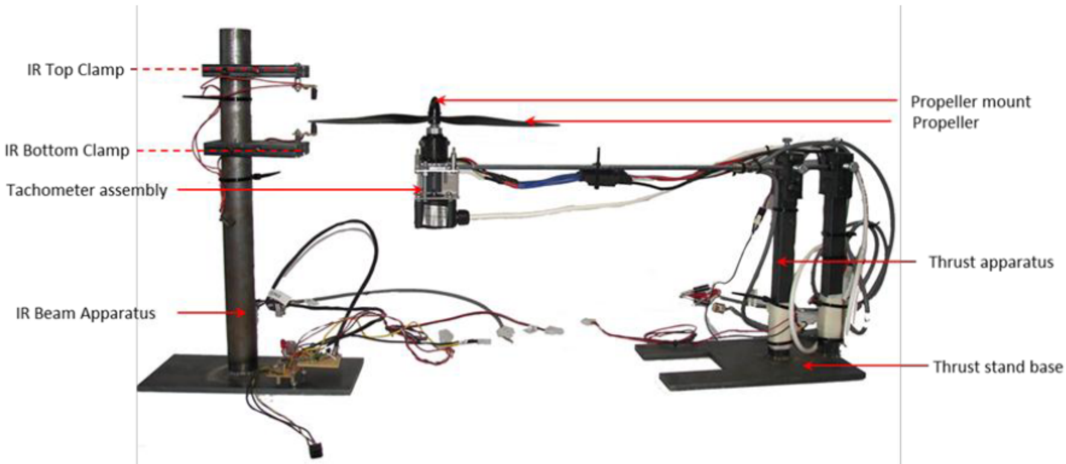

(b) Thrust and RPM measurement configuration

Figure 2.9: Thrust and torque measurement rig from Beharie (2013).

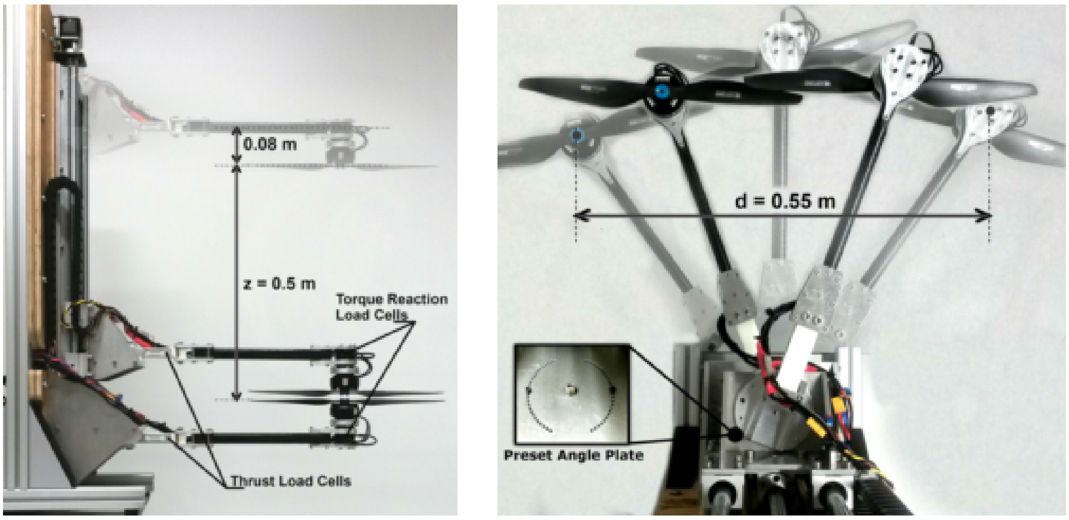

Figure 2.10: Thrust testing stand from Brazinskas et al. (2016).

and torque data but it is not clear if this uncertainty is propagated through the analysis. The authors note that test rig induced error may be the cause of small changes in calculated efficiency.

2.2 Classical rotorcraft aerodynamics

The majority of work on rotor interactions on classical rotorcraft considers the interactions between the main rotor and the tail rotor on a conventional helicopter. A much smaller body of work considers the rotor-rotor interactions of tandem rotor, transverse rotor, and tilt rotor aircraft.

Tandem rotor aircraft, such as the CH-47 Chinook, and transverse rotor aircraft, such as the V-22 Osprey, are the 'production' aircraft most similar to multirotors. The success of the tandem configuration for heavy lift applications has resulted in research into their complex aerodynamics, however they tend to have overlapping rotor discs. The only commercially successful transverse rotor aircraft, the V-22, has rotor discs spaced apart much like a multirotor, but utilises a horizontal tail for pitch control in forward flight.

Dingeldein (1954) and Halliday and Cox (1961) describe separate wind tunnel based investigations into the performance of tandem rotor aircraft. Both found that the front rotor produced more thrust than the rear rotor, and more than a single rotor alone. Halliday found that adjusting the spacing of the rotors, whilst still remaining overlapped, had no apparent effect on the total thrust. Raising the rear rotor above the front rotor was shown to result in a slight increase of thrust for the rear rotor only as it was moved out of the front rotor wake.

Much work has been done on interactions between rotors and the wing and airframes of tiltrotors (McVeigh et al., 1990), but no literature is available on pure rotor-rotor interactions.

2.3 CFD studies of rotor interactions

Accurate modelling of the performance of a rotor and the effects of its wake has historically been a challenging problem for CFD with the most basic of cases taking many hours to compute. In recent years significant progress has been made in modelling the efficiency of hovering rotors, catalysed in part by the AIAA Applied Aerodynamics Rotor Simulation Working Group which was established to evaluate the state-of-the-art in CFD methods for rotor simulation. Barakos and Jimenez-Garcia (2016) have demonstrated that the University of Glasgow Helicopter Multi-Block solver can calculate the nondimensional performance coefficients (C_T, C_Q and FoM) to within 2% or better for a 1/4.74 scale S-76 rotor in hover. More recently Barakos and Jimenez-Garcia have published work on the XV-15 tiltrotor blade as part of the Leonardo HiPerTilt project, which aimes to further CFD methods for simulation of tiltrotor aircraft (Dehaeze et al., 2017).

The work presented includes comparisons between experimental Pressure Sensitive Paint data, and CFD derived pressure distributions, which show a good correlation with some divergence seen at higher thrust coefficients (Jimenez-Garcia and Barakos, 2017).

Barakos et al. note an improvement in processing times in recent years, however in a sample case for an XV-15 tiltrotor a wall-clock time of 17 hours was required on a 232 core high performance computer cluster (Jimenez-Garcia et al., 2016).

Schafroth (2010) compared BEMT and a commercial CFD code during their investigation into the aerodynamics of a small scale coaxial helicopter, as a three dimensional CFD simulation can capture effects that BEMT cannot, such as spanwise flow along the rotor blades. Comparing Schafroth's CFD and BEMT results shows no appreciable improvement in thrust and torque estimates for a single rotor. With the computational requirements of a three dimensional CFD simulation being several orders of magnitude higher than those of a BEMT analysis, it is unsurprising that BEMT remains the more prevalent technique for estimating rotor forces in multirotor research. Despite this BEMT is unsuited to predicting the effects interactions between rotors, wakes, and bodies and high fidelity three dimensional CFD simulation is required instead.

A study by Yoon et al. (2016) investigated the wake flow of a quad tilt-rotor in hover using NASA's OVERFLOW CFD package, and considers four rotors operating together in free air and with wing and fuselage structures acting as blockages. The results of the investigation show average thrust generation for each of the four rotors is reduced as spacing is reduced, a result that is in broad agreement with the existing experimental work on tandem rotors and multirotors presented above. When considering the four rotors along with the wings and fuselage the authors found the rotors generated 3 percent more thrust than in the isolated case. The authors suggest that at least some of this improvement is due to the fuselage limiting wake interactions although they do not quantify this claim. The authors also do not address impact on rotor thrust impinging directly onto the wing structures in the nearfield rotor wakes, however they do note a large “download” generated by the wings which is presumably a result of said interaction.

2.4 Visualising rotor flow fields

As discussed previously the flow field around one or more rotor systems is complex and difficult to predict. Early studies of rotorcraft, such as Dingeldein, used balsa dust to capture qualitative imagery of the flow field around the rotors. More recent studies, such as that of Harrington, use smoke or oil droplets to achieve a similar result.

As CFD techniques improve, and computational power decreases in cost, complex CFD studies of helicopter flow fields are becoming accessible and there is a desire for quantitative experimental data to validate these studies. Whilst forces and pressures can be measured somewhat easily, gathering qualitative velocity data through the flow field is more challenging. One of the oldest methodologies available is to measure the flow field at discrete points using pressure probes or hot-wire anemometers, however these techniques are intrusive and gathering data across a large area is laborious even with an automated traverse. The current state-of-the-art technique for capturing flow field data is Particle Image Velocimetry which can measure instantaneous velocity over a large interrogation window, capturing flow features that are otherwise unfeasible to measure experimentally. For more information on the application of PIV to helicopter aerodynamics the interested reader is directed to the excellent paper by Raffel et al. (2017).

At Iowa State University PIV has been used in number of investigations into rotor aerodynamics. Zhou et al. (2017) present the most significant investigation using both two dimensional and stereoscopic PIV to visualise the interaction between two adjacent rotors. Having noticed a loss in thrust as tip spacing between the rotors was reduced, Zhou et al. used PIV techniques to reveal the complex flow interactions between the induced flows. Ning and Hu (2016, 2017) also use PIV to visualise the flow field around their bioinspired multirotor propeller, however they do not use the PIV to capture rotor interactions. The team at Iowa State have also applied PIV to the study of wind turbine wakes.

2.5 Concluding Remarks

A review of the available literature indicates that multirotor research is primarily focused on application and control theory, leaving aerodynamic understanding of multirotors to plateau somewhat. This is partially due to rapid improvements in technology allowing more complex multirotor dynamics to be treated as disturbances to a control scheme rather than needing to be be fully understood aerodynamically.

The current state-of-the-art for modelling a multirotor consists of a Blade Element Momentum theory with allowance for rotor flapping and coning. The more advanced models will generate aerodynamic data for the BEMT model through two dimensional CFD methods.

The availability of experimental performance data for MAV scale rotors is increasing however the validity of some of the experiments is questionable. A review of the relevant literature has revealed that a number of the thrust testing rigs used to validate analytical models are inadequate. Rigs suffer from poor blockage management, poor mechanical design, and poor data acquisition method. Many authors do not address calibration, uncertainty, or accuracy in their analysis making it difficult to determine the value of their conclusions. There is a clear need for a well designed thrust testing rig that can provide accurate, reliable, calibrated force and torque data for a rotor system.

Flow field data for MAV scale rotors has historically been uncommon however there has been a number of recent publications that consider MAV scale rotors and the effect of tip spacing. There remains a lack of flow field data that considers more complex rotor interactions.

Chapter 3

Relevant Theory

3.1 Rotor system performance

A small amount of general theory on the aerodynamics and performance of rotorcraft is useful in adequately assessing the performance of the rotor systems presented in this experimental investigation. A number of theories for predicting rotor performance are summarised within this chapter, for full derivations the reader may refer to 'Principles of Helicopter Aerodynamics' by Leishman (2006) and 'Basic Helicopter Aerodynamics' by Seddon (1990).

3.1.1 Disc actuator theory

Disc actuator theory, or momentum theory, is a model with a long history having been first developed by Rankine in 1865 for analysis of marine propellers. The approach models an ideal rotor as an infinitely thin disc across which there is a pressure difference that induces a velocity along the axis of rotation. From this model it is possible to derive a relationship between the induced velocity and the rotor's radius and power (torque) requirements.

The control volume is defined as the area around the rotor and its wake as

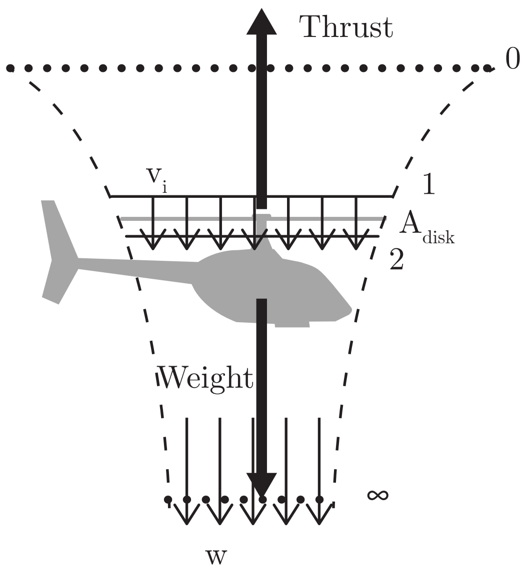

Figure 3.1: Diagram representing the flow through a rotor as defined by disc actuator theory.

shown in Figure 3.1, with the zero and ∞ boundaries at atmospheric pressure. Boundaries one and two are located above and below the rotor disc respectively, and v_i and w refer to the induced velocity and exit velocity respectively. A_x represents cross sectional area at the point in the control volume indicated by the subscript.

The mass flow through the volume can be defined as shown in Equation 3.1a and conservation of momentum (3.1b) and conservation of energy can be used to determine the relationship between rotor power and the energy gain of the fluid in the control volume (3.1c), yielding the relationship (3.1d). This indicates that exit flow velocity is twice that of the induced velocity at the disc, and the equations may be rearranged to allow induced velocity to be expressed as a function of thrust (3.2).

$$m = \rho A_\infty w = \rho A_1 v_i = \rho A_2 v_i \tag{3.1a}$$

$$Thrust = \dot{m}w \tag{3.1b}$$

$$P = Tv_i = \frac{1}{2}\dot{m}w^2 \tag{3.1c}$$

$$w = 2v_i \tag{3.1d}$$

$$v_i = \sqrt{\frac{T}{2\rho A}} \tag{3.2}$$

Disc actuator theory makes several assumptions and approximations in order to quantify the thrust generation and power requirements of a rotor system, and to estimate the the induced velocity through the rotor. The theory assumes that the rotor disc is loaded uniformly, and the flow is steady, inviscid, and incompressible. It does not consider the effects of rotor geometry, angular momentum imparted to the flow, or the work done on fluid that does not pass through the rotor risk. The solution also assumes a constant induced velocity along the rotor blade.

Despite these assumptions disc actuator theory is of particular use in this investigation for validation of flowfield velocity measurement techniques such as PIV.

3.1.2 Blade element theory

Blade Element Theory (BET) was first posited by Drzewiecki in 1892 and again in 1909 for use in the analysis of aeroplane propellers. It is based on the assumption that each section, or element, of a rotor blade acts as a two dimensional aerofoil, providing aerodynamic forces and moments. A non-uniform inflow can be accounted for by adjusting the angle of incidence of each element of the rotor.

However, it is often considered too complex to accurately represent the highly non-uniform velocity field generated by the blade wake, and so a linear or uniform distribution is usually assumed.

This approach allows for the estimation of the aerodynamic loading on the blade element, and the performance of the rotor can subsequently be obtained by integrating the air loads on each element over the length of the blade and averaging over a revolution of the rotor. Additionally by approaching the blade as a series of separate elements, it is possible to analyse a rotor where twist, chord, and aerofoil change along the blade.

3.1.2.1 Blade element momentum theory

Blade Element Momentum Theory (BEMT) combines the blade element and momentum approaches to modelling a rotorcraft in hover. This model offers improvement over the separate blade element and momentum theories by allowing for an estimation of the inflow distribution across the rotor blade.

The methodology presented by Froude and Finsterwalder divides the rotor disc into a series of annuli, the incremental thrust of which can be calculated using simple momentum theory. This is a 2-D model that assumes no interaction between the annuli, and therefore loses validity towards the blade root and tips. The 'tip loss' effect can be approximated using Prandtl's 'circulation-loss' model.

Although an improvement over BET, the BEMT model is still limited as it assumes no interaction between the annuli, and is applicable only in hover. BEMT is often used to optimise the geometry of a rotor blade to reduce its power requirements, however in this investigation it is used to characterise an existing rotor system.

3.1.2.2 Methodology

In this work an implementation of BET was used to generate thrust estimates for isolated rotor systems. These estimates were used to develop design specifications for the thrust testing system and for comparison to experimental data.

This section provides a brief overview into the application of BET and the derivation of key equations. The simplified method presented here is based on the work by Leishman (2006), who in turn draws on the approaches to BET established in prior literature.

Initially the blade is broken up into elements of width dy at radius y from the rotor hub, as shown in Fig 3.2a, where each blade element experiences the incident velocities shown in Fig 3.2b. The element experiences an out-of-plane velocity component U_P due to induced airflow and climb, and an in-plane component U_T due to the rotation of the blade, giving the resultant velocity as shown in Equation 3.3c.

$$U_P = V_c + v_i \tag{3.3a}$$

$$U_T = \Omega y \tag{3.3b}$$

$$U_{total} = \sqrt{U_T^2 + U_P^2} \tag{3.3c}$$

The induced angle of attack, ϕ at the blade element can be calculated as

$$\phi = \arctan\left(\frac{U_P}{U_T}\right) \tag{3.4}$$

Each blade element has a local pitch angle θ which is a result of blade twist distribution, and the collective pitch. For small angles $\phi \approx U_P/U_T$, allowing the effective Angle of Attack for a blade element with local pitch angle θ, to be defined as

$$\alpha = \theta - \phi = \theta - \frac{U_P}{U_T} \tag{3.5}$$

The lift and drag for each blade element can therefore be written as

$$dL = \frac{1}{2}\rho U_{total}^2 C_l c dy \tag{3.6a}$$

$$dD = \frac{1}{2}\rho U_{total}^2 C_d c dy \tag{3.6b}$$

Resolving lift and drag perpendicular and parallel to the rotor disc allows the thrust (T), torque (Q), and power (P) contributions of the element can be determined, where N_b is the number of rotor blades.

$$dT = N_b(dL\cos\phi - dD\sin\phi) \tag{3.7a}$$

$$dQ = N_b(dL\sin\phi + dD\cos\phi)y \tag{3.7b}$$

$$dP = N_b(dL\sin\phi + dD\cos\phi)\Omega y \tag{3.7c}$$

By assuming that U_T is significantly larger that U_P, that the induced angle ϕ is very small (allowing for the application of small angle approximation), and that drag is much less than lift (such that $dD\phi$ is negligible), the equations simplify

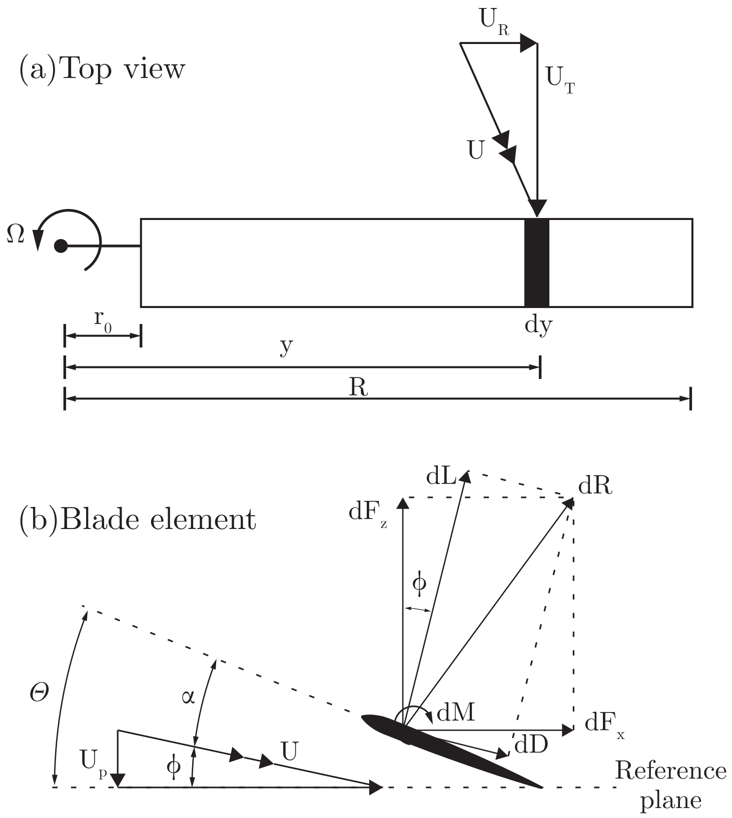

Figure 3.2: Diagram showing the aerodynamic environment of a typical blade element (derived from Leishman (2006)).

to

$$dT = N_b dL \tag{3.8a}$$

$$dQ = N_b(dL\phi + dD)y \tag{3.8b}$$

$$dT = N_b(dL\phi + dD)\Omega y \tag{3.8c}$$

3.1.3 Nondimensionalisation

In assessing and comparing the performance of a rotor system under various conditions, it is useful to employ nondimensional coefficients for the quantities of interest.

3.1.3.1 Thrust, torque, and power coefficients

The rotor thrust coefficient is defined as

$$C_T = \frac{T}{\rho A_{disc}(\Omega R)^2} \tag{3.9}$$

Where A_{disc} is the area of the rotor disc and ΩR is the rotor tip speed.

The rotor ideal power coefficient is defined as

$$C_P = \frac{P}{\rho A_{disc}(\Omega R)^3} \tag{3.10}$$

And the rotor shaft torque coefficient is defined as

$$C_Q = \frac{Q}{\rho A_{disc}\Omega^2 R^3} \tag{3.11}$$

This power coefficient can be used in the Figure of Merit (FOM) defined in Equation 3.12.

3.1.3.2 Figure of Merit (FOM)

The efficiency of a hovering helicopter is often quantified by a nondimensional measure called the FOM. The measure is defined as the ratio of ideal power to actual power requirements (Equation 3.12) where ideal power can be derived from the simple momentum theory.

$$\text{Figure of Merit} = \frac{\text{Ideal power required for hover}}{\text{Actual power required for hover}} \tag{3.12}$$

For application to experimental data the FOM can be written as

$$\text{Figure of Merit} = \frac{{C_{T_{meas}}}^{3/2}}{\sqrt{2}C_{P_{meas}}} \tag{3.13}$$

This formulation for FOM is suitable for comparing isolated rotors at similar disc loadings. An approach to calculating FOM specifically for coaxial rotor systems where the rotors are operating at different disc loadings is presented by Leishman and Syal (2008). Whilst the formulations presented by Leishman and Syal are useful in comparison between coaxial and isolated rotor systems, they are only suitable for a coaxial rotor system where both rotors are working in unison. The varying disc angles and thrust vectors considered in this investigation mean that the coaxial rotor formulation for FOM is not suited to assessing the combined efficiency of the rotor system.

Conventional single rotor FOM may be used to monitor the change in efficiency of each rotor as conditions change, however this FOM will be specific to each experiment test point and is not suitable for comparison with other experiments.

3.2 Particle Image Velocimetry

PIV is a flow field visualisation technique and a non-intrusive method of measuring velocity components simultaneously across the whole flow field. Other traditional flow field interrogation methods, such as pressure sensors, hot wire anemometers and Laser Doppler Anemometry (LDA) measure the velocity only

Table 3.1: Types of PIV (Quinn, 2016).

Name	Acronym	Velocity components
Traditional	2C2D	U,V
Stereoscopic	3C2D	U,V,W
Multi-plane Stereoscopic	3C2.5D	U,V,W
Scanning	2C2.5D	U,V
Scanning Stereoscopic	3C2.5D	U,V,W
Tomographic	3C3D	U,V,W

at one point and may also be intrusive to the flow. The ability of PIV to capture velocity simultaneously over a wide interrogation region allows flow features to be captured that would be otherwise impossible to capture using traditional techniques.

Table 3.1 outlines some of the established PIV techniques currently available, and the velocity components they can resolve. For this investigation where highly rotational flows are being considered it would be useful to utilise either stereoscopic or tomographic PIV, however the equipment required for such a study is not presently available to the present experiments. Instead monoscopic PIV will be used to capture the U and V velocity components. Images will be captured at between 5 and 10 Hz.

The two component two dimension (2C2D) approach used in this investigation will not be able to resolve the velocity component of a flow that is perpendicular to the plane of the laser light sheet. This is important to note due to the high degree of rotation present in the rotor flow field, particularly in the region close to the disc. As a consequence the PIV analysis will under predict the velocity magnitude in regions of highly rotational flow, such as in and around the rotor disc, however the result will be representative of the overall flow field.

3.2.1 PIV setup

A typical PIV experimental setup consists of a laser light source, a particle seeder, and one or more cameras. An optics system is used to transform the coherent laser beam into a light sheet to illuminate the region of interest. The particle seeder is used to seed the flow with light scattering particles which are then recorded by the camera. Image exposure is controlled by the timing of the laser system, allowing the time between images, δT, to be precisely controlled.

The images are subdivided into interrogation windows and particle movement within each region is tracked between images through a process called cross-correlation. The size of the interrogation window must be carefully selected, too large and small flow features will not be captured, too small and seed particles may pass between interrogation windows and not be tracked. Modern PIV software uses an iterative multi-grid method to progressively refine the grid, with the results from the prior analysis providing a reference for each progressive refinement. This allows for an increased vector field resolution whilst reducing spurious vectors.

3.2.2 Limitations

A single camera PIV system will be used in this experiment, meaning the analysis is limited to two velocity components in a 2D plane, defined by the laser sheet. As highlighted previously this means out-of-plane velocity will not be captured and subsequently velocity magnitude will be under estimated in regions of highly three dimensional flow.

Chapter 4

Experimental Methods

4.1 Overview

The objective of this chapter is to describe the methods required to obtain a set of measurement data that can help improve the understanding of rotor interactions. The results may also be used to verify the results of future Computational Fluid Dynamics (CFD) analysis. The experiments conducted consider the previously unstudied rotor-rotor interference effects of non-planar two rotor systems as the relative angle between rotor discs (disc angle) is varied.

4.2 Propulsion system

4.2.1 COTS rotor blades

To draw accurate comparisons between numerical analysis and experimental investigations, it is necessary to correctly model the propellers used in the experimental setup inside the numerical simulation. Aerodynamic properties of the sections of COTS rotors are not readily available, nor are twist and chord distributions. Rotor aerofoil profiles also typically change along the blades, meaning aerodynamic performance varies with radius independent of twist and taper.

There are a number of metrology techniques available to determine the 3D profile of a rotor blade, subsequently allowing the aerofoil profile, chord distribution, and twist distribution to be derived. The simplest approach is through manual inspection, using a flat reference plane and a dial gauge to determine the location of reference points on the rotor in three dimensional space. This process is adequate for determining the rough outline of the rotor, but it is labour intensive and it would be infeasible to inspect the number of reference points required to build an accurate 3D model of the blade. For complex shapes with large numbers of reference points it is more appropriate to use a Coordinate Measuring Machine (CMM). CMMs come in a number of formats each having its own benefits and costs in terms of capability. In this investigation a simple scanning type CMM is used, which consists of a computer controlled gantry and piezo based probe. The machine operates by sweeping through a predefined volume with the piezo probe and logging the position of the probe tip when it touches the rotor with a resolution of up to 0.05 mm. The main disadvantage to this method is that only one side of the rotor can be scanned at a time, as shown in Fig 4.1, with the meshes for the two separate halves being manually combined after scanning.

Commercially available multirotor rotors can be broadly categorised into 'acrobatic'[1] and 'utility' designs. Acrobatic rotors are typically designed for high RPM operation and low mass, often at the expense of rigidity. These rotors are usually considered consumable items and are commonly made from unreinforced plastics. This design approach is contrary to what one may expect but is a symptom of a hobby driven industry.

In contrast utility rotors are designed for low RPM operation, and achieve high thrust levels through larger disc areas. These rotors are usually made from

[1] Acrobatic is used preferentially to aerobatic by manufacturers

Figure 4.1: 3D Scan of COTS rotor from a DJI multirotor.

carbon fibre reinforced plastic and manufactured to a much higher standard than traditional RC propellers. The large disc areas of utility rotors, with diameters in excess of 300 mm, make them unsuitable for this investigation. Acrobatic type rotors are more suited due to their reduced disc area, however the low rigidity of these designs results in a somewhat flexible rotor that allows the rotor disc shape to change significantly with RPM as the blade cones and twists. This deformation is hard to measure accurately, and means the aerodynamic properties determined from the static rotor shape can become invalid as RPM increases and the blades deform.

An initial study of the deflection of a typical COTS rotor under aerodynamic loading was performed by operating a DJI8045 rotor at high RPM and imaging it with a DSLR. A strobe was used to achieve a short exposure time. Using this method the deflection of the rotor as it cones can be seen. It was anticipated that a more severe motion would be seen during interaction between two rotors. A simple overlapping rotor experiment was setup and imaged using a high speed camera. The setup of this experiment can be seen in Figure 4.2 and a sample result in Figure 4.3 which shows clearly the flapping motion the low rotor undergoes as

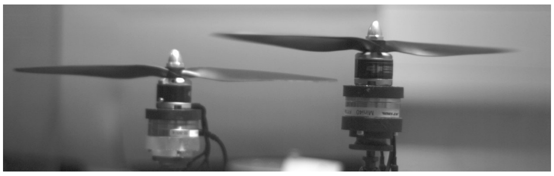

Figure 4.2: Setup to investigate interference induced flapping.

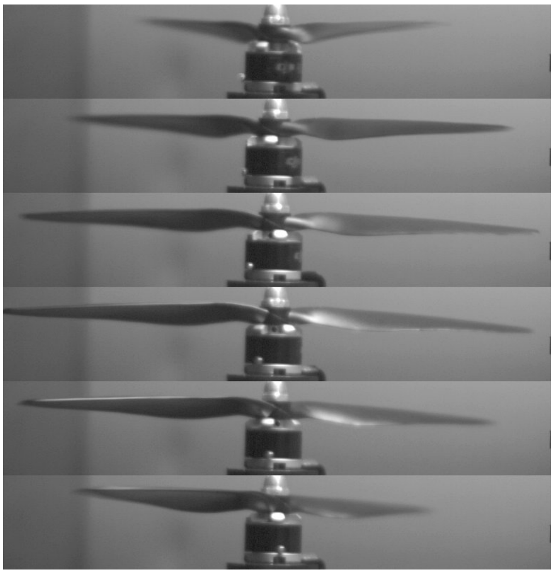

Figure 4.3: High Speed camera imagery showing flapping motion of rotor blade.

it passes into and out of the wake of the upper rotor. For this experiment COTS 8 inch diameter unreinforced plastic propellers were used (DJI8045), the lower rotor speed was 3000 RPM and the upper rotor speed was 7000 RPM. Phase angle between rotors was uncontrolled and varied throughout the experiment.

A study carried out by Nowicki (2016) serves as a source of qualitative and quantitative data on COTS propeller deflection under operational loading. Nowicki uses photogrammetry techniques to capture the three dimensional deflection of two rotors under load, one made from unreinforced thermoset plastic, similar to the rotors shown in Fig 4.2, and the other from carbon fibre reinforced plastic. Unfortunately, the rotors considered are dissimilar in diameter and pitch and thrust values are not provided. Nowicki's results indicate significantly more tip deflection and change in pitch angle for unreinforced plastic compared to carbon

Table 4.1: Comparison of displacement of reinforced and unreinfored rotors at 5000 RPM(Nowicki, 2016).

Rotor	Tip displacement	Coning Angle	Change in Pitch
Unreinforced (24x12.7 cm)	3 mm	2 °	-0.75 °
Reinforced (38x12.7 cm)	1 mm	0.4 °	0.1 °

fibre. A sample of Nowicki's results are shown in Table 4.1. In the presented experiment the reinforced rotor was 50% larger than the unreinforced rotor and generated 250% of the unreinforced rotor thrust at 5000 RPM.

4.2.2 Custom rotor blades

Due to the geometric uncertainty associated with COTS rotors, a custom rigid rotor system was developed. Initially a flat plate rotor profile was considered due to ease of manufacture, however lift and drag data for a thick flat plate is not widely available and is not straightforward to generate. Instead the Clark-Y aerofoil was selected as aerodynamic data is widely available for Reynolds numbers of less than 100,000, and the flat lower side makes the manufacturing process easier. A slight modification to the standard Clark-Y profile was carried out in the form of a thickening of the trailing edge to further ease manufacture. The final produced blade has a chord of 22 mm and span of 126.5 mm, or 135 mm including hub attachment.

Additive Layer Manufacturing (ALM) techniques are often seen as a panacea for creating custom experimental apparatus, particularly for complex shapes, and have been used previously to produce custom rotor designs (Ning and Hu, 2017; Harrington, 2011). In this previous work authors have noted the flexibility of 3D printed parts, and also the potential for the parts to creep over time (Harrington, 2011), this reflects the author's experience and so ALM was discarded as a possible manufacture technique.

The work by Nowicki highlights the significant stiffness advantages of Carbon Fibre reinforced plastic compared to unreinforced thermoset plastic in the manufacture of rotor blades.

Individual rotor blades were machined from solid sheets of Carbon Fibre using a Computer Numerical Control (CNC) mill. In this investigation a 5-axis mill was used to machine the entire blade in one operation to improve the accuracy of the final rotor. However the flat base and thickened trailing edge allows the blades to be machined on a 3-axis mill in one operation with the underside of leading edge being hand finished.

The usual methodology for producing a carbon fibre rotor would be to either layup the part in a mould, or perhaps press the part from sheet stock in a temperature controlled press. Both processes require precision metal moulds and are suited for production runs of parts, making them expensive and unsuited to this investigation where only a small number of rotor blades are needed.

The machined blades were matched into pairs based on mass to reduce vibrations due to mass imbalance across the rotor. Once matched the blades could be further balanced through removal of material.

Aluminium rotor hubs were manufactured to hold a pair of blades at a fixed pitch and interface securely with the motor shaft. The hubs were designed to clamp onto large flat areas at the blade root rather than rely on a through hole method which would wear through the carbon fibre composite over time. The blades are held in the hub with an offset by 2.1 degrees from the zero lift line of a Clark Y aerofoil. This means that a 0 degree hub, where the clamping slot is parallel to the top and bottom of the hub, is holding the blade at a 2.1 degree pitch angle. Similarly, an 8 degree hub is holding the blade at a 10.1 degree pitch angle.

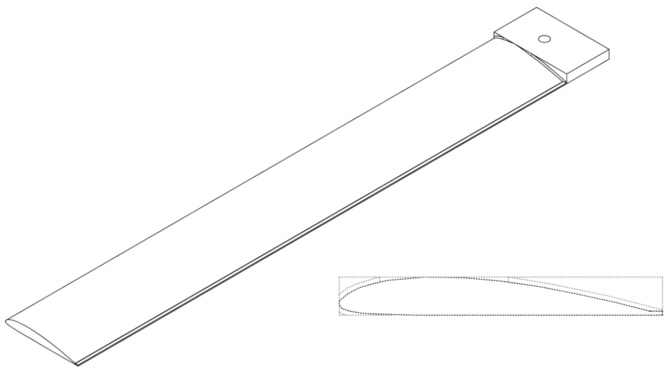

(a) Line drawing of custom Clark Y rotor.

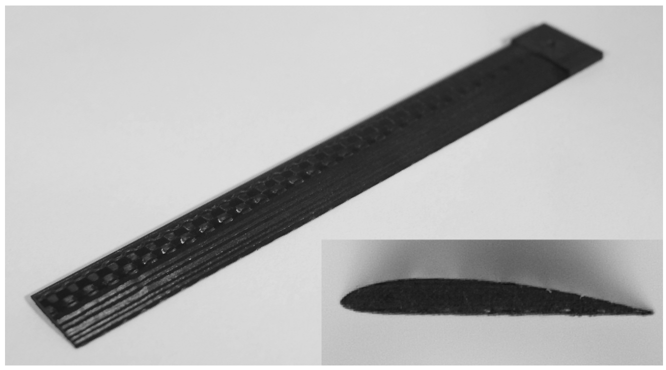

(b) Photograph of Clark-Y rotor blades.

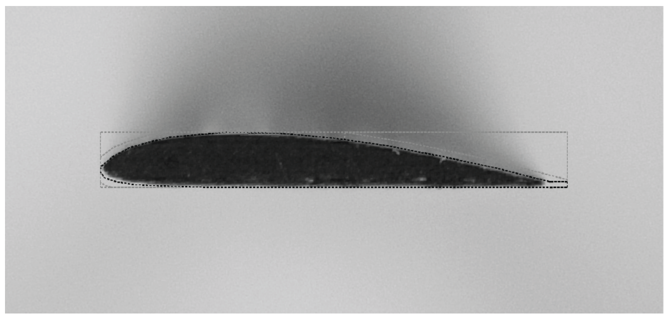

(c) Design and actual profile of rotor blade.

Figure 4.4: Design of custom rotor blades.

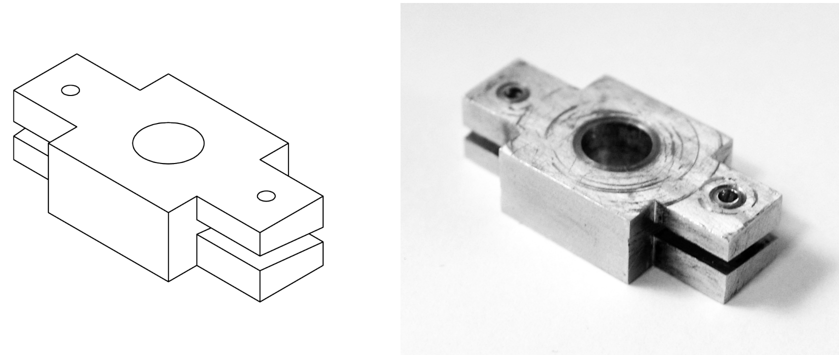

(a) Line drawing of rotor hub. (b) Photograph of rotor hub.

Figure 4.5: Custom rotor hubs.

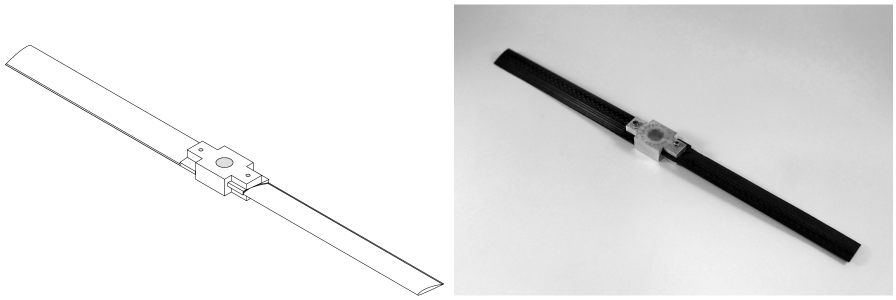

(a) Line drawing of rotor assembly. (b) Photograph of rotor assembly.

Figure 4.6: Custom rotor assembly.

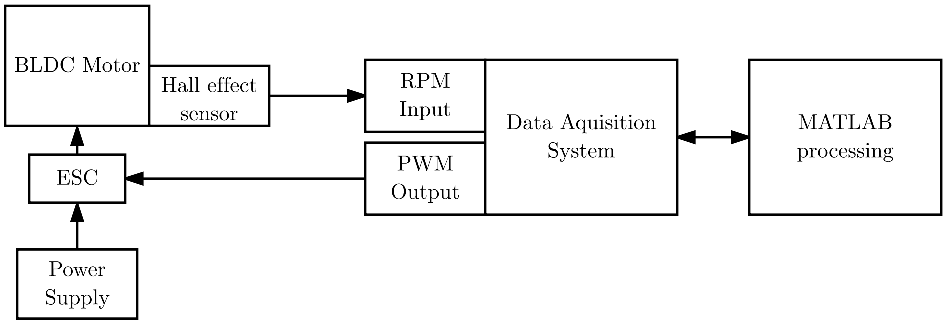

Figure 4.7: Motor control schematic.

4.2.3 Motor and electronic speed controller

A DJI 2212/920 kV Brushless Direct Current (BLDC) motor typical of those used on small multirotors was selected for use. The motor is designed for operation with a supply voltage of between 12 V and 14 V and with an appropriate Electronic Speed Controller (ESC) has a maximum unloaded rotation rate of 920 RPM per volt. A DJI 18A ESC matched to the motor requirements was sourced from the motor manufacturer. Electrical power to the ESC is provided through a TDK-Lambda 12 V power supply, and additional capacitance was added to the circuit to reduce the voltage spikes generated during rapid motor accelerations which would usually be absorbed by a battery. This powertrain is broadly representative of those found on many COTS multirotor aircraft, and has a theoretical maximum rotation rate of 11,000 RPM.

A MATLAB script was used to generate a Pulse Width Modulation (PWM) signal which is output to the ESC by the data acquisition system. Actual motor speed is monitored using a hall effect sensor. A simplified schematic is shown in Figure 4.7.

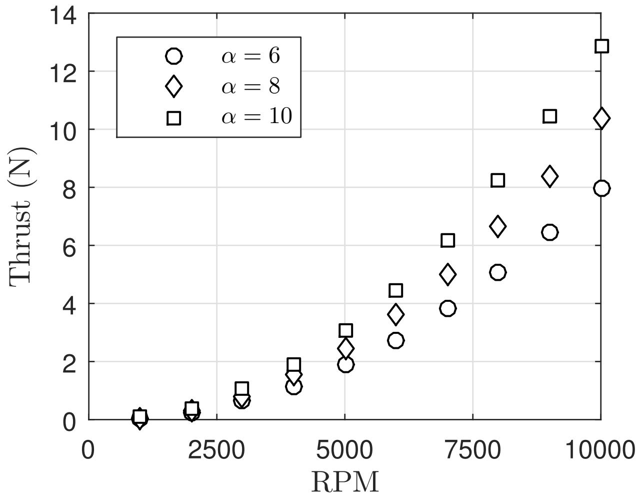

Figure 4.8: A BEMT thrust estimate used for determining rig requirements

4.2.4 Simulation

Using BEMT it is possible to estimate the peak forces generated by the propulsion system detailed above. Aerodynamic data for the Clark Y aerofoil, both theoretical and experimental, is available from a number of sources or can be calculated using a number of widely accepted methods.

A BEMT implementation was created in MATLAB based upon the methodology in Section 3.1.2. Aerodynamic data for the Clark Y aerofoil was determined with the xfoil software package and passed to the BEMT. For simplicity the Reynolds number is assumed to be constant along the blade for each rotational rate, based on conditions at radial position $\frac{r}{R} = 0.8$. This location was chosen based on the thrust distribution of the operating rotor, however it should be noted this differs from the $\frac{r}{R} = 0.75$ location conventionally used for defining rotor properties.

Thrust measurements at rotational rates from 1000 to 10,000 RPM were obtained for a Clark Y aerofoil at 6, 8, and 10 degree pitch, Fig 4.8. This preliminary analysis showed a maximum thrust of approximately 13 N at 10,000 RPM with a 10 degree blade pitch.

4.3 Experimental apparatus

4.3.1 Adjustable interaction rig

The key requirement of the experimental rig is to allow for thrust generation along arbitrary vectors between vertical and horizontal on the XZ-plane. A design requirement was set that the rig should deflect no more than 1% of the rotor diameter, or 2.7 mm, under the maximum load determined in Section 4.2.4.

A structurally rigid rig capable of holding a pair of motors in a number of different spacings and relative angles is a mechanically complex undertaking, especially if a rapid turnaround between different configurations is required. Design and manufacture of a custom solution would be prohibitively expensive in time and material costs, and so an 'off the shelf' solution was sought.

The NOGA Holding System, or NOGA Arm, is an industrial mounting system often used to position dial indicators on a machine tool or to position camera equipment in locations that would otherwise be hard to reach. The system consists of two arms connected with a swivel clamp, with articulated ball-and-socket assemblies located at the end of each arm. A single adjustment knob securely locks the central swivel joint and the ball-and-socket assemblies.

One end of the NOGA arm is connected to the ground side of the force balance via a custom aluminium interface plate, whilst the other end is attached to a length of 25 mm optical mounting rail that serves as a rigid base. This rail allows for the spacing between the rotor assemblies to be varied, whilst the NOGA arms provide the articulation necessary to achieve the desired relative rotor angles.

A simple alignment jig connects to the shaft of each motor and allows the angle and tip spacing desired to be set. Once the motors are positioned, the NOGA arm friction locks are tightened allowing the jig to be removed and the rotors to

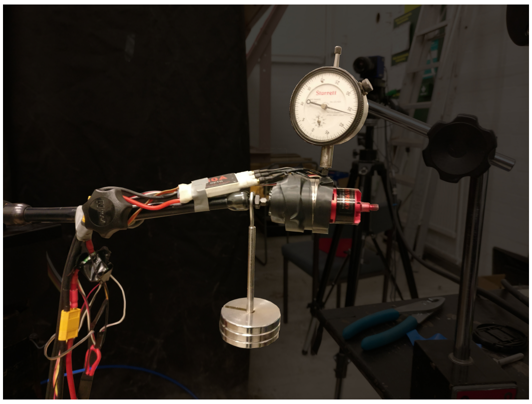

Figure 4.9: Measuring the deflection of a NOGA arm under static loading (Case 2).

be affixed to the motors. This methodology allows motors to be aligned quickly and accurately whilst reducing the blockage presented by the rig apparatus to the wake of each rotor.

NOGA arms are available in a wide variety of styles, strengths, and lengths. The NOGA DG 1105 was selected for this experiment as it has a 40 N static load rating and is of sufficient length to allow the rotors to be spaced as desired. Rigidity of the arm was verified by applying loads whilst measuring deflection with a dial gauge. Two orientation cases were considered with results shown in Figure 4.10. 'Case 1' was a representative orientation based on the rig configuration seen in Figure 4.11. 'Case 2' is a full extension orientation, shown in Figure 4.9, providing a worst case deflection. In both cases the rig displayed a deflection at 10 N load significantly less than the 1% rotor diameter, 2.7 mm, design requirement.

Interfacing between the motor, force balance, and NOGA arm is achieved through bespoke aluminium and plastic bosses. An aluminium boss is used at the balance-arm interface for its dimensional stability however a plastic boss is used at the motor-balance interface to reduce heat transfer from the motor to the force balance. Limiting heat transfer prevents the force balance from heating up during runs which would result in a measurement drift. The effectiveness of the

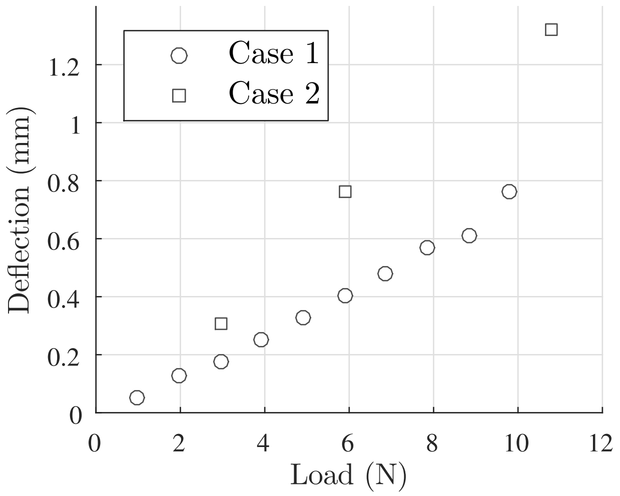

Figure 4.10: Deflection of a NOGA arm under static loading.

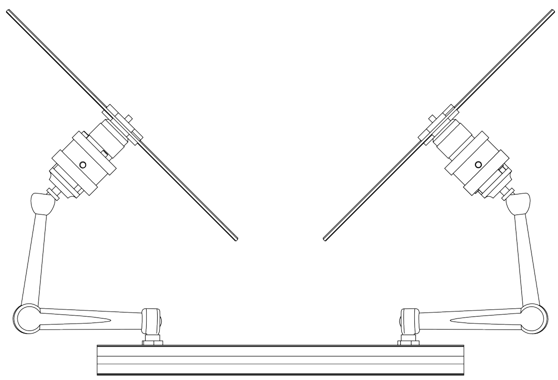

Figure 4.11: Engineering drawing of Adjustable Interaction Rig setup.

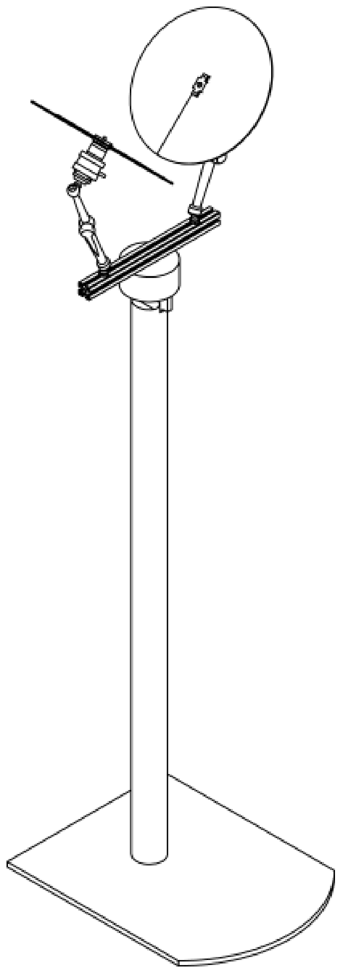

Figure 4.12: Engineering drawing of free standing test stand.

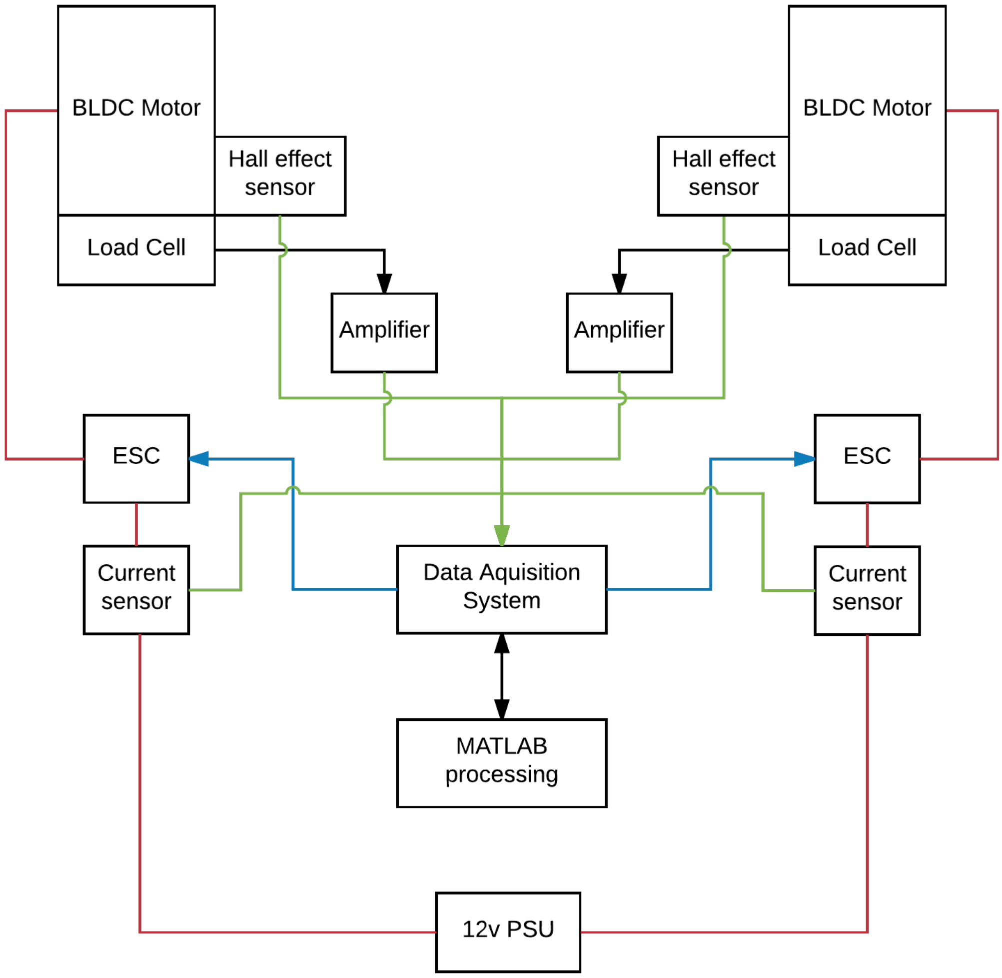

Figure 4.13: Schematic of data acquisition setup.

plastic boss for heat isolation is measured by running a series of long period high thrust tests to heat the motor up and comparing thrust levels across the period.

4.3.2 Data acquisition

For the experimental data gathered in this study to be considered valid, it is important that appropriate data acquisition methods are used, and all sensors involved are calibrated and used within specification.

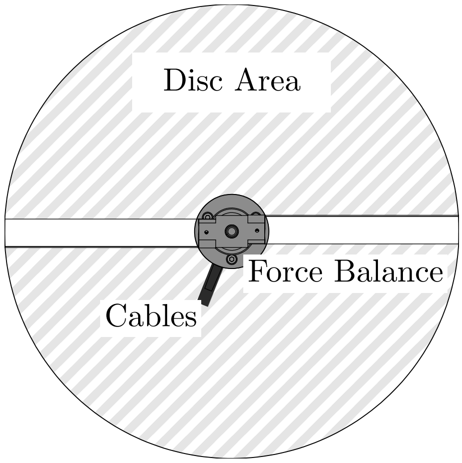

Figure 4.14: Diagram showing blockage behind disc area in dark grey and black.

4.3.2.1 ATI Force Balance

Force and torque on each rotor are measured using an ATI Mini40 Force/Torque transducer. Each Mini40 is positioned underneath a motor such that the normal thrust vector is aligned with the transducer z-axis. The alignment rig described above ensures the X-Z-plane of both transducers are aligned which simplifies data processing. Care was taken to reduce the blockage presented by the transducer and the associated cable and mounting hardware as far as practicable. The configuration is axisymmetric and falls within the region of the rotor hub with the exception of the cabling for the motor, balance, and hall effect sensor. The cabling constitutes a blockage of approximately 0.3% and is located in the X-Z plane common to both motor/balance assembly. The blockage of the force balance and mounts is shown in Fig 4.14.

Each transducer is connected to an ATI IFPS device, which powers the transducer and amplifies the low level voltage output for a data acquisition system. Preliminary investigations revealed that one of the ATI IFPS devices was significantly more sensitive to electrical noise than the other. When averaged, this noise manifests as spurious forces in the Fx and Fy axes and overestimation of

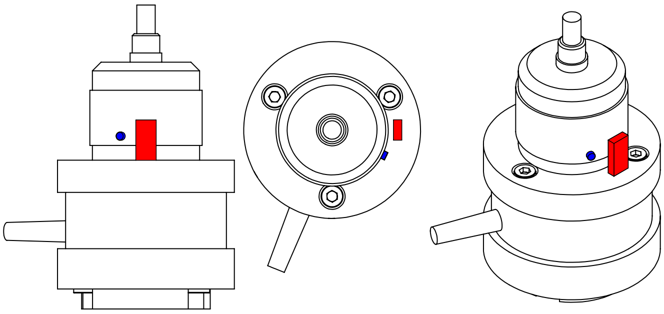

Figure 4.15: Location of hall effect sensor used for RPM measurement.

forces in the Fz axis. Noise level can be mitigated by routing the low voltage force balance signal leads as far as possible from sources of interference, such as power supplies and motor controllers. Particular attention must be paid to the data from this balance to ensure noise levels remain low and force readings are repeatable. Due to the nature of the experimental setup force and torque data from this balance can be discarded if necessary with no significant effect on the experimental results.

4.3.2.2 RPM measurement

Motor RPM is measured through the use of a hall effect sensor and a small magnet attached to the outside of the motor casing. Figure 4.15 shows the configuration with the sensor highlighted in red and magnet in blue. The magnet has a mass of approximately 0.5% of the mass of the motor casing, resulting in an acceptably small impact on motor balance. The RPM of the motor is calculated from the number of pulses per unit time recorded from the hall effect sensor.

4.3.2.3 Current measurement

Electric current to each motor is measured through the use of an ACS715 hall effect current sensor as shown in Figure 4.16. The sensor is capable of measuring 0-30 A currents with a typical error of 1.5%. The sensor is ratiometric meaning

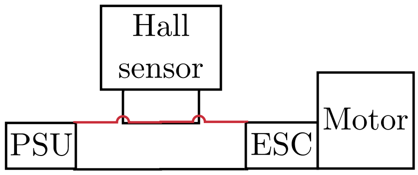

Figure 4.16: Current sensing circuit diagram.

it provides an output voltage proportional to the supply voltage. The nature of operation of hall effect current sensors means care must be taken to minimise the risk of magnetic interference, which could originate from other power cables, or the motors on the test rig.

4.3.2.4 Power supply and motor control

Electrical power to the motors is provided by a TDK Lambda GWS 500 Watt power supply capable of providing between 11 and 14 V under loads of up to 42 A. The power supply will hold the set voltage to within 0.8% as the load is varied. The voltage range matches that of the electronic speed controllers and is representative of a typical power system on a commercial multirotor.

Motor control is provided by the ESC which receives a PWM control signal from the data acquisition system.

4.3.3 Flow visualisation

Two particle tracer methods were used to produce qualitative and quantitative information on the flow around the experimental rig. The first method produced qualitative flow data using a laser light sheet and seed material, whilst the second method used the same light sheet and seed material to perform Particle Image Velocimetry.

The region around the rotor blades is seeded with Di-Ethyl-Hexyl-Sebacat

(DEHS) using a Laskin nozzle based atomizer. The seed material is illuminated using a Litron Nano L-200-15 PIV Pulsed Nd:YAG laser, passed through a cylindrical lens to generate a light sheet, and capable of providing 200 mJ pulses at a 15 Hz repetition rate.

For qualitative imaging of the flow the laser system can be operated alongside a conventional DSLR, using the laser pulse to control the exposure length. For quantitative flow field analysis the laser forms part of an LaVision FlowMaster PIV system, alongside an Imager Pro X2M camera. This system provides an image resolution of 1600x1200 pixels, a minimum ΔT between image frames of 110 nS, and a maximum repetition rate of 10 Hz. By tracking movement of the seed material between two precisely timed frames the velocity vector of the particle can be determined.

4.4 Experimental procedure

4.4.1 Time averaged force, torque, and power data

4.4.1.1 Calibration

ATI mini40 force balances are provided with factory calibrations based on multi-axis loading. Both force balances used in this investigation have only been lightly used within their stated limits, therefore minimal drift from the factory calibration was anticipated. Validation of the factory calibration was carried out by applying a static load to each axis. Multiple loads were used to establish linearity across the measurement rage.

The ACS715 hall effect current sense IC was factory calibrated, and remained unused in a sealed anti-static bag until implemented in the adjustable rotor interaction rig. As a ratiometric sensor it is important that the supply voltage, Vcc, is

Table 4.2: Pitch setting angles of rotor hubs.

ID	Design angle (°)	Actual angle (°)	Deviation
6deg_1_a	6	5.97	0.5%
6deg_1_b	6	5.81	3.2%
6deg_2_a	6	5.82	3.0%
6deg_2_b	6	5.85	2.5%
8deg_1_a	8	7.91	1.1%
8deg_1_b	8	7.70	3.0%
8deg_2_a	8	7.70	3.0%
8deg_2_b	8	7.97	0.4%

known throughout the experiment. A programmable lab power supply is used to provide a stable Vcc voltage source which is recorded throughout the experiment.

Rotation rate of each motor is calculated using a hall-effect sensor and a small magnet located on the motor housing. Pulses from the signal are recorded by a counter on the data acquisition system and referenced against the internal clock. The raw analogue signal is also recorded to allow for easy verification of the counter based RPM during post processing. This methodology was validated against results from a COTS optical tachometer and frequency analysis of the force balance data.

Blade pitch is set through the use of machined aluminium rotor hubs, with each rotor hub providing a single blade pitch. The pitch of each hub was verified by measuring the dimensions of the blade mount with calipers and calculating the setting angle. The design and actual setting angles are shown in Table 4.2, and show a maximum deviation from design of 3.0%. Whilst every effort was made to ensure an accurate measurement, such as referencing the calipers against a calibrated gauge block set, the shape of rotor hub makes measurement difficult and the deviation hard to quantify.

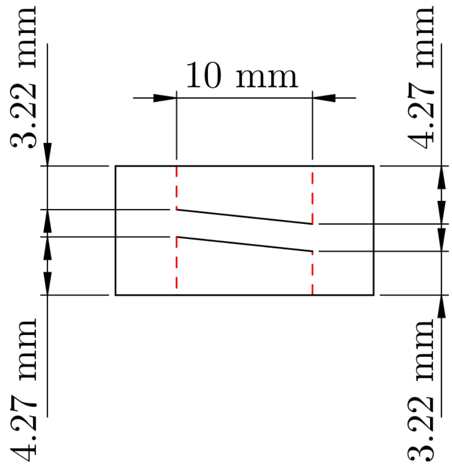

Figure 4.17: Example measurements for setting angle calculation.

Table 4.3: Lengths and Chords of rotor blades.

ID	Length (mm)	Chord (mm)
1	126.5	22.0
2	126.5	22.0
3	126.5	22.0
4	126.5	22.0
5	126.5	22.0
6	126.5	22.0
7	127.0	21.5

4.4.1.2 Data sampling

Required sample rates for the sensors used in the investigation can be determined by application of the Nyquist-Shannon Sampling theorem, which states:

> "If a function x(t) contains no frequencies higher than B Hertz, it is completely determined by giving its ordinates at a series of points spaced 1/(2B) seconds apart."

The obvious frequency content anticipated in the force/torque data is that of the blade rate of the rotor discs. For the two bladed rotor disc and motor combination considered in this experiment the maximum rotation rate is approximately 9,000 RPM giving a blade rate of 300 Hz.

With the introduction of a second rotor disc a short duration event of approximately 0.13 ms occurs as the rotor tips pass in close proximity. To capture meaningful dynamic force data during the interaction a sample rate in excess of 15 kHz is required. With the available data acquisition equipment it is not possible to capture all 12 channels of the force/torque transducers at such a high sample rate.

Electric current data is recorded as an ancillary method of monitoring power requirements of each rotor system, supplementing the torque measurement from the six axis force/torque balance. Frequency content in the current data is generated as the electronic speed controller switches between the phases of the motor however this content is not of interest to the current investigation. Therefore sampling requirements for current data are only that it is sufficient to capture the steady state value. As the current data is being sampled and processed alongside the force torque data it will be recorded at the same rate.

RPM sensing is carried out using a hardware counter on the data acquisition card, which for a square wave has a maximum frequency rate of 5 MHz and a minimum pulse width of 50 nanoseconds. Through experimental investigation the pulse width of the hall effect sensor at 8,000 RPM was determined to be approximately 0.2 ms, well within the range of the hardware counter. With such a short pulse period, reliably capturing the RPM signal using the analogue inputs would require a 10 kHz sample rate.

The LabJack T7 data acquisition device used in this experiment is able to capture the required number of channels at a maximum sample rate of 5 kHz per channel. This sample rate is more than sufficient to meet the requirements detailed above for capturing steady state time averaged values, and allows for a small amount of additional time varying to also be captured.

4.4.1.3 Procedure

Setup and alignment For each experimental run the rig was situated in an open space free of interference in all directions. For the purposes of this investigation this is taken to mean the rig is located at least 10 rotor radii from the nearest object, Figure 4.18. In most scenarios an appropriate location will result in the ground presenting the closest interference boundary at approximately 9R away from the base of the optical mounting rail, Figure 4.19. A survey of experimental investigations of ground effect on hovering flight presented in Leishman (2006) indicates a rotor will be clear of ground effects if it is at least 3 rotor radii from the ground. For each rig relocation, a series of calibration tests was run to establish independence from interaction effects.

The goal of the alignment process to achieve the desired relative rotor angle and tip spacing whilst minimising blockage. A simple alignment methodology utilising laser cut aluminium spacers ensures alignment can be made to the tolerances described in Section 4.3.1. Correct usage of the alignment jigs will align

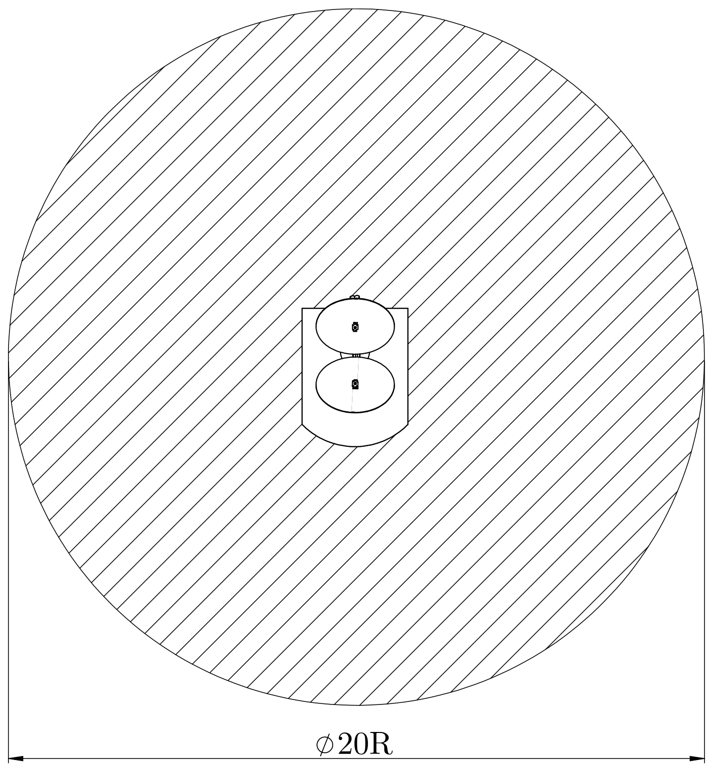

Figure 4.18: Horizontal clearance of experimental setup.

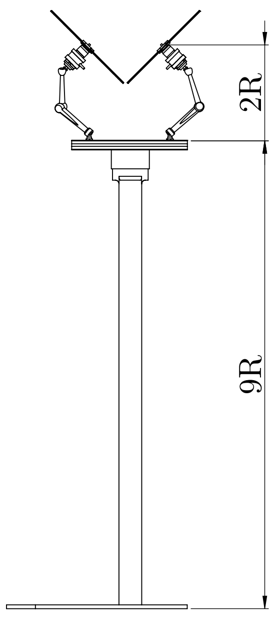

Figure 4.19: Vertical clearance of experimental setup.

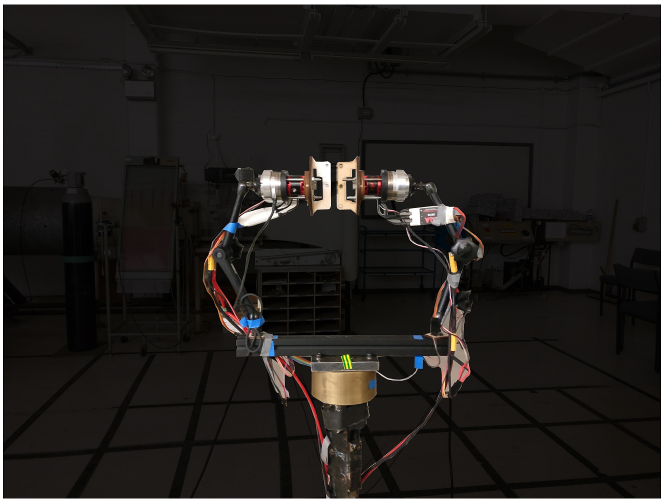

Figure 4.20: Photograph of insitu alignment process.

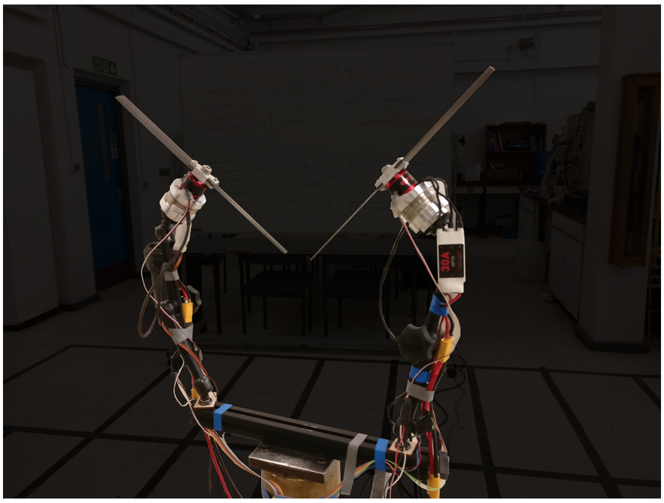

Figure 4.21: Photograph of aligned rig.

the X-Z planes of both force balances, which significantly simplifies the post processing of force and torque data.

The design of the rig is such that for most configurations the supporting structure will be within 2R of one or both rotor discs. The area of the blockage is small (∼5% of the disc area) and with appropriate care should not have a significant effect on the results.

Two different rig configurations are used as shown in Figure 4.22 to facilitate the acquisition of PIV data and to reveal interference effects resulting from

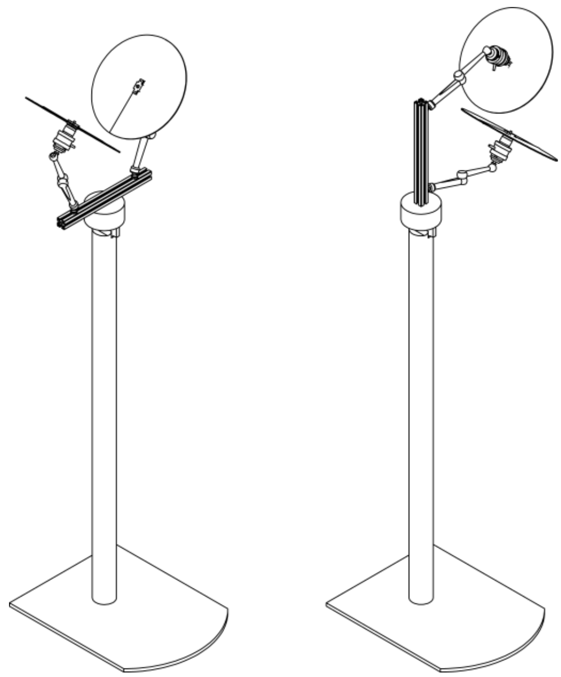

Figure 4.22: Test stand configurations for force data (left) and PIV data (right) collection.

proximity of rotors to the rig structure.

The impact of near and farfield blockages was quantified by running calibration tests in various orientations and comparing results. Figure 4.23 shows thrust results for four separate configurations for each rotor disc. Figure 4.23a shows Disc 1 in a 'puller', or tractor, configuration and Figure 4.23b shows Disc 2 in a 'pusher' configuration. In both figures Run 1 and 2 refer to different rotor orientations in the same location, whilst Run 3 and 4 refer to different rotor orientations carried out in the laser lab used for the PIV experiment. Comparison of the thrust values shows no apparent relationship between thrust and orientation or location. A larger spread is seen in the data from Disc 1 due to the noise sensitivity of the balance hardware discussed previously.

Blade pitch for each experiment is set through selection of an appropriate rotor hub as discussed in Section 4.4.1.1. In this investigation, where a cambered aerofoil is used, a negative pitch setting indicates a reversal of both the rotor disc

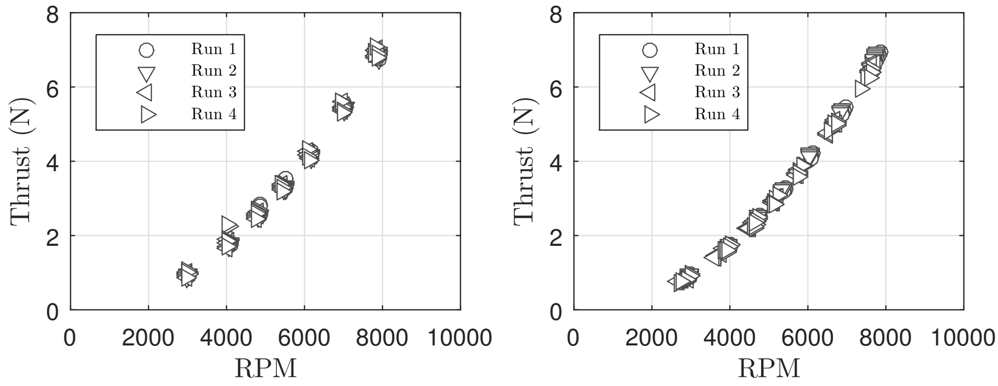

(a) Disc 1 (b) Disc 2

Figure 4.23: Thrust comparisons for differing orientations and locations.

and the direction of rotation.

Following alignment the output voltage of both the instrumentation power supply and motor power supply are verified to insure the correct voltage is being supplied to all electronics. Small variations in instrumentation supply voltage affect the calibration of the current sensors, although this can be corrected for during data processing, and large variations can damage all the attached sensors. Variations in motor power supply voltage change the relationship between the control signal for the speed controller and the rotor RPM. Whilst this can be accounted for during data processing, maintaining a constant motor supply voltage simplifies data processing and allows for fast verification of results.

Running RPM and disc angle sweeps Control software written by the author is used to set each motor speed and acquire the required data. For each test configuration, defined as a combination of disc angle, rotor tip spacing, and blade pitch, the software runs through a predefined set of test points. The experiment can be considered in two halves; in each half one rotor serves as the "static" rotor whilst the other rotor assumes the role of the "dynamic" rotor. The static rotor holds a constant power setting whilst the dynamic rotor steps up through

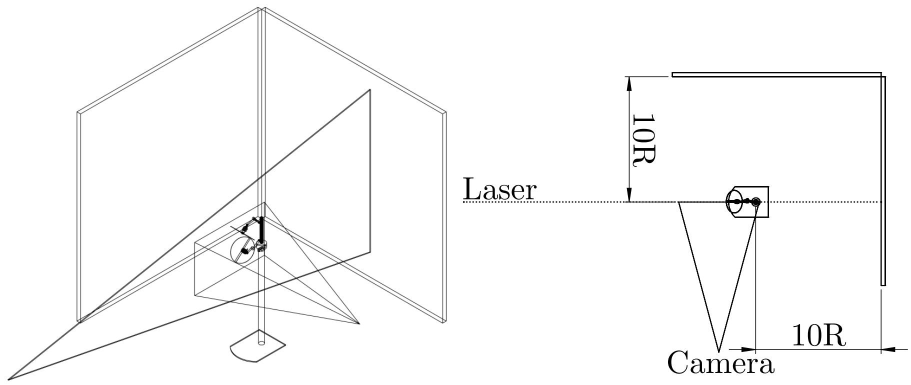

(a) Location **(b)** Spacing from backstop

Figure 4.24: PIV Setup.

seven power settings, repeating each setting three times. The static rotor then advances to the next power setting and the process repeats, ending with both rotors running at full power. The roles of static and dynamic rotor are then reversed and the process is repeated meaning that each specific combination of motor powers is repeated six times.

Preliminary experiments were carried out to verify that there was no hysteresis in the results, which would indicate a dependency on whether each test point was approached from a higher or lower RPM setting. The settling time of the rotor following changes in power demand was determined experimentally to ensure sufficient time is allowed before data acquisition is carried out.

At each test point 5000 samples are collected at a 5 kHz sample rate. At the highest rotor RPM this sample period encompasses over 30 rotations of the rotor disc, providing adequate data for measuring the steady state condition.

4.4.2 Flow field data

Flow field visualisation was performed in a separate room from the main experiments due to the operational requirements of the laser and seeding systems. As with the main experiment the rig was located in an open area free from any

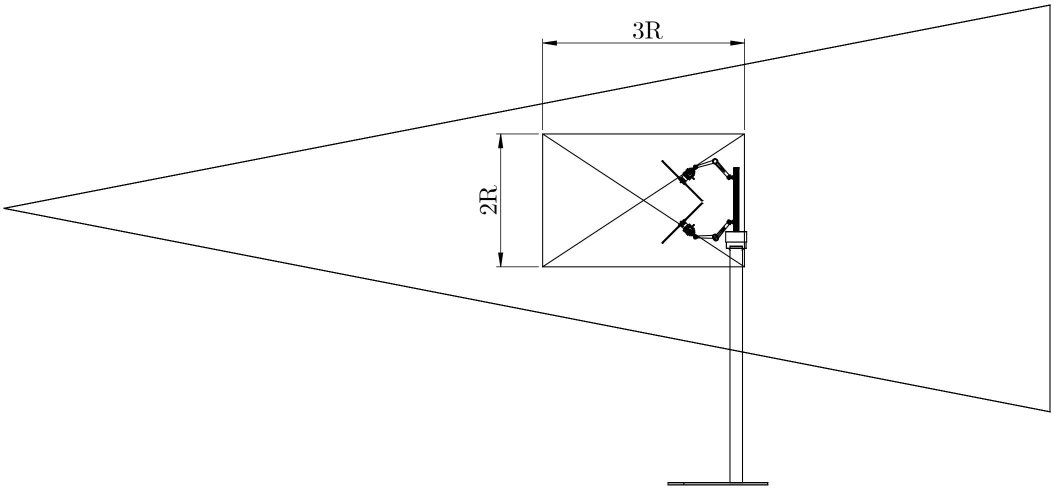

Figure 4.25: PIV interrogation area.

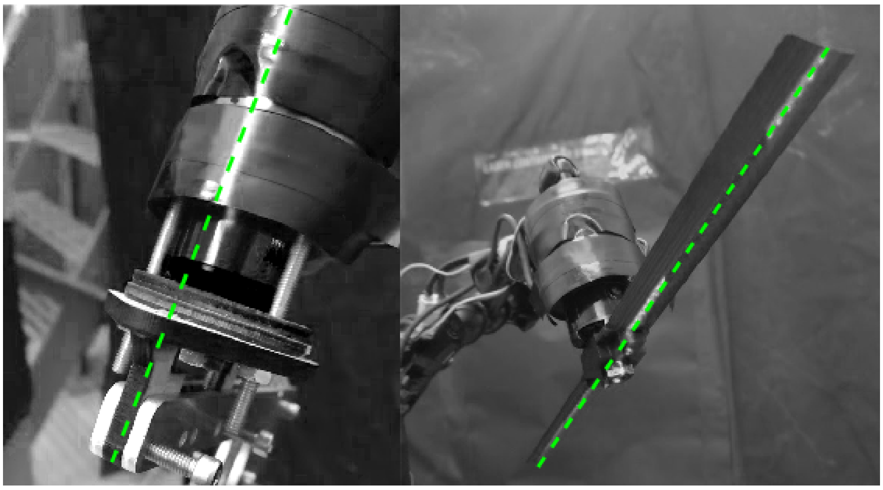

Figure 4.26: Laser alignment with rotor.

significant air flow. Two black curtains are used as laser power dumps for the light sheet and located at least 10R from the rotor rig as shown in Figures 4.24a and 4.24b. Rotor pitch setting and disc alignment was performed as described in Section 4.4.1.3 and aligned with the laser sheet as shown in Figure 4.26. The camera was placed in a slight forward scatter position to increase the signal level of the seed particles, the interrogation window is shown in Figure 4.25.

An LaVision supplied calibration plate was used to provide a spatial calibration of the set-up and remove any lens or perspective distortion. The seeding generator was started and given sufficient time to seed the test area whilst the rest of the system was initialised.

LaVision's DaVis software was used to operate the PIV system and was configured to take a double frame exposure with an interframe time, ΔT, of 250 μS or 500 μS. Varying the interframe time tailors the PIV for either the high velocity outflow or lower velocity inflow. For experiments that include inflow and outflow the lower ΔT value was used.

The rotors were then accelerated to the desired power level and 100 frame pairs were captured at 10 Hz. Force and torque data was simultaneously captured to allow for comparison between flow field and thrust. The rotors were then halted and reconfigured for the next test point.

4.5 Data reduction

4.5.1 Filtering and rejection

Grubbs' test for outliers is used to detect anomalies in recorded data. Applied to raw data the test is particularly useful in identifying discrepancies in data due to errors in the data capture process such as insufficient settling times. Drift between the start and finish of the sampling windows was monitored and highlighted if it exceeded 2%. All identified data was reviewed and rejected if necessary.

The raw data recorded from the force balances, current sensors, and voltage sensors is averaged over a 5000 sample period to obtain a single time averaged data point. Grubbs' outlier test is applied again to identify outliers arising from systematic errors such as physical movement of the rig, drift due to excessive heating of the balances, or changes in supply voltage to the current sensors. The rotational rate of both discs is verified by cross referencing rates from the

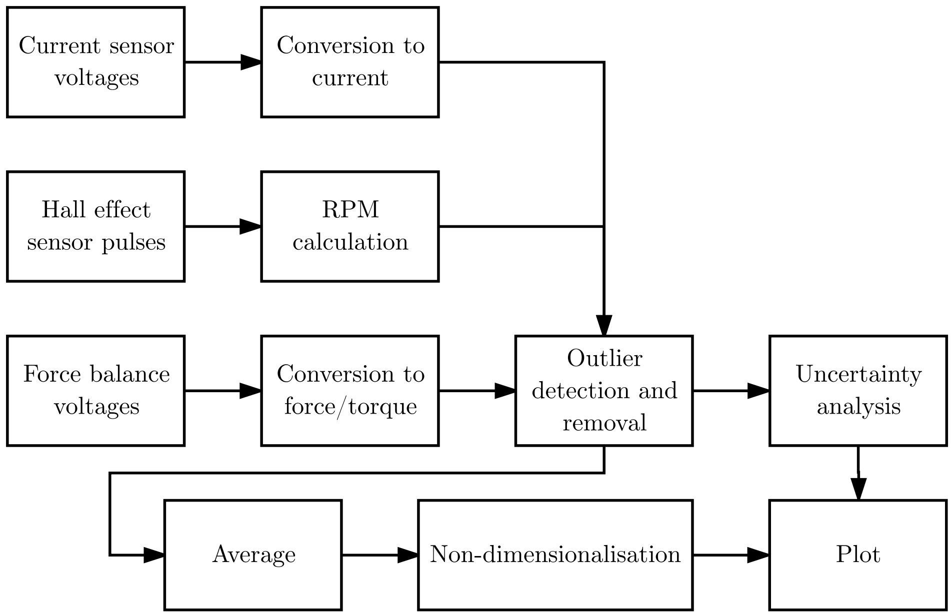

Figure 4.27: Data Processing.

hardware counters with periods calculated from the analogue data measurement of the hall sensors.

4.5.2 Data transformation

Time averaged voltages from the force balances are converted to forces and torques through application of the manufacturer supplied calibration matrix. The balances are biased by subtracting forces and torques measured whilst both rotors are quiescent. The biasing is repeated using zero thrust points throughout the experiment to account for drift due to force balance heating. Force data is used to verify the balances are correctly aligned across their X-Z plane.

Voltages from the current sensor are converted through application of the manufacturer supplied transformation function.

$$I = \frac{V_{cc} - (0.1 * V_{cc})}{0.133}$$

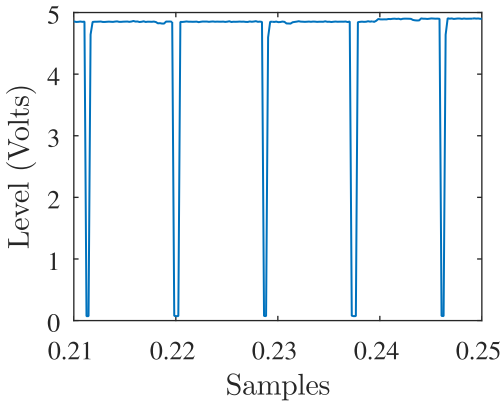

(a) RPM hall sensor signal

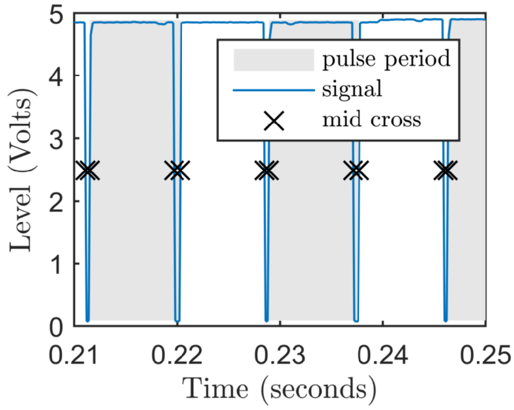

(b) Calculating pulse period from signal

Figure 4.28: RPM signal validation.

4.5.3 Nondimensionalisation of results

It is useful to normalise experimental results to aid comparison between test cases. As discussed in Section 3.1.3 forces and torques are normalised by rotor tip speed, and overall efficiency of the rotor is quantified as the Figure of Merit.

4.5.4 Particle Image Velocimetry

The raw images captured during the PIV investigation required significant processing and reduction. Each set of 100 pairs of image frames was initially processed using LaVision's DaVis 8 software. Vector calculation was carried out using the multipass methodology with a final interrogation window of 32x32px and a 75% window overlap. These settings are computationally expensive but provide a high resolution vector field. For primary analysis the vector field was averaged over the entire test period, with further post processing carried out using TecPlot and MATLAB.

A raw frame from the PIV investigation is included as Figure 4.29. The case being imaged is of a coaxial rotor orientation with both rotors operating at full power demand. Even before processing the wake of the rotors is easily

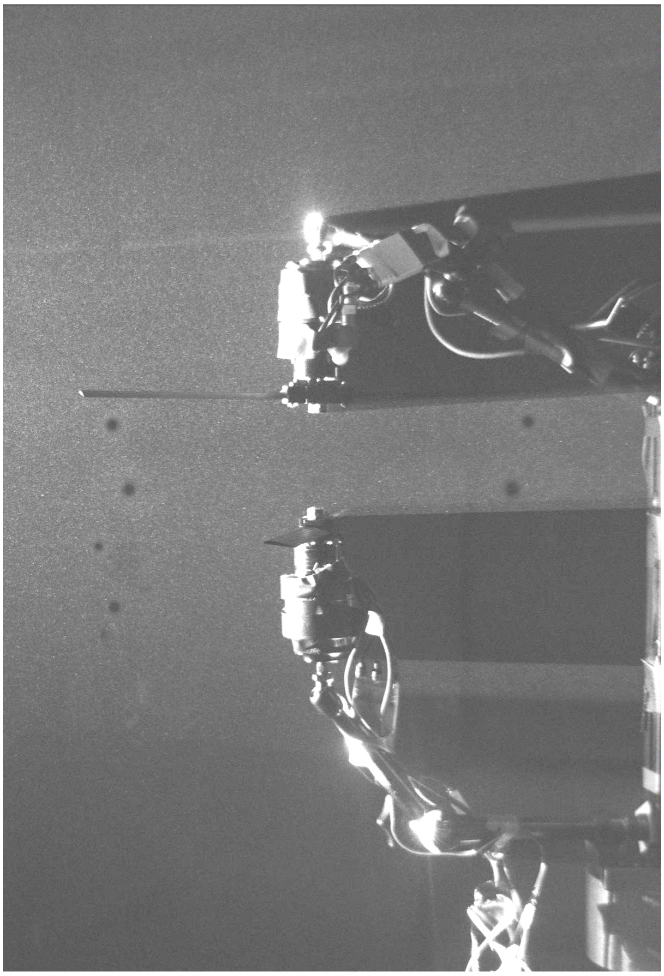

Figure 4.29: Raw image frame from PIV investigation.

recognisable from the location of the descending tip vorticies, where the rotational flow has expelled the seed particles from the region leading to an area of darkness at the vortex core.

The captured frame pairs are processed in DaVis to generate the flow field shown in Figure 4.30, before being filtered for spurious vectors and averaged to create the final vector field shown in Figure 4.31.

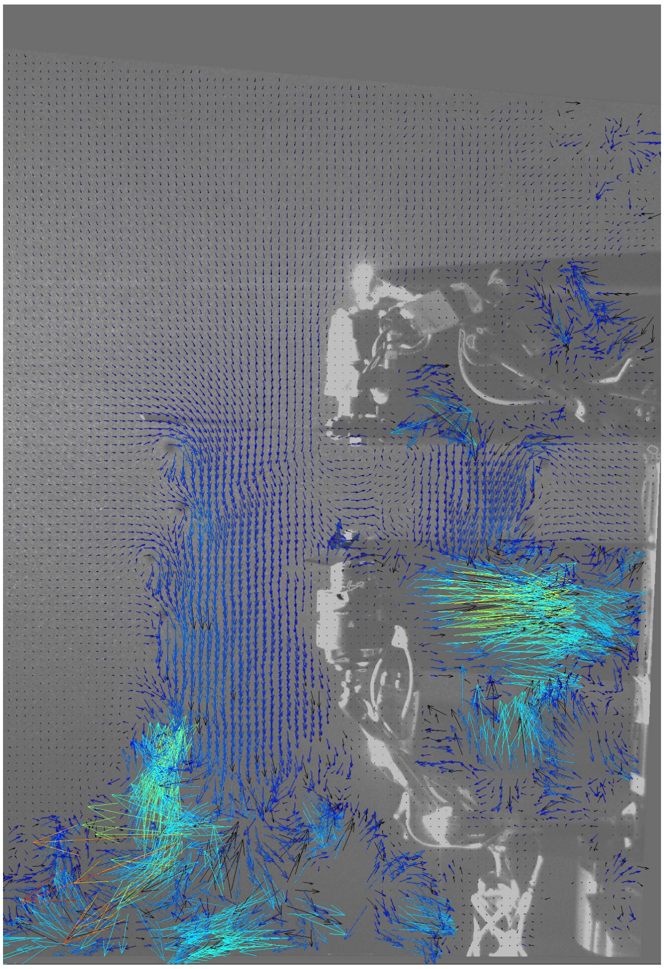

Figure 4.30: Processed vectors for single frame of the PIV investigation.

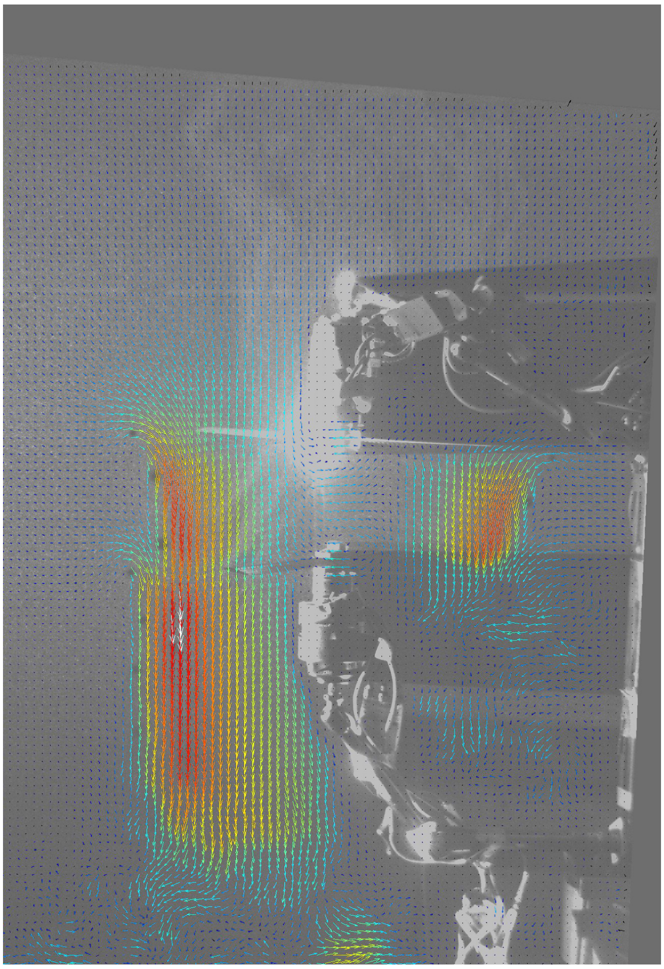

Figure 4.31: Filtered and averaged vectors derived from 100 frames of the PIV investigation.

Figure 4.32: PIV processing workflow.

4.6 Uncertainty Analysis

Uncertainty in the results presented in this thesis is analysed in accordance with JCGM 100:2008 *Evaluation of measurement data - Guide to the expression of uncertainty in measurement* (Jcgm, 2008).

For directly measured quantities, including force/torque, RPM, and current, the uncertainty of the measurand can be determined directly from the uncertainty in the measurement itself. For formulated measurands, such as C_T, uncertainty is propagated from the directly measured quantities.

4.6.1 Type A uncertainty evaluation

The expected value of a quantity, q can be estimated as the average, $\bar{q}$, of n observations (Eq 4.1a). The standard variance of the measured quantity can be calculated as shown in Equations 4.1b and 4.1c. The root of the variance is the uncertainty associated with the measurement of the quantity. This methodology is used to estimate uncertainty for all measured voltages. For quantities measured as voltages by the data acquisition system it is necessary to consider the resolution of the analogue to digital converter. In this investigation a 16bit resolution is used throughout which corresponds to a typical Least Significant Bit (LSB) voltage of $316\mu V$. This uncertainty is negligible compared to the calibration certainties associated with the voltage measurements.

$$\bar{q} = \frac{1}{n}\sum_{i=1}^{n} q_i \tag{4.1a}$$

$$s^2(\bar{q}) = \frac{s^2(q_i)}{n} \tag{4.1b}$$

$$s^2(q_i) = \frac{1}{n-1}\sum_{j=1}^{n}(q_j - \bar{q})^2 \tag{4.1c}$$

4.6.1.1 Force balance measurement

Voltages from the force balances are converted to forces and torques through application of a manufacturer supplied calibration matrix. This calibration matrix has an associated uncertainty for the conversion to absolute force and torque. In this investigation it is the relative change that is of interest rather than the absolute force values and so the uncertainty in the force balance measurement is reduced to that of the data acquisition system. Therefore the uncertainty can be simply quantified through a type A analysis of the measured data.

4.6.2 Type B uncertainty evaluation

4.6.2.1 Rotor blade chord and span

Chord and span of each blade were measured using calipers with a quoted accuracy of ±0.03 mm. Assuming a rectangular probability yields:

$$u(c) \equiv u(b) = \frac{2 * 0.03}{2\sqrt{3}} = 0.017\ mm \tag{4.2}$$

4.6.2.2 Current measurement

The Allegro ACS715 current sensors used in this experiment have a manufacturer quoted accuracy of 1.5% of the full scale measurement of 30 amps, giving an uncertainty of 0.45 amps. As with the force balance measurements, the uncertainty due to analogue to digital conversion is negligible.

$$u(curr) = \frac{2 * 0.45}{2\sqrt{3}} = 0.26\ A \tag{4.3}$$

4.6.3 Uncertainty propagation

For the nondimensional coefficients used in the results analysis uncertainty must be propagated from the directly measured quantities. This involves formulating the relationship between the quantities measured and the measurands, determining the uncertainty associated with quantities measured, and then propagating the uncertainty through the calculation to attain the final uncertainty.

$$C_T = \frac{T}{\rho A(\omega R)^2} \equiv \frac{T}{\rho R^4 \omega^2 \pi} \tag{4.4a}$$

$$C_Q = \frac{Q}{\rho A(\omega R)^2 R} \equiv \frac{Q}{\rho R^5 \omega^2 \pi} \tag{4.4b}$$

The sensitivity of each of the equations shown in Equation 4.4 to the measured quantities can be determined by partially differentiating each equation with respect to each of those measured quantities, shown in Equations 4.5 and 4.6. Dividing through by the original equations gives the relative uncertainties shown in Equations 4.7 and 4.8.

$$\frac{\delta C_T}{\delta T} = \frac{1}{\rho R^4 \omega^2 \pi} \tag{4.5a}$$
$$\frac{\delta C_T}{\delta \omega} = -\frac{2T}{\rho R^4 \omega^3 \pi} \tag{4.5b}$$
$$\frac{\delta C_T}{\delta R} = -\frac{4T}{\rho R^5 \omega^2 \pi} \tag{4.5c}$$

$$\frac{\delta C_Q}{\delta Q} = \frac{1}{\rho R^5 \omega^2 \pi} \tag{4.6a}$$
$$\frac{\delta C_Q}{\delta \omega} = -\frac{2Q}{\rho R^5 \omega^3 \pi} \tag{4.6b}$$
$$\frac{\delta C_Q}{\delta R} = -\frac{5Q}{\rho R^6 \omega^2 \pi} \tag{4.6c}$$

$$\frac{1}{C_T}\frac{\delta C_T}{\delta T} = \frac{1}{T} \tag{4.7a}$$
$$\frac{1}{C_T}\frac{\delta C_T}{\delta \omega} = -\frac{2}{\omega} \tag{4.7b}$$
$$\frac{1}{C_T}\frac{\delta C_T}{\delta R} = -\frac{4}{R} \tag{4.7c}$$

$$\frac{1}{C_Q}\frac{\delta C_Q}{\delta Q} = \frac{1}{T} \tag{4.8a}$$
$$\frac{1}{C_Q}\frac{\delta C_Q}{\delta \omega} = -\frac{2}{\omega} \tag{4.8b}$$
$$\frac{1}{C_Q}\frac{\delta C_Q}{\delta R} = -\frac{5}{R} \tag{4.8c}$$

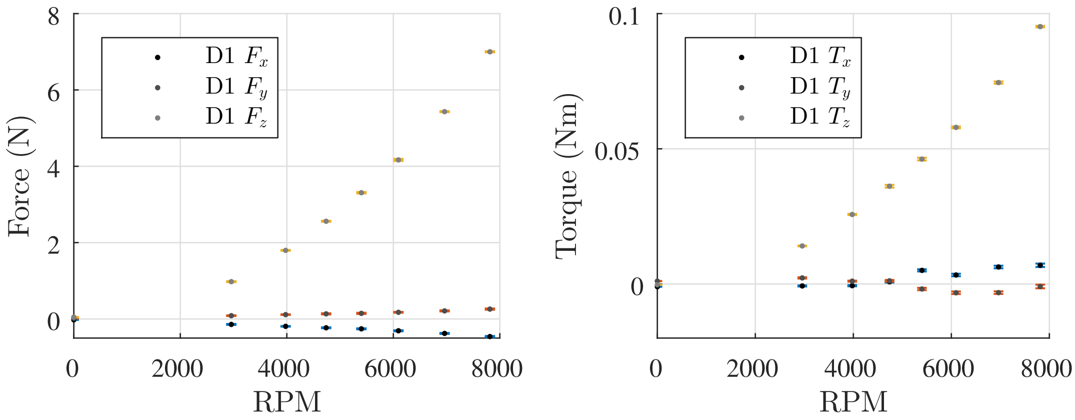

(a) Disc 1 force uncertainty. **(b)** Disc 1 torque uncertainty.

Figure 4.33: Disc 1 force balance measurement uncertainty.

Combining the sensitivity coefficients using the root-sum-square method allows the total uncertainties U_{C_T} and U_{C_Q} to be expressed as in Equation 4.9.

$$\frac{U_{C_T}}{C_T} = \sqrt{\left(\frac{1}{T}U_T\right)^2 + \left(-\frac{2}{\omega}U_\omega\right)^2 + \left(-\frac{4}{R}U_R\right)^2} \tag{4.9a}$$

$$\frac{U_{C_Q}}{C_Q} = \sqrt{\left(\frac{1}{Q}U_Q\right)^2 + \left(-\frac{2}{\omega}U_\omega\right)^2 + \left(-\frac{5}{R}U_R\right)^2} \tag{4.9b}$$

4.6.4 Sample analysis

A sample analysis of the standard experimental uncertainty for force and torque measurements on both disc 1 and disc 2 is shown in Figure 4.33 and 4.34.

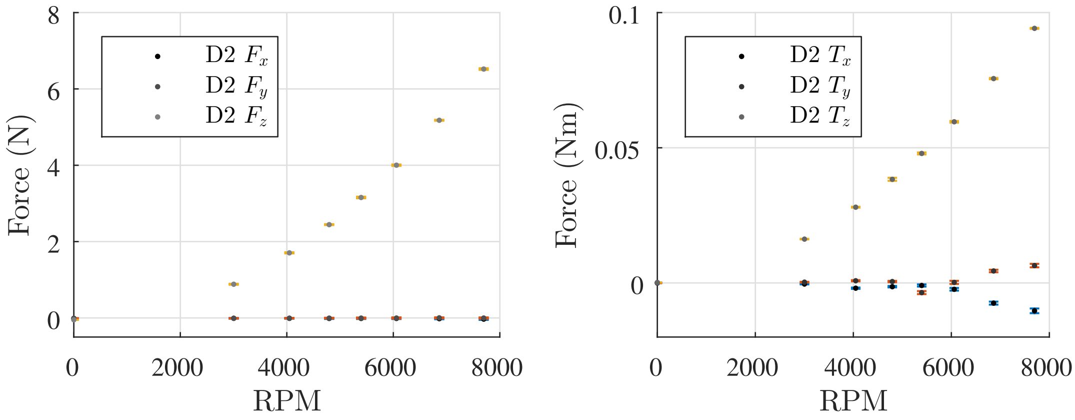

(a) Disc 2 force uncertainty. **(b)** Disc 2 torque uncertainty.

Figure 4.34: Disc 2 force balance measurement uncertainty.

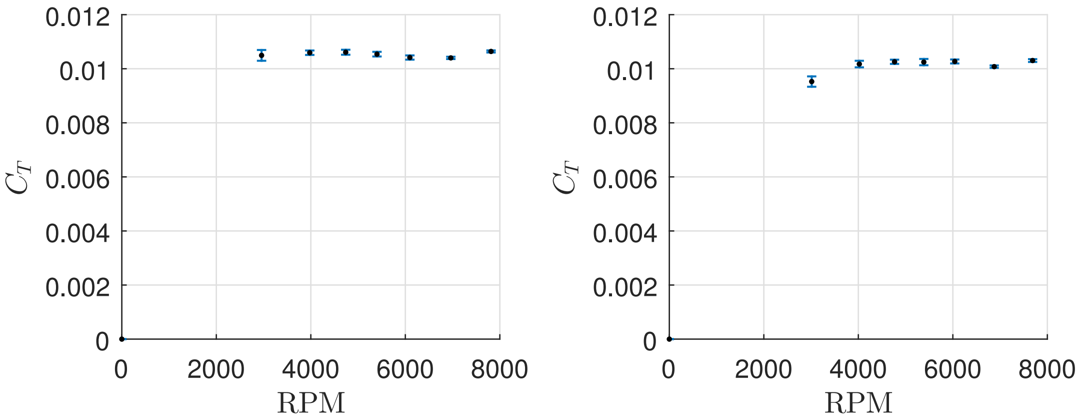

(a) Disc 1 C_T uncertainty. **(b)** Disc 2 C_T uncertaint.y

Figure 4.35: Sample C_T uncertainty analysis.

4.7 Experimental methods conclusions

An adjustable interaction rig was presented and shown to be capable of achieving the desired range of relative disc angles and spacing and meeting the design deflection requirements. The extensible design of the rig allows further disc angles to be investigated with minimal effort, and for additional rotor systems to be added if desired.

A methodology for collecting time averaged steady state performance data for one or more rotors has been presented. The methodology describes the data acquisition, filtering, and reduction required to obtain repeatable results. An uncertainty analysis was carried out which revealed the uncertainty level for raw force and torque data was low. Uncertainty in the force and power coefficients is higher, with further increased uncertainty at low disc loading. The levels of uncertainty shown by the analysis are acceptable for this investigation.

A nonintrusive method for acquiring instantaneous whole field velocity data using PIV was introduced. The limitation of the two-dimension two-component system used in accurately measuring flow regions with high three-dimensionality, such as near a rotor, is noted. With the available PIV equipment the interrogation window is not large enough to encompass the full region of interest at disc angles above 120 degrees. As the level of interaction between the discs at this angle is small this will not limit the PIV investigation.

Data acquired using the setup and methodologies detailed in this section is suitable for comparison with CFD as long as some considerations are made. The trailing edge of the custom rotor blades is fragile and can be easily damaged. The final shape of the rotor blades used in the experiment is a slightly truncated version of the design as shown in Figure 4.4c.

This experiment considers co-rotating coaxial rotors, rather than the conventional contra-rotating, as a consequence of the rig design. This deviation will result in reduced efficiency compared to a conventional contra-rotating coaxial rotor system, however, this is considered an acceptable compromise for this experiment.

Chapter 5

Results

5.1 Summary

The figures in this section summarise the force and flow field data gathered in the investigation. For each disc a thrust vector is displayed in black starting from the rotor hub. This vector is constructed from the mean of the force components, $[\overline{F_x}, \overline{F_y}, \overline{F_z}]$, measured during the primary force/torque experiments and is normalised against the magnitude thrust vector for the disc operating in isolation which is shown in grey. Only the F_x and F_z components of the thrust vectors are shown as these are the most significant with the majority of the thrust vector being generated in F_z whilst changes in thrust line due to disc interaction primarily be seen in F_x.

Forces for each rotor are displayed relative to the respective balance reference frame where the X-axis lies parallel to the rotor and the Z-axis is coaxial with the motor shaft, as shown in Figure 5.1.

In these results a rotor is said to be operating in either a 'pull' or 'push' configuration. In a 'pull' configuration the rotor is acting to generate force in the positive F_z direction relative to the balance reference frame, whilst in the 'push'

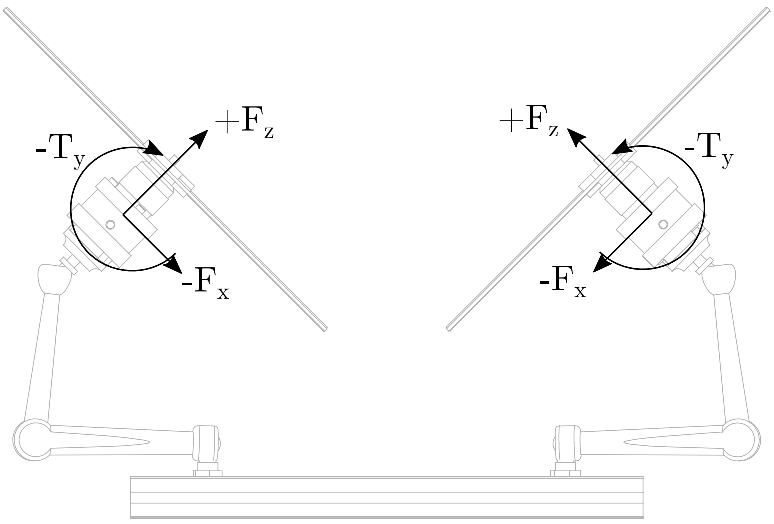

Figure 5.1: Force balance reference frames.

configuration the rotor is acting to generate force in the negative F_z direction relative to the balance reference frame.

Streamlines derived from the PIV experiments are overlaid to provide flow field data and are coloured by velocity magnitude. A slight bias is seen in the flow data at lower disc angles due to a marginally higher (approximately 7%) maximum thrust generated by the right side disc. This effect is particularly visible in Figures 5.5c, 5.6c and 5.7c. Areas of the PIV interrogation area were shielded from the laser light source by the physical structure of the rig, these are omitted. Other areas were intermittently illuminated as the blades rotated, or poorly illuminated due to the sharp roll off in laser power towards the edge of the interrogation area. Vectors in these areas are retained, however they are masked off to indicate the lower level of confidence.

Figure 5.2 presents the 180 degree co-planar cases which are used to provide a baseline throughout the results section. Experimentally derived streamlines are not available for this case as the interrogation window is not large enough to encompass the area around both rotor discs. As is to be expected the thrust vectors for both the ‘Pull Pull’ and ‘Push Push’ cases differ minimally from the

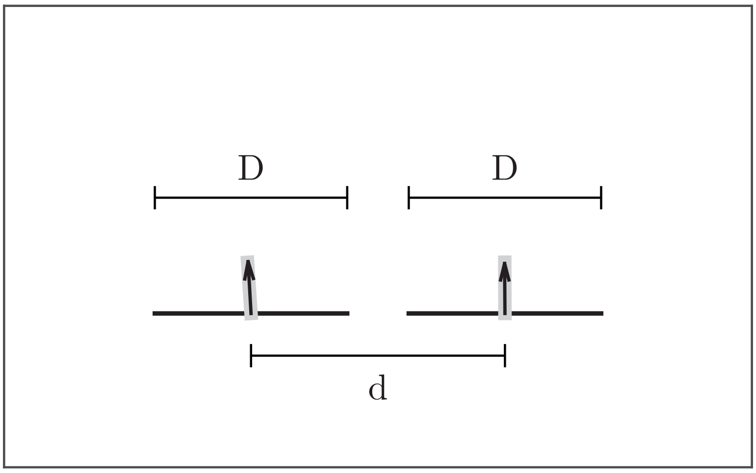

(a) Pull Pull

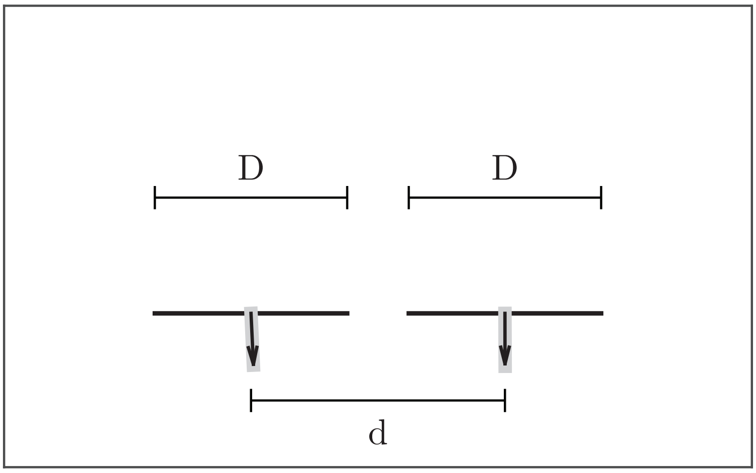

(b) Push Push

Figure 5.2: 180 degree results summary.

benchmark case. The co-planar case may be considered alongside other work, such as Brazinskas et al. (2016), in which case it is useful to understand the ratio between disc diameter and disc overlap. In this case, where tip spacing is 40mm, $d = 310\ mm$ and $D = \ 270mm$, the overlap ratio $\frac{d}{D} = 1.15$.

Disc angle is reduced to 120 degrees in Figure 5.3. For the 'Pull Pull' and 'Push Push' cases minimal change in thrust is seen and for the 'Pull Push' case a slight reduction in thrust is seen for the pushing disc. Flow field data for the 'Pull Push' case shows a slight shifting of the outflow from the 'Push' disc, however the effect of this is not visible in the force data.

At a 90 degree disc angle, as shown in Figure 5.4a, the interaction between ‘Pull’ and ‘Push’ discs starts to become significant with clear changes to the outflow of the ‘Push’ disc and inflow to the ‘Pull’ disc. This is reflected in the force data with the pusher and puller discs exhibiting a 5% decrease and increase of thrust respectively. A negative torque around the y-axis is measured on both discs and a potentially corresponding increase in speed can be seen in one half of pusher disc outflow.

Thrust starts to become significantly affected by the flow interactions at a disc angle of 60 degrees, Figure 5.3. The ‘Pull Pull’ and ‘Push Push’ cases show an increase in thrust for both discs of approximately 7%. In the ‘Pull Push’ case no change in thrust is seen for the pushing disc whilst the pulling disc sees a reduction in thrust of approximately 17%. There is also a clearly visible change in thrust angle for the puller disc and a negative torque around the y-axis for both discs.

At a disc angle of 30 degrees thrust is increased by approximately 18% for both discs for the ‘Pull Pull’ case. For the ‘Push Push’ case thrust has become asymmetric, with the left hand disc generating approximately 15% more thrust whilst the right hand disc generates approximately 20% more thrust. The difference between maximum thrust level on the discs is significantly larger than seen in the baseline tests. In the ‘Pull Push’ case flow field data shows the puller disc is now fully in the wake of the pusher disc. The thrust of the puller has been reduced to 67% of the baseline level whilst the pusher disc remains unchanged. As with the previous cases a negative torque around the y-axis is present for both discs.

Figure 5.7 summarises experimental data from the 0 degree disc angle, or coaxial, case. An increase in thrust of approximately 23% is seen for both discs

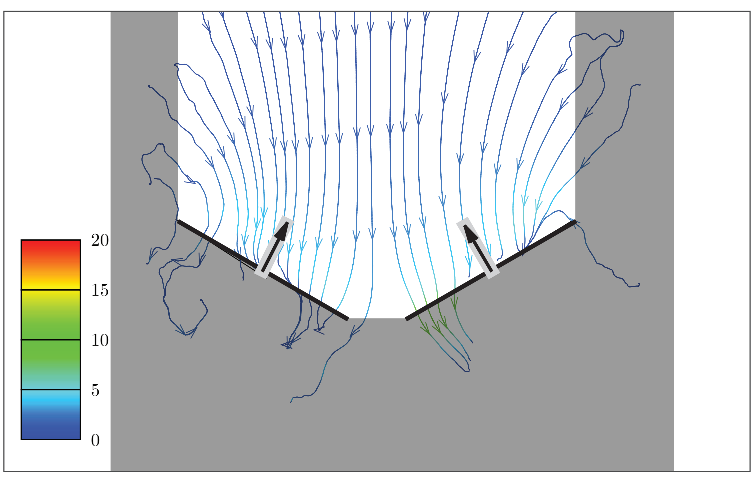

(a) Pull Pull

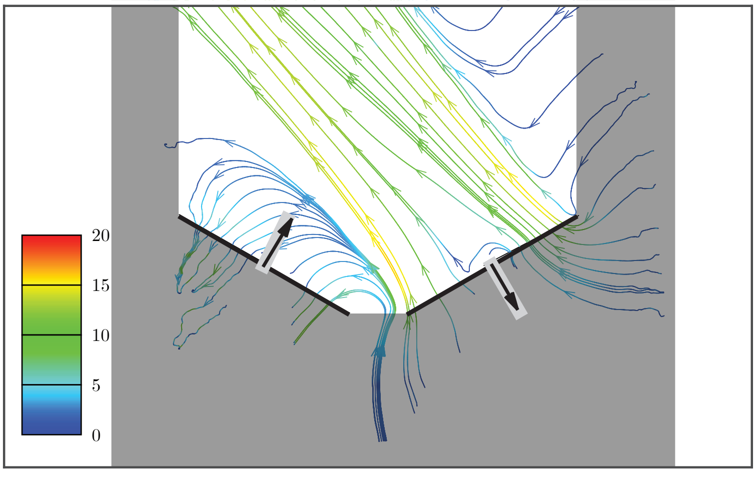

(b) Pull Push

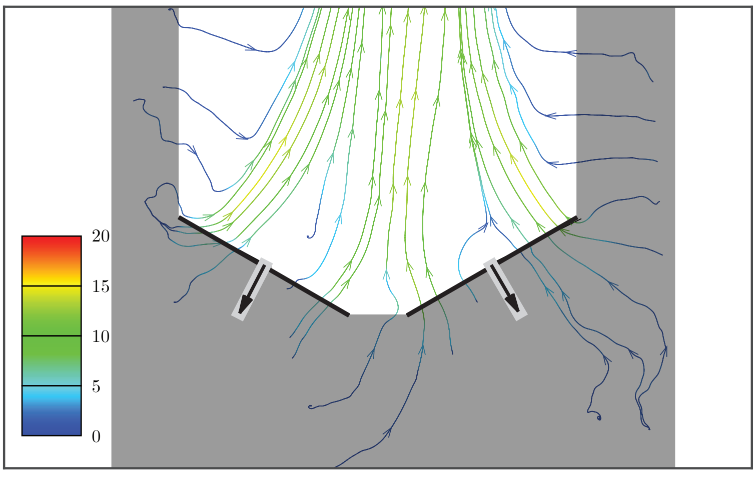

(c) Push Push

Figure 5.3: 120 degree results summary.

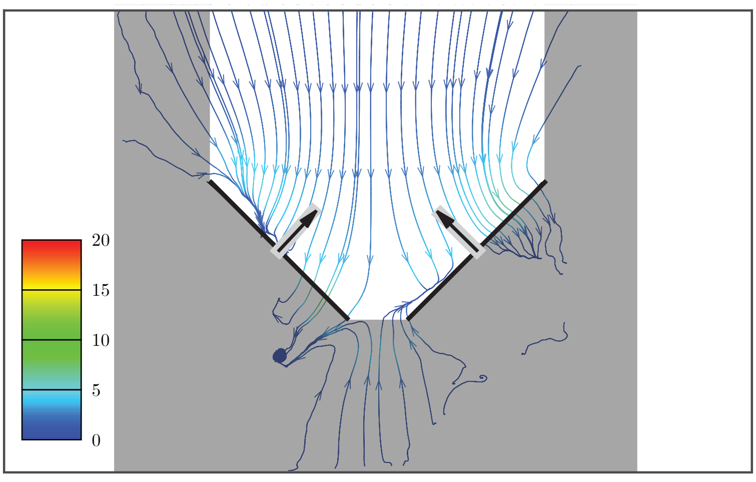

(a) Pull Pull

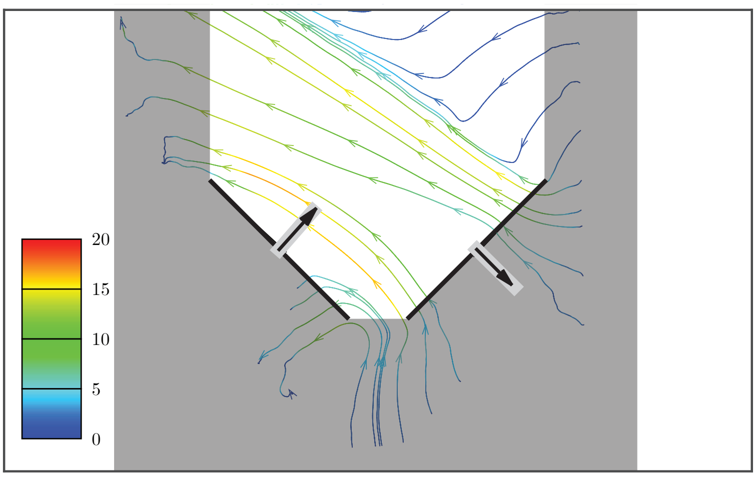

(b) Pull Push

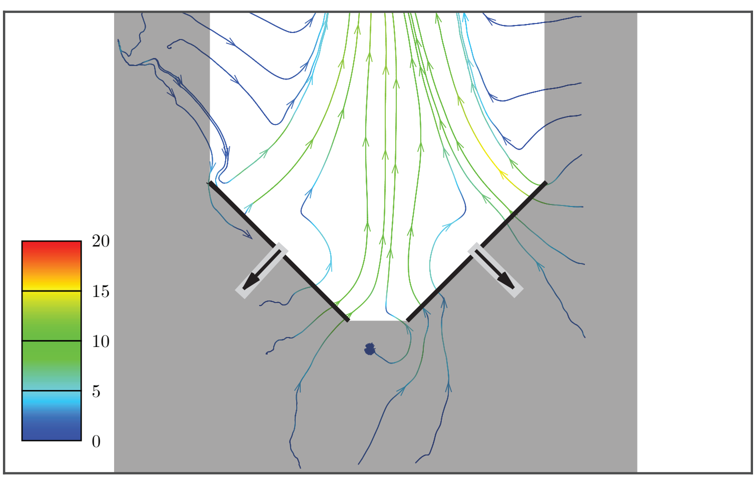

(c) Push Push

Figure 5.4: 90 degree results summary.

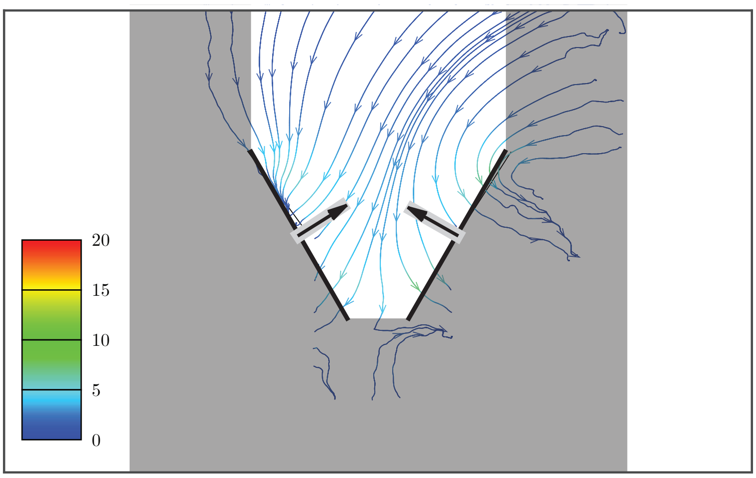

(a) Pull Pull

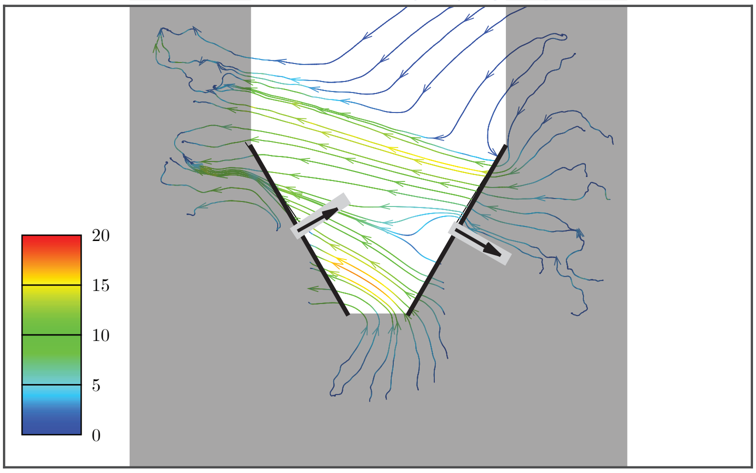

(b) Pull Push

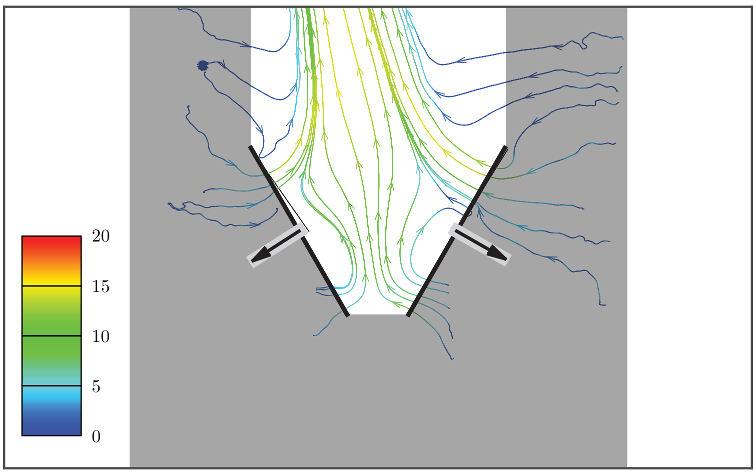

(c) Push Push

Figure 5.5: 60 degree results summary.

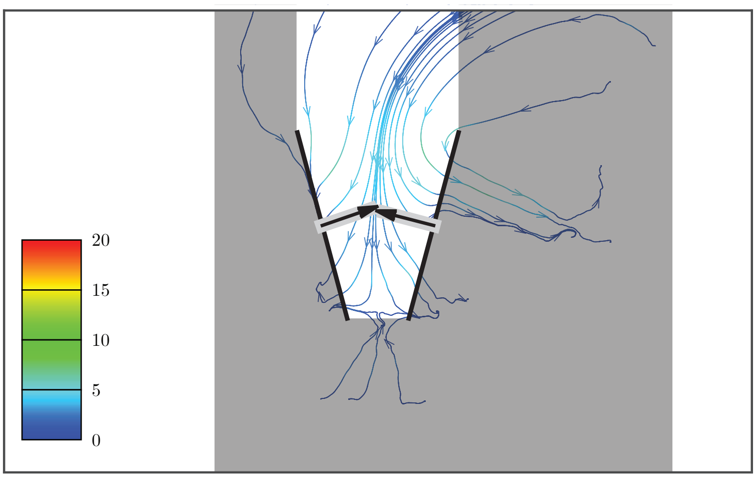

(a) Pull Pull

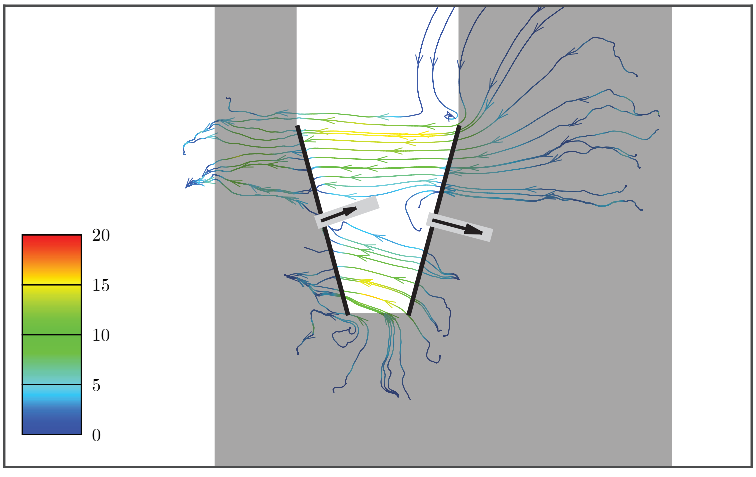

(b) Pull Push

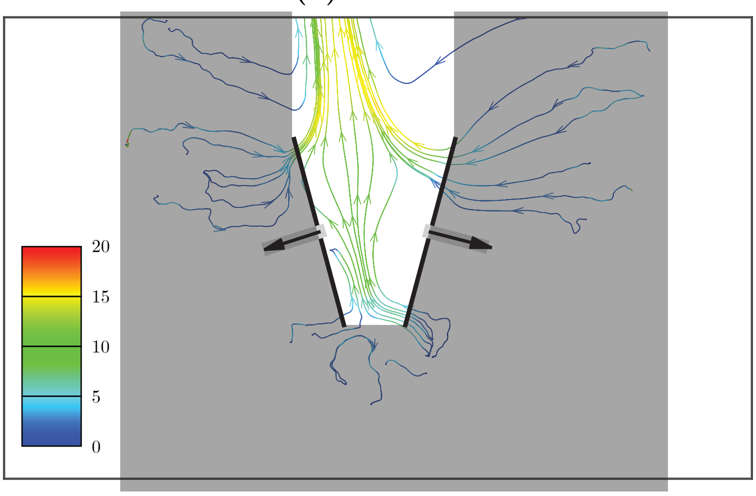

(c) Push Push

Figure 5.6: 30 degree results summary.

in the 'Pull Pull' case. The flow field in the 'Pull Pull' case shows strong agreement with coaxial rotor flow fields detailed in literature. Thrust increase in the 'Push Push' is asymmetric, as in previous cases, with the left hand disc seeing an approximate increase in thrust of 35% and the right hand disc seeing an approximate increase of 45%. In the 'Pull Push' case the pusher disc continues to exhibit no change in thrust whilst the puller disc has a similar thrust reduction to that seen at 30 degrees. No meaningful torque around the Y-axis is measured for either disc.

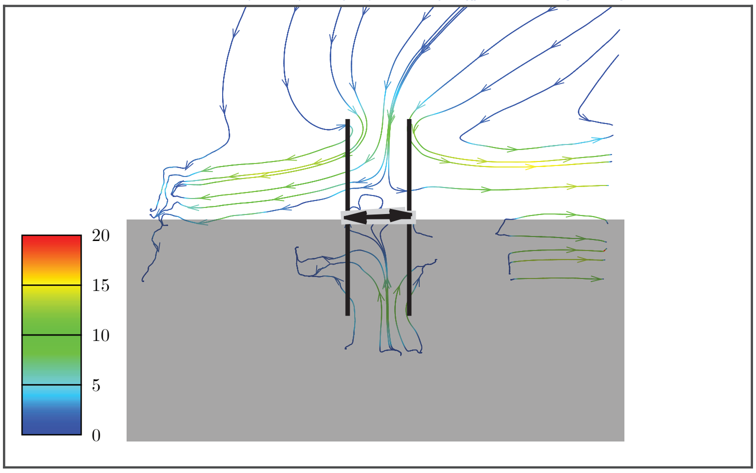

(a) Pull Pull

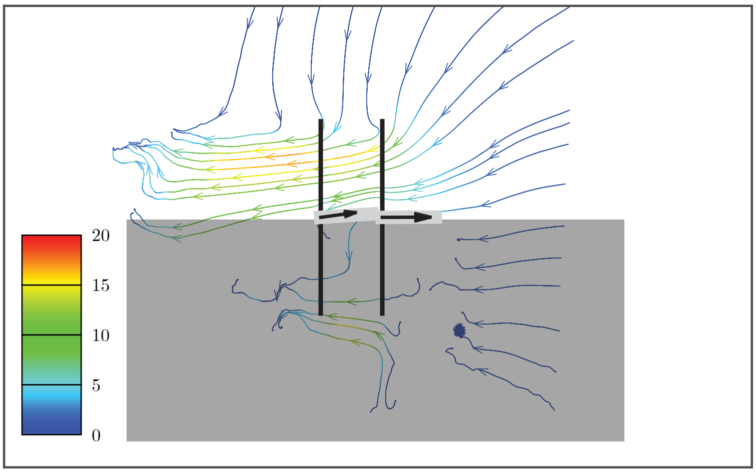

(b) Pull Push

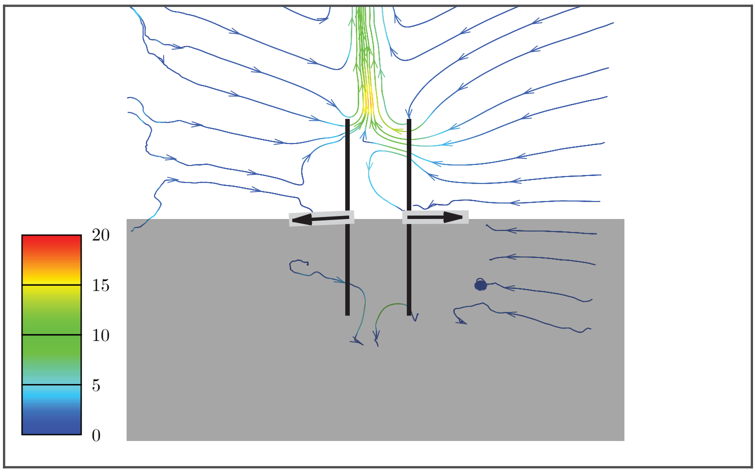

(c) Push Push

Figure 5.7: 0 degree results summary.

5.2 Force and Torque Data

5.2.1 Baseline performance

Force data in this investigation is presented normalised against the maximum thrust generated by the specific rotor operating in isolation. A baseline level for Thrust and Torque was established from the '180 deg' case where the rotors are operating in plane with a tip spacing of 0.3R, or 40 mm. Both 'pulling' and 'pushing' configurations are considered and the results are presented in Tables 5.1 and 5.2 and Figures 5.9 and 5.10.

5.2.1.1 Comparison to BEMT model

A comparison between experimental data and BEMT derived estimates is presented in Figure 5.8a. The BEMT estimate is based on aerofoil data calculated using XFoil as discussed in Section 3.1.2. The estimate is based on the ideal profile shown in Figure 4.4a and a blade setting angle of 8 degrees. The experimental setup differs slightly with a setting angle of approximately 7.94 degrees, based on the measurements in Table 4.2, and slightly truncated blade profile resulting from the manufacturing process, as shown in Figure 4.4c.

The BEMT derived thrust and C_T values show good agreement with the experimental data, however at the maximum achievable experimental RPM the model underestimates thrust by approximately 9% and C_T by approximately 7%. This variation may be in part due to the difference in blade setting angle and differences in blade profile. The deviation between experiment and theory in this investigation is markedly reduced compared to that seen by Langkamp (2011),

However the strong correlation between experimental and theoretical data indicates that aerodynamic properties for the manufactured blades can be modelled by currently available methods.

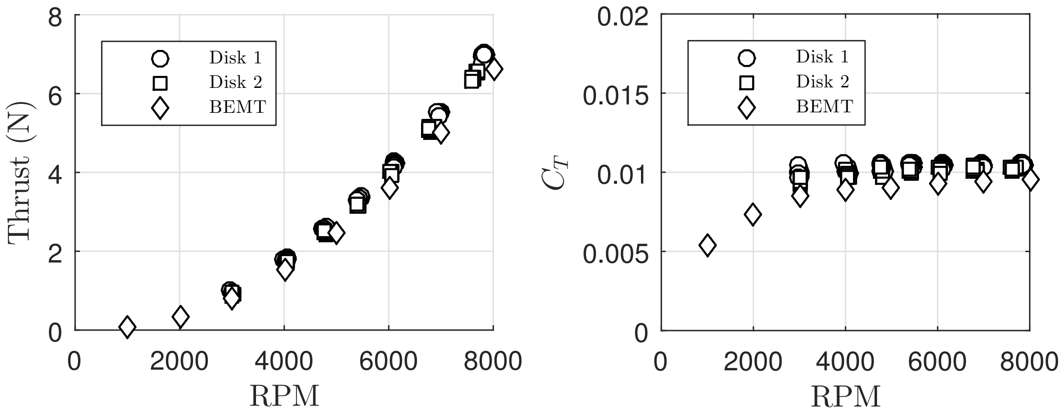

(a) Thrust comparison. **(b)** C_T comparison.

Figure 5.8: Comparison between BEMT and experimental results.

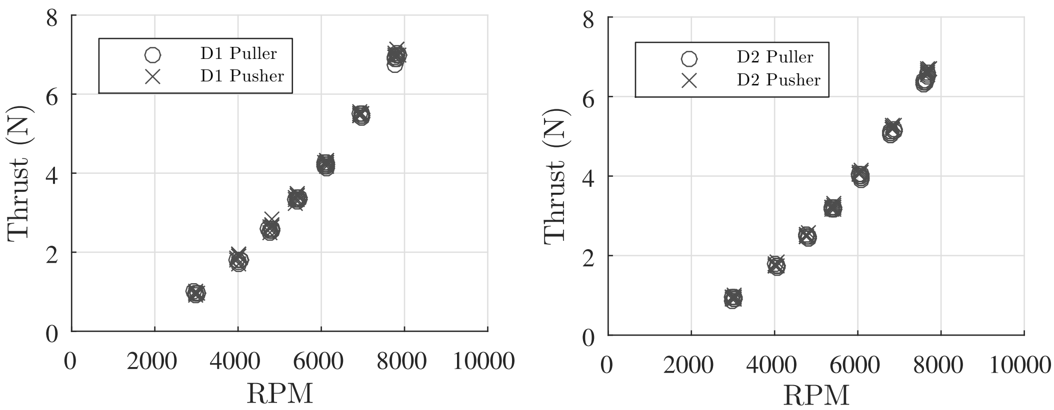

(a) Disc 1. **(b)** Disc 2.

Figure 5.9: Establishing baseline thrust values.

Table 5.1: Baseline thrust and torque values.

	Thrust [N]		Torque [N.m]	
	Mean	Std	Mean	Std
Disc 1 Pull	6.93	0.077	0.095	8.1×10^{-4}
Disc 1 Push	7.00	0.070	0.097	4.9×10^{-4}
Disc 2 Pull	6.43	0.097	0.093	9.7×10^{-4}
Disc 2 Push	6.63	0.055	0.095	3.6×10^{-4}

Table 5.2: Baseline thrust and torque coefficients.

	C_T		C_Q	
	Mean	Std	Mean	Std
Disc 1 Pull	0.0103	2.5×10^{-4}	0.0012	2.0×10^{-5}
Disc 1 Push	0.0106	3.5×10^{-4}	0.0012	1.3×10^{-4}
Disc 2 Pull	0.01	2.9×10^{-4}	0.0012	4.1×10^{-5}
Disc 2 Push	0.0102	2.7×10^{-4}	0.0012	4.3×10^{-5}

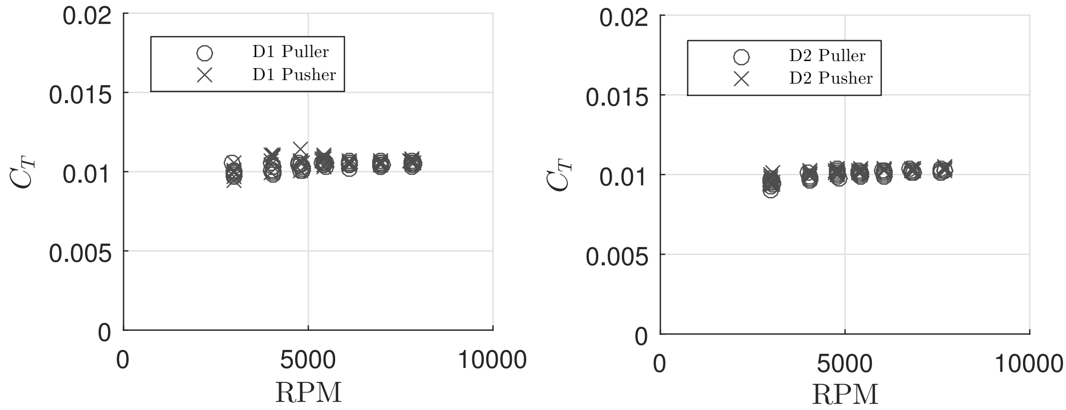

(a) Disc 1 **(b)** Disc 2

Figure 5.10: Establishing baseline C_T values

5.2.2 Influence of disc angle on thrust

To quantify the direct effect of disc angle on thrust generation the thrust magnitudes of disc 1 and disc 2 are normalised against the thrust magnitude of each rotor operating in isolation using the data from Section 5.2.1.

Figure 5.11 presents a series of normalised thrust maps for each rotor configuration. Whilst this gives a good overview of the change in thrust with disc angle, the relationship can be more easily visualised by plotting the normalised peak thrust of each disc against the disc angle, as shown in Figure 5.12.

For the 'Pull Pull' configuration where the discs share an inflow region, Figures 5.11a and 5.12a, little variation is seen in thrust between disc angles of 180 degrees and 90 degrees. As disc angle decreases past 90 degrees to 0 degrees, the coaxial case, normalised thrust increases significantly to $\sim$1.23.

Figures 5.11c and 5.11b present thrust maps for 'pull push' and 'push pull' configurations where one rotor is ingesting the wake of the other. As with the 'pull pull' configuration disc angles between 90 degrees and 180 degrees show minimal change in normalised thrust. As disc angle is reduced towards the coaxial case the normalised thrust on the pulling disc ingesting the flow of the pusher disc is reduced to around 0.6. Considering the results again in Figures 5.12c and 5.12d reveals a 4-6% increase in thrust for the puller disc between disc angles of 120 degrees and 90 degrees, before thrust starts to drop off.

The 'Push Push' configuration is considered in Figure 5.11d and 5.12b. As before no significant variation in thrust is seen between disc angles of 180 and 90 degrees. As the disc angle is reduced past 90 degrees normalised thrust generation for both discs increases to a maximum of 1.4.

All four cases considered above indicate that interactions between disc angles of 180 and 90 degrees have minimal impact on thrust generation for either disc. As the disc angle is reduced towards 0 degrees the impact on thrust generation rises significantly.

5.2.3 Influence of disc angle on rotor moments

The relationship between rotor moments and disc angles for the considered cases are presented in Figures 5.13 and 5.14. Moments are presented as non-dimensional coefficients, C_{Q_x} and C_{Q_y}, using the methodology described in Section 3.1.3. Both rotors are operating at maximum power demand.

Figure 5.13 shows that, whilst there is some variation seen in C_{Q_x}, there is no clear trend against disc angle. The variation seen is likely a result of slight errors in disc alignment.

In contrast the results presented in Figure 5.14 display a strong correlation

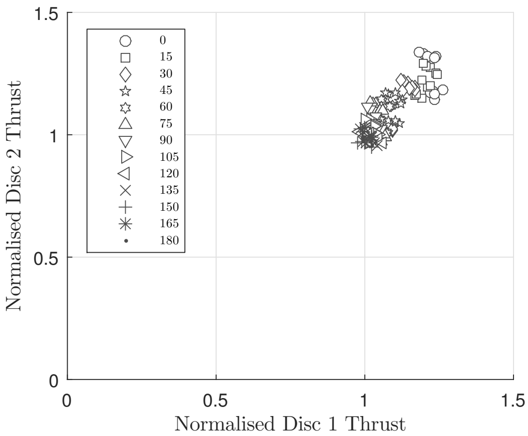

(a) ‘Pull’ ‘Pull’ configurations.

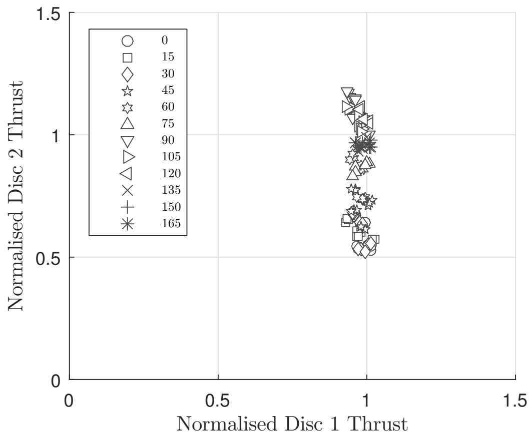

(b) ‘Push’ ‘Pull’ configurations.

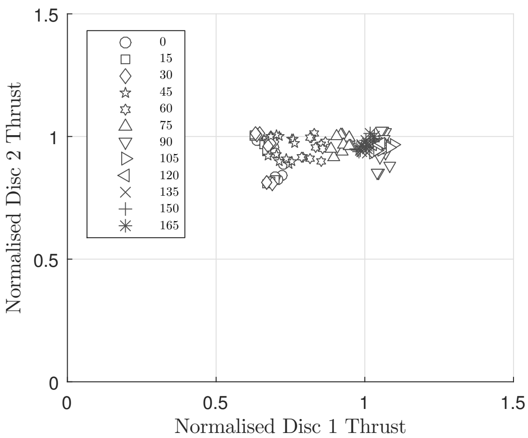

(c) ‘Pull’ ‘Push’ configurations.

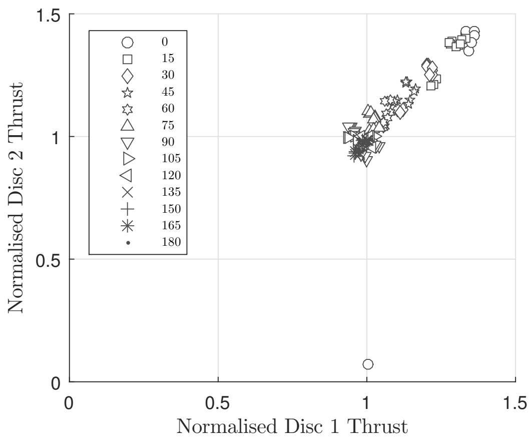

(d) ‘Push’ ‘Push’ configurations.

Figure 5.11: Thrust maps for rotor configurations as disc angle changes.

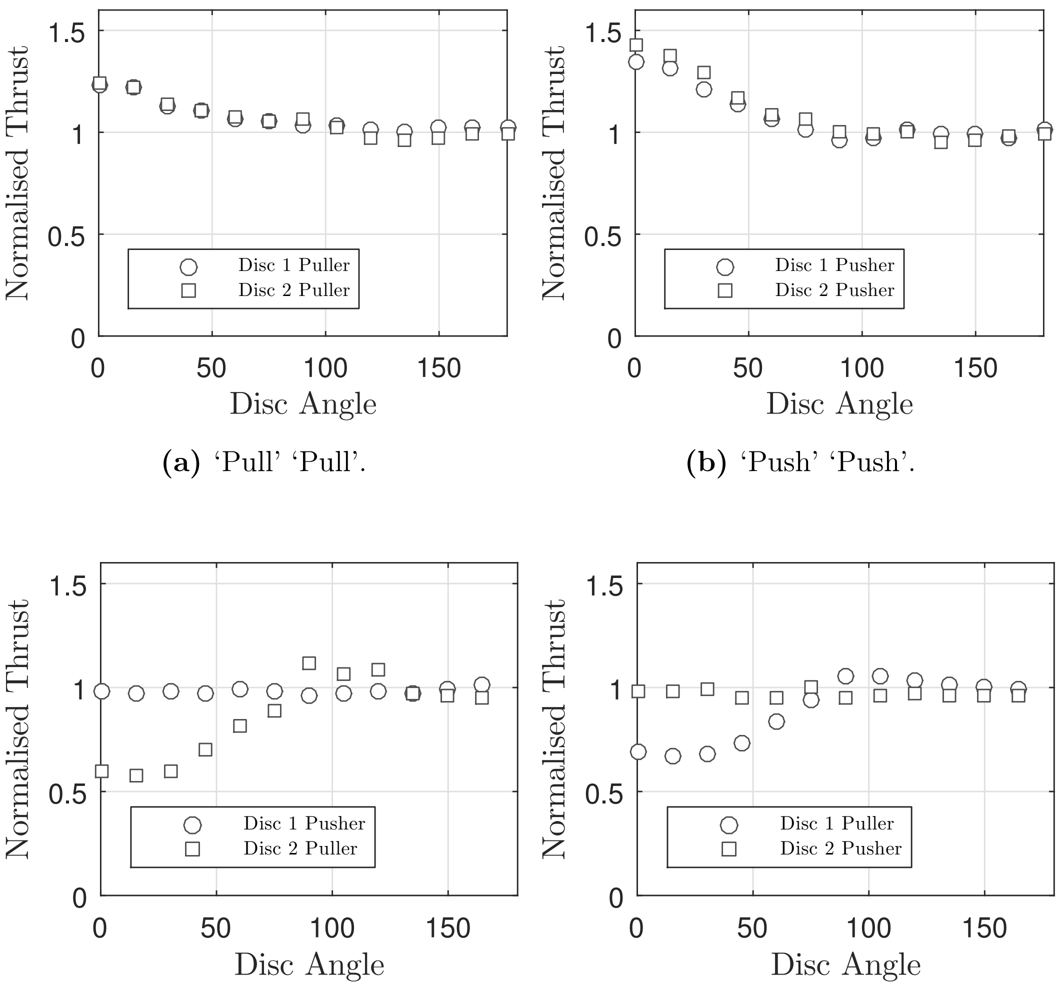

(a) ‘Pull’ ‘Pull’.

(b) ‘Push’ ‘Push’.

(c) ‘Push’ ‘Pull’.

(d) ‘Pull’ ‘Push’.

Figure 5.12: Influence of disc angle on thrust for different rotor configurations.

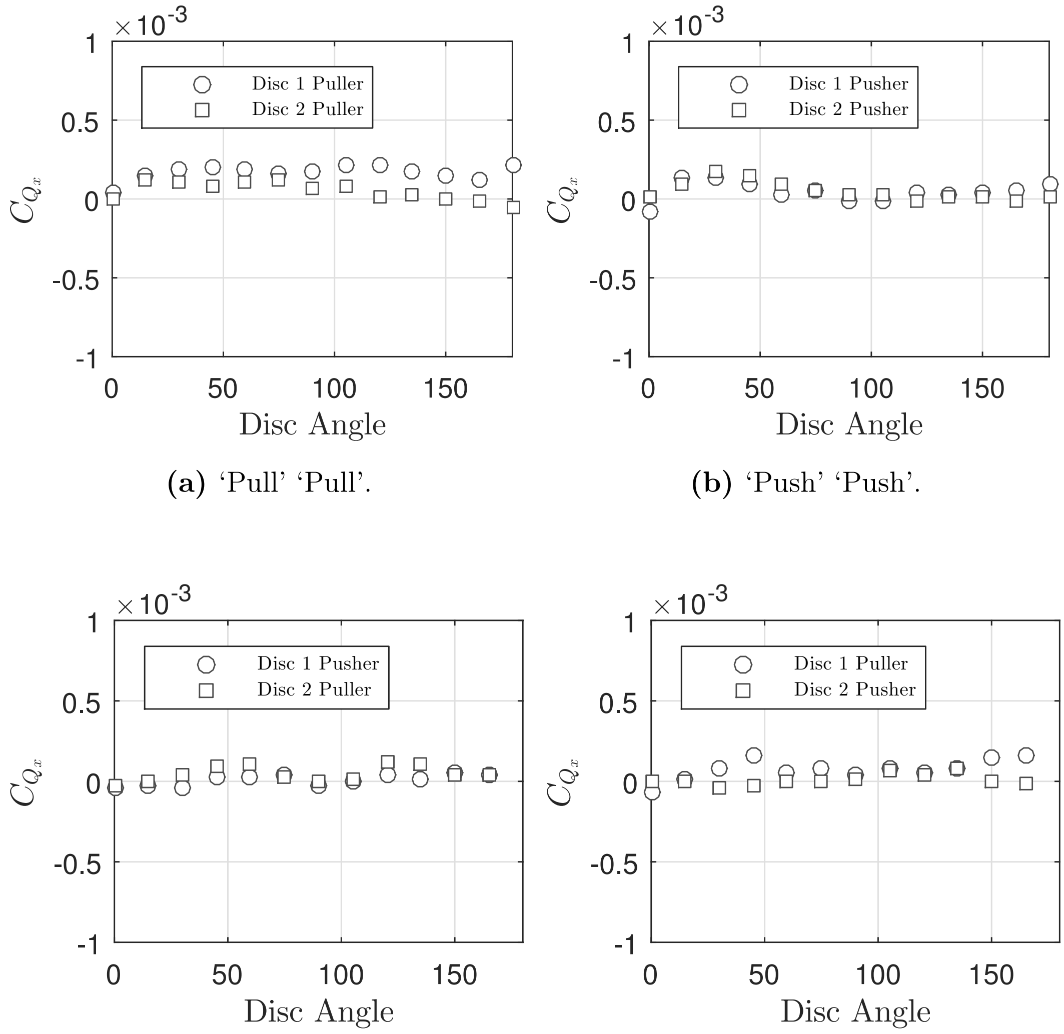

(a) ‘Pull’ ‘Pull’.

(b) ‘Push’ ‘Push’.

(c) ‘Push’ ‘Pull’.

(d) ‘Pull’ ‘Push’.

Figure 5.13: Influence of disc angle on C_{Q_x} for different rotor configurations.

between C_{Q_y} and disc angle. Significant changes in C_{Q_y} are seen in the ‘Push Pull’ and ‘Pull Push’ cases where the puller disc exhibits a strong positive moment coefficient about the Y axis between disc angles of 75 and 30 degrees. This positive moment is acting to rotate the pulling rotor away from the pushing rotor. The moment coefficient decreases quickly to near zero as the disc angle reduces towards the coaxial configuration.

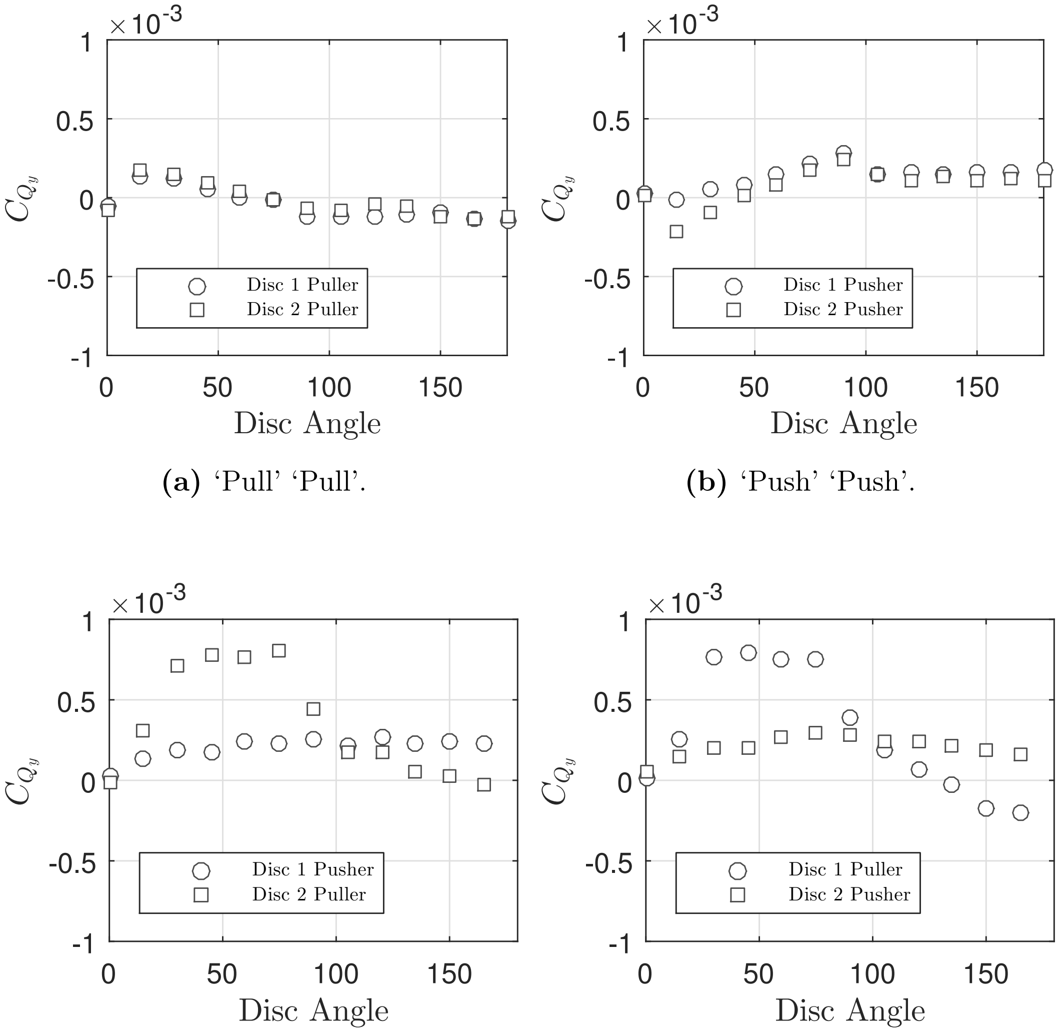

(a) 'Pull' 'Pull'.

(b) 'Push' 'Push'.

(c) 'Push' 'Pull'.

(d) 'Pull' 'Push'.

Figure 5.14: Influence of disc angle on C_{Q_y} for different rotor configurations.

5.2.4 Influence of disc angle on rotor efficiency

The power requirements of a rotor disc can be quantified through measurement of the reactive torque of the BLDC motor using the force/torque balance. The measured torque is then non-dimensionalised against RPM to derive a torque coefficient, C_Q, which is equivalent in magnitude to the power coefficient C_P. As the investigation considers both clockwise and anti-clockwise motor rotation, the sign of C_Q changes depending on whether the rotor is in a push or pull configuration. Unless otherwise noted the absolute value of C_Q will be used.

Considering the change in C_Q with disc angle, as presented in Figure 5.15, is insufficient as it does not account for the change in thrust also present in the experiment. The FOM was introduced in Section 5.2.1 as a method of quantifying the efficiency of a rotor. As the FOM is only suitable for comparison between rotors at a similar disc loading it is necessary to interpolate the available set of data to extract values of FOM for a continuous thrust level as disc angle is varied.

Figures 5.16, 5.17, and 5.18 present contour plots of the FOM against disc angle and normalised thrust, and extracted FOM values for a specific normalised thrust value.

For the 'Push Pull' case presented in Figure 5.16, the FOM shows little variation between disc angles of 180 and 90 degrees. As disc angle approaches the coaxial case the pusher disc maintains FOM whilst the puller disc sees a reduction of approximately one third.

As discussed previously in Section 3.1.3 there is an alternative method of calculating FOM for coaxial rotor systems. The previously discussed study presented by Brazinskas et al. (2016) considers a coaxial rotor system at similar thrust levels and rotor spacing as the coaxial case considered here. Brazinskas et al. also applies the Leishman and Syal methodology for coaxial FOM calculation. Results

Table 5.3: Individual and coaxial FOM values.

	Thrust (N)	FOM_{upper}	FOM_{lower}	$FOM_{coaxial}$
Experimental	8.3	0.65	0.33	0.51
Brazinskas et al. (2016)	8.0	0.61	0.37	0.49

from both experiments are presented in Table 5.3. Whilst the experiments have similar net thrusts the ratio of thrust between the upper and lower discs is different. As a result the experiments consider different disc loadings and therefore direct comparison is not possible.

Consider now the 'Push Push' and 'Pull Pull' cases presented in Figures 5.17 and 5.18. It can be seen that for both cases the FOM for either disc varies little for disc angles of between 180 and 90 degrees.

For the 'Push Push' case FOM values increase from 0.6 at a disc angle of 90 degrees to over unity at a disc angle of 0 degrees. The 'Push Push' case can considered to be similar to a single disc operating in 'ground effect'. Whilst experimental FOM values for a rotor in ground effect are not commonly published, Leishman (2006) does provide an "optimistic" value of 0.8.

The 'Pull Pull' case exhibits similar rise in FOM as disc angle approaches 0 degrees. Similarly to the 'Push Push' configuration, the 'Pull Pull' configuration can be considered as a rotor operating in 'ceiling effect'. A study by Heredia and Ollero (2017) provides experimental data on the change in thrust for a rotor operating in ceiling effect however they do not provide power data. Instead the study relates thrust to the 'throttle' position, or the PWM value passed to the ESC. The nature of ESC operation means it is not possible to relate these PWM values to power, and therefore the effect of the ceiling effect on rotor efficiency is not quantified.

For the 'Push Push' and 'Pull Pull' cases it is expected that there will be an

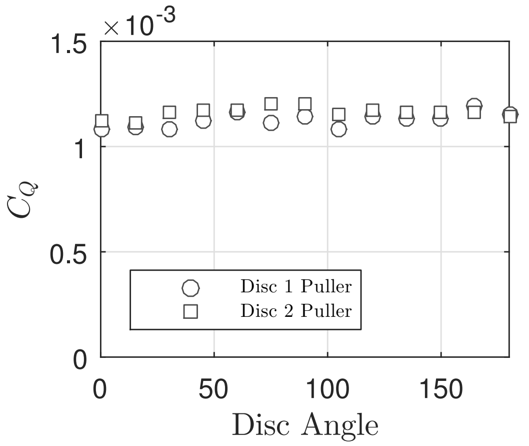

(a) ‘Pull’ ‘Pull’.

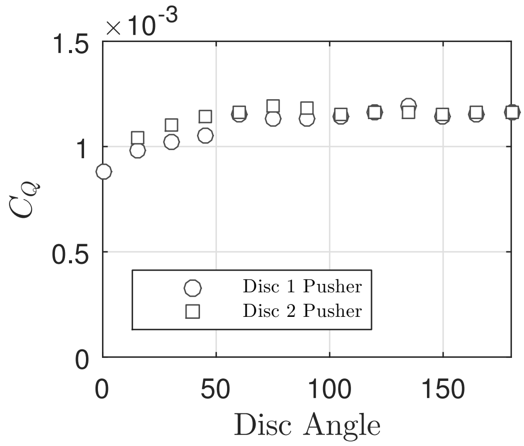

(b) ‘Push’ ‘Push’.

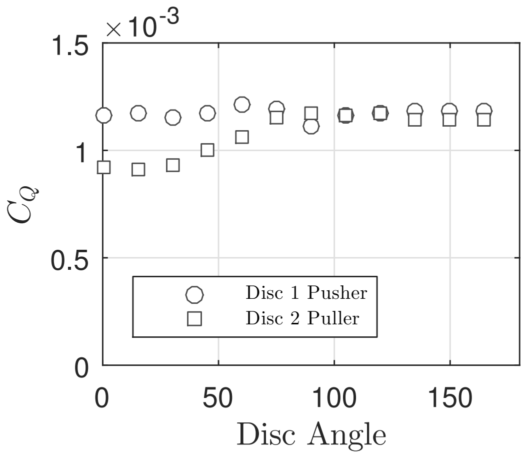

(c) ‘Push’ ‘Pull’.

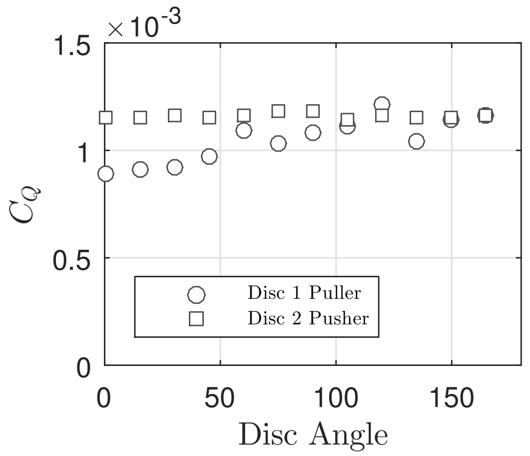

(d) ‘Pull’ ‘Push’.

Figure 5.15: Influence of disc angle on C_Q for different rotor configurations.

increase in FOM based on the similarity to ground and ceiling effect cases. However the values calculated in this experiment are higher than would be expected.

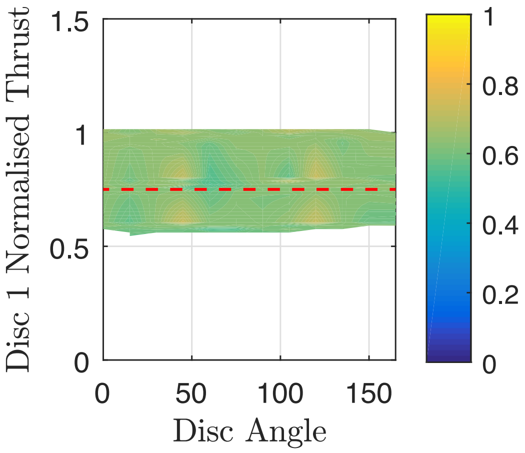

(a) Disc 1 FOM.

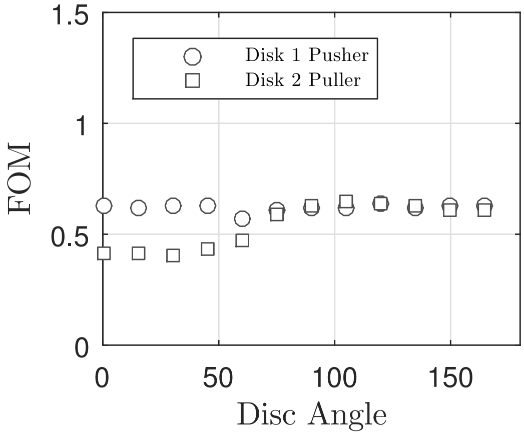

(b) FOM for normalised thrust = 0.75.

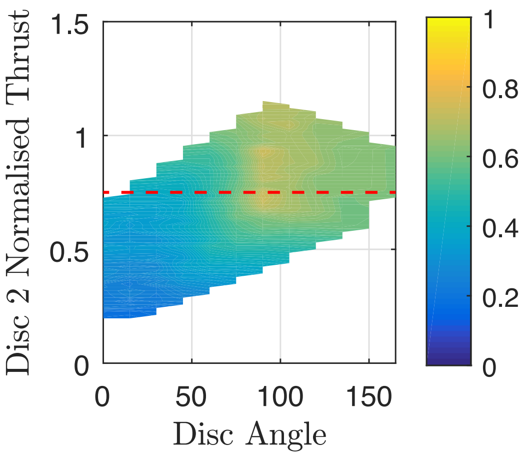

(c) Disc 2 FOM.

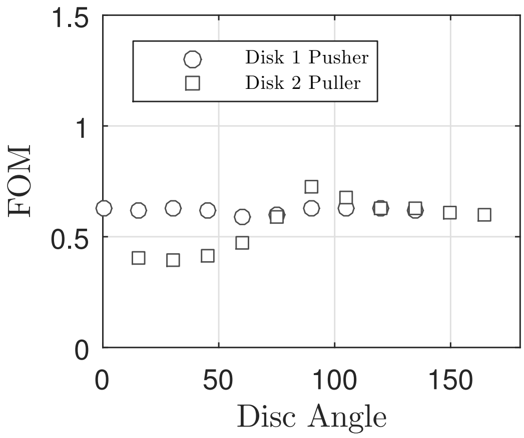

(d) FOM for normalised thrust = 0.75.

Figure 5.16: Influence of disc angle on FOM for 'Push Pull' configuration.

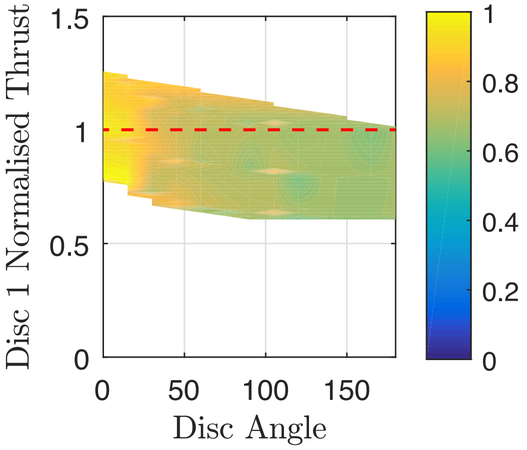

(a) Disc 1 FOM.

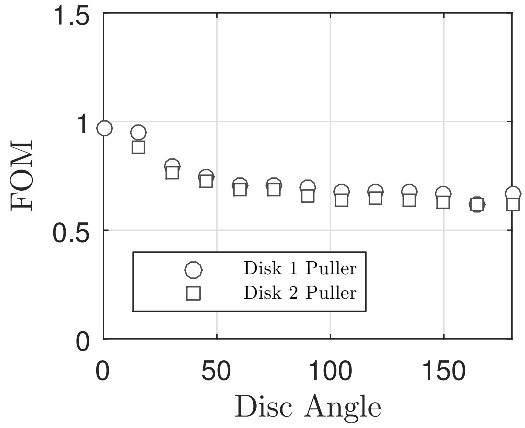

(b) FOM for normalised thrust = 1.0.

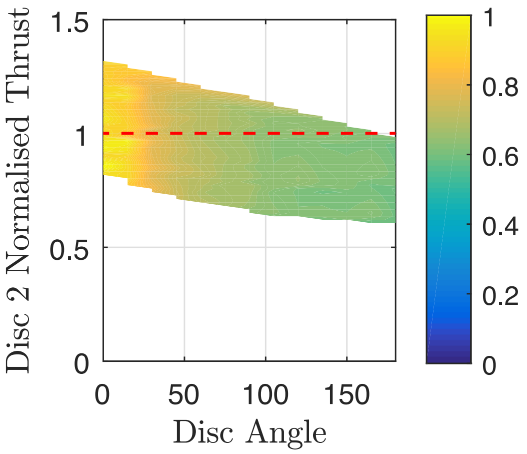

(c) Disc 2 FOM.

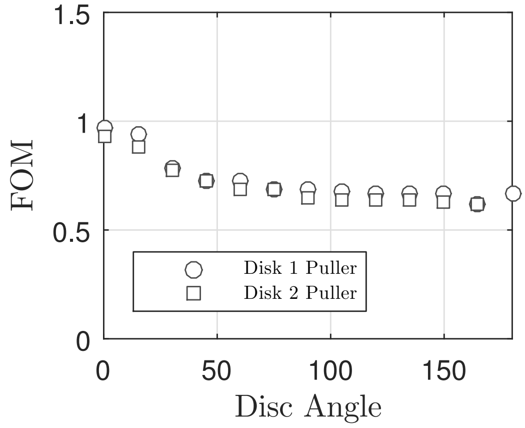

(d) FOM for normalised thrust = 1.0.

Figure 5.17: Influence of disc angle on FOM for ‘Pull Pull’ configuration.

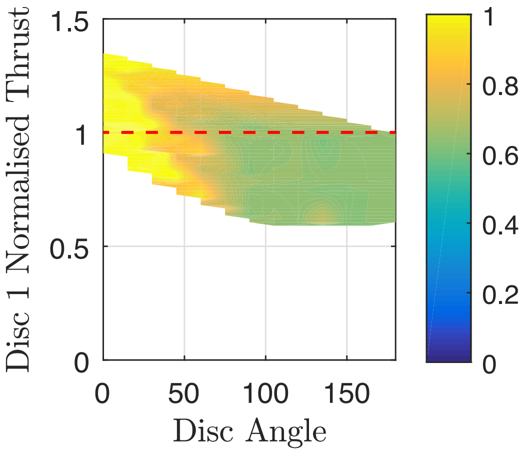

(a) Disc 1 FOM.

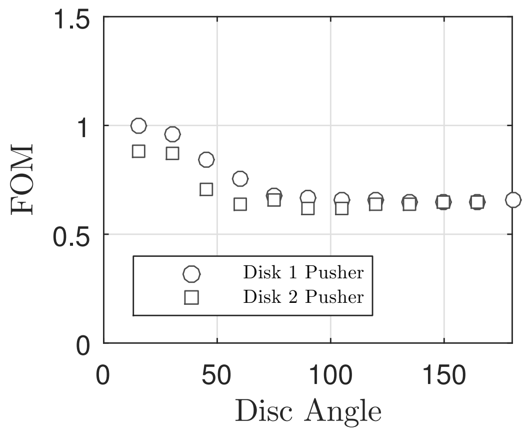

(b) FOM for normalised thrust = 1.0.

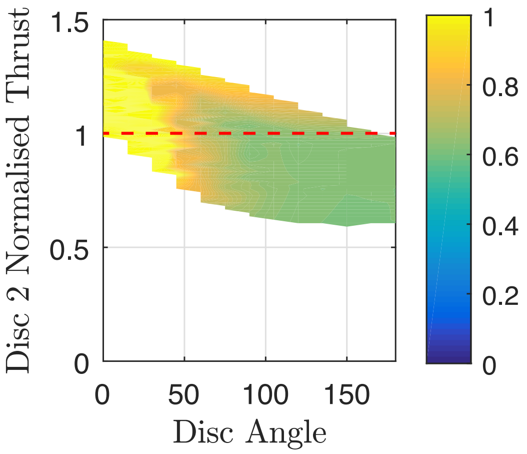

(c) Disc 2 FOM.

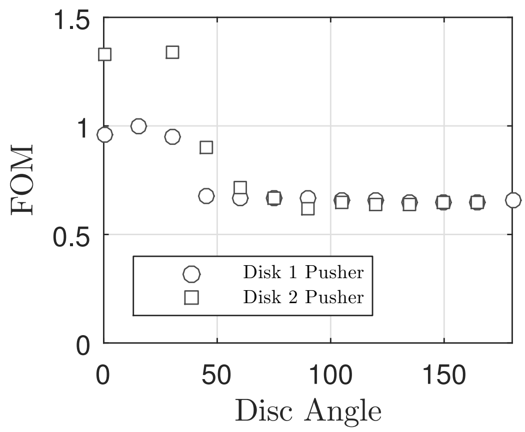

(d) FOM for normalised thrust = 1.0.

Figure 5.18: Influence of disc angle on FOM for ‘Push Push’ configuration.

5.3 Flow field data

5.3.1 Single rotor benchmark

The PIV experiment used to derive the streamlines in Section 5.1 was validated through comparison of PIV derived flow field data for a single rotor test case with theoretical models described by Leishman (2006). As discussed in Section 3.1.1 momentum theory can be used to relate the thrust generation, induced velocity, and exit velocity of a single rotor operating in isolation.

The PIV data is interrogated to determine average values for v_i of 5.4 m/s and w of 14.4 m/s, represented in Figure 5.19 as purple and black lines respectively. The corresponding thrust level measured for this rotor configuration is approximately 7 N. From this thrust value v_i and w can be calculated as shown in Equations 5.1 and 5.2.

$$\begin{aligned} v_i &= \sqrt{\frac{T}{2\rho A}} \\ &= 7.1\ m.s^{-1} \end{aligned} \tag{5.1}$$

$$\begin{aligned} w &= 2v_{inflow} \\ &= 14.2\ m.s^{-1} \end{aligned} \tag{5.2}$$

Strong agreement is seen between the experimental and theoretical values for w. The disparity between values for v_i is likely a result of the shading of the region of interest by the rotor and inadequate capture of the three-dimensionality of the flow in the region of the disc.

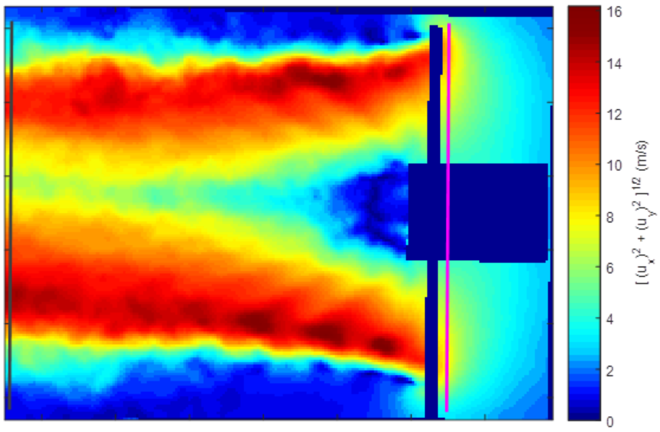

Figure 5.19: Single rotor test case for PIV validation.

5.4 Summary

- The experimental data set shows good agreement with the theoretical estimates derived using BET, with a smaller deviation between results than seen in prior investigations.
- The use of a custom rotor system removes some of the uncertainty inherent in modelling a COTS rotor and allowed for a stiffer blade to be used, reducing aeroelastic deformation.
- For 'Push Push' and 'Pull Pull' configurations:
  - Varying disc angle from 180 degrees to 90 degrees has no effect on peak thrust.
  - As disc angle is reduced from 90 degrees to 0 degrees a significant increase in thrust is seen.
  - For the 0 degree case thrust is increased by $\sim 23\%$, for the 'Pull Pull' configuration, and $\sim 40\%$ for the 'Push Push' configuration.
- For 'Push Pull' configurations:

  - The pulling disc exhibits a $\sim 5\%$ increase in peak thrust between disc angles of 120 degrees and 90 degrees.
  - For disc angles between 0 degrees and 30 degrees, peak thrust is reduced by $\sim 35\%$.
  - This thrust plateau coincides with the pulling disc operating fully in the wake of the pushing disc.
  - A moment is generated about the rotor hub of the pulling rotor between disc angles of 30 and 75 degrees and acts to rotate the pulling rotor away from the pushing rotor.
  - The magnitude of this moment is significant and comparable to the torque generated by the motor.

- For disc angles between 90 degrees and 180 degrees minimal changes in FOM are seen for all rotor configurations.
- For disc angles lower than 60 degrees the FOMs for 'Push Pull' rotor configurations become similar to that of a coaxial rotor system. PIV data shows that the puller disc operates fully inside the wake of the pusher disc in these cases.
- The use of a custom rotor means that the rotor systems considered in this investigation do not exhibit the same aeroelastic behaviour as COTS rotors.

Chapter 6

Implications for vehicle design

6.1 Case studies

6.1.1 TumbleWeed

The ‘TumbleWeed’ hexrotor (Crowther et al., 2008) shown in Figure 6.1 consists of six variable pitch rotors orientated at 52.7 degrees to the horizontal. The design places adjacent rotor discs at a relative angle of 90 degrees, with ‘Pull Pull’, ‘Pull Push’, and ‘Push Push’ rotor configurations possible due to the variable pitch units.

In Figure 6.2 TumbleWeed is shown in a hovering orientation where only

Figure 6.1: TumbleWeed non-planar multirotor concept (Llopis Pascual, 2011).

the two horizontal rotors are providing lift thrust. By considering the results of presented in chapter 5, the impact of using the two vertically aligned to translate the vehicle towards the left of the figure can be assessed. The two remaining rotors are assumed to be generating zero thrust. This scenario allows all interaction cases between rotors to be analysed using data gathered in the preceding experimental investigation.

Figure 6.3 displays velocity vectors for the upper left quadrant of the flow field where two rotors are operating in a 'pull pull' configuration. As Figure 6.6a shows, there is minimal impact on thrust generation for either rotor. Figure 6.7a and Figure 6.7b show that there is negligible change in C_{Q_x} and C_{Q_y} for this configuration, compared to each rotor operating in isolation.

Figure 6.4 considers the upper right quadrant of the flow field where the outflow from the upper rotor is passing across the inflow of the lower rotor. In this case there is a small but measurable increase in thrust generation for the lower rotor but negligible effect on the upper rotor, as shown in Figure 6.6b. In order to maintain a constant altitude and prevent any undesirable attitude changes the TumbleWeed flight controller would need to reduce the thrust demand, the pitch angle, for the lower rotor.

A change in C_{Q_y} is measured for both the pushing and pulling rotor, acting to rotate the discs away from each other, no significant variation C_{Q_x} is seen. The level of variation in C_{Q_y} would have no impact on aircraft performance.

Finally we consider the the lower right quadrant in Figure 6.5, where two rotors are operating in a 'push push' configuration. As with the 'pull pull' case negligible changes in thrust and C_{Q_x} are measured. A variation in C_{Q_y} is measured, similar to that seen in the 'push pull' case, acting to rotate the rotor discs apart. As in the 'push pull' case this variation in C_{Q_y} would not impact performance.

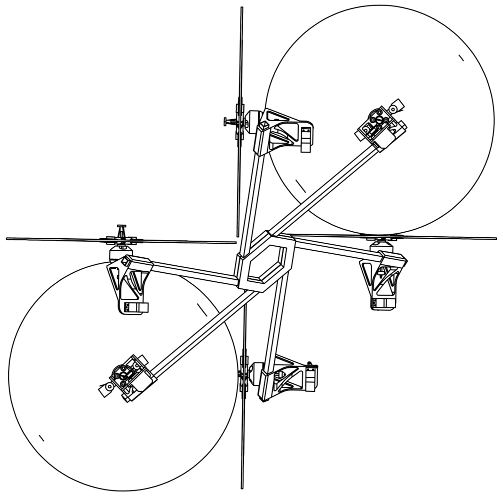

Figure 6.2: Tumbleweed in a two rotor hover orientation.

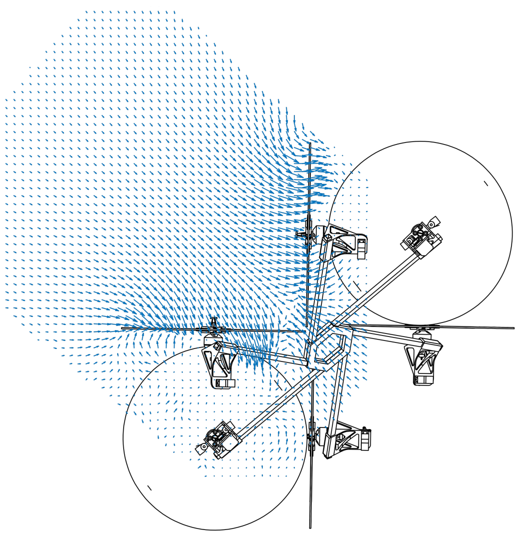

Figure 6.3: Vector field for 'Pull Pull' interaction.

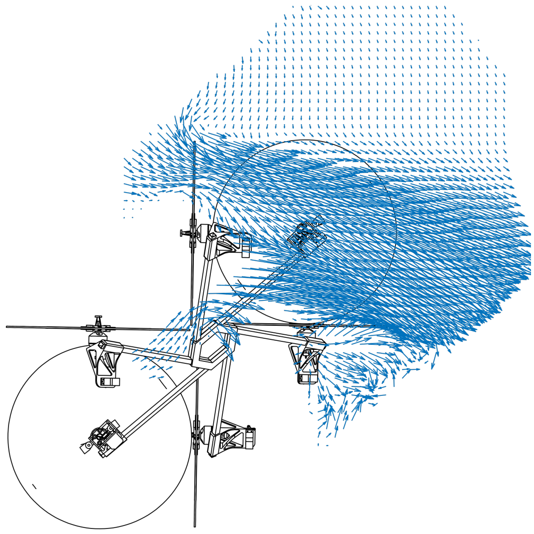

Figure 6.4: Vector field for 'Push Pull' interaction.

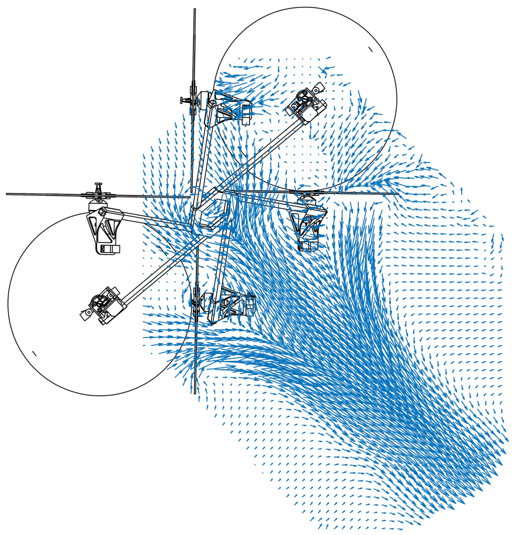

Figure 6.5: Vector field for 'Push Push' interaction.

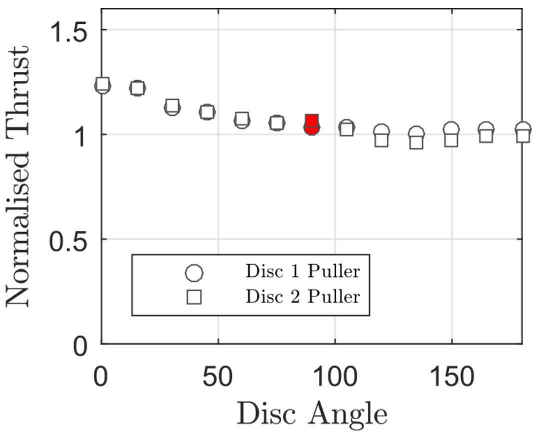

(a) 'Pull Pull' configuration.

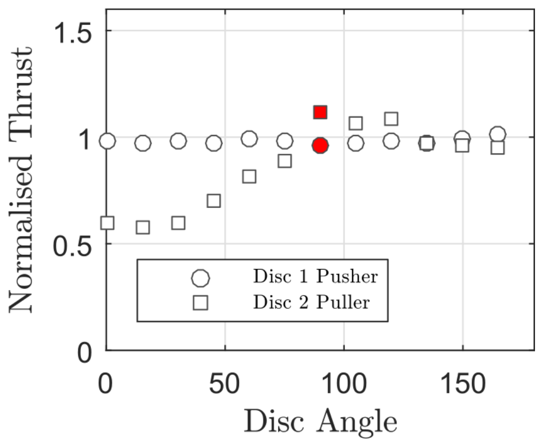

(b) 'Push Pull' configuration.

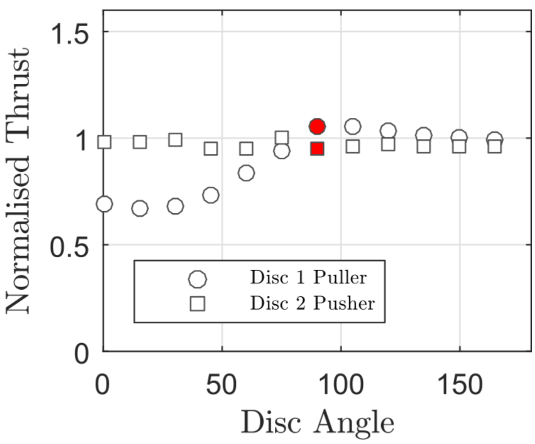

(c) 'Pull Push' configuration.

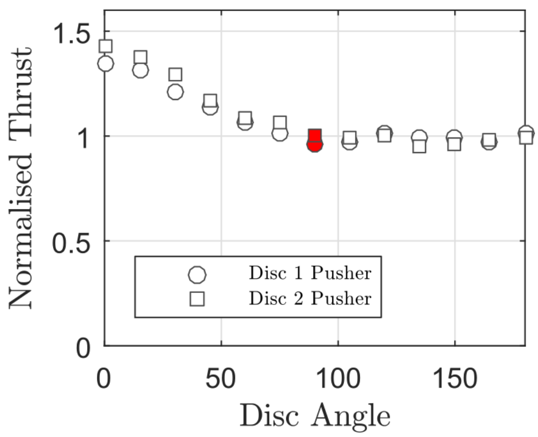

(d) 'Push Push' configuration.

Figure 6.6: Variation in normalised thrust with disc angle.

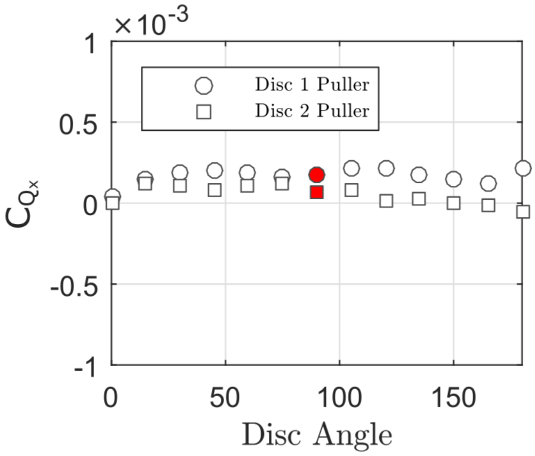

(a) 'Pull Pull' configuration.

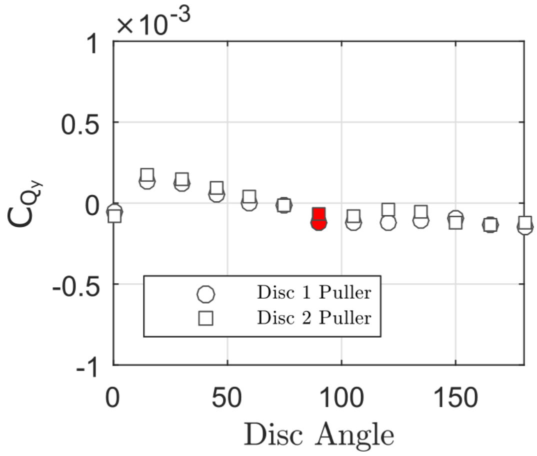

(b) 'Pull Pull' configuration.

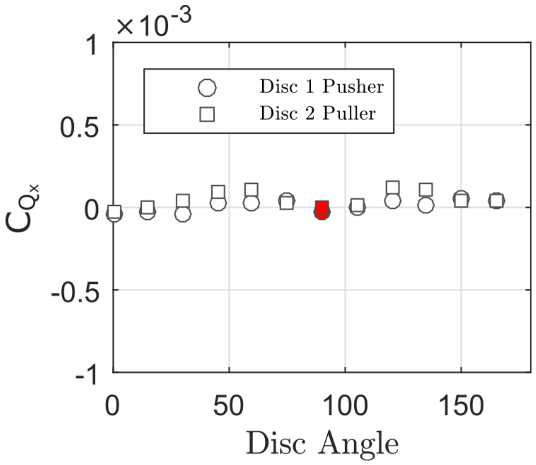

(c) 'Push Pull' configuration.

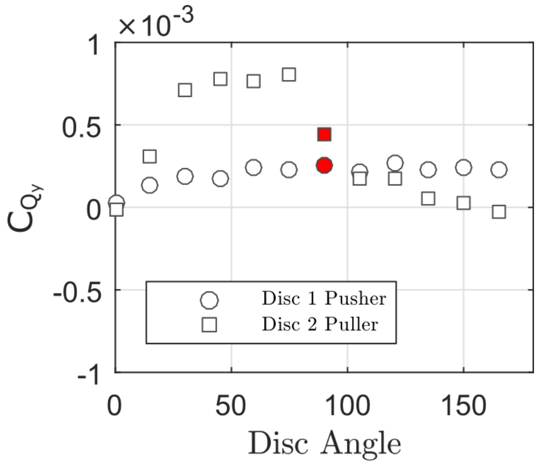

(d) 'Push Pull' configuration.

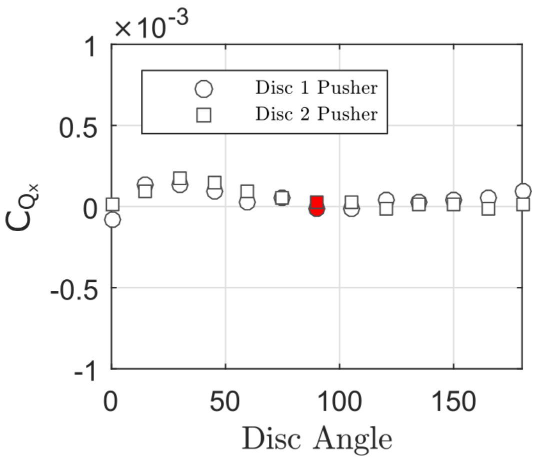

(e) 'Push Push' configuration.

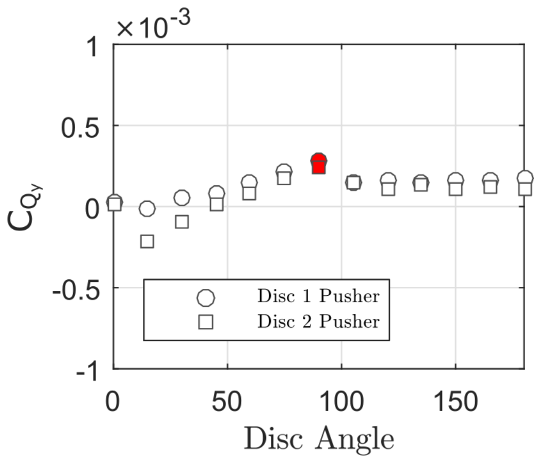

(f) 'Push Push' configuration.

Figure 6.7: Variation in C_{Q_x} and C_{Q_y} with disc angle.

6.1.2 Marble VTOL aircraft

The Marble MRB3, shown in Figure 6.8, is a VTOL aircraft designed to carry a 5 kg payload at a cruise speed of 158 kph and a range of 120 km. The unusual configuration is known as a quadplane which, as the name suggests, combines characteristics of fixed wing aircraft and quadrotors.

For the majority of quadplanes the configuration is chosen to reduce some of the difficulties associated with the take-off and landing phases of UAV flight. An additional advantage to separating cruise and take-off/landing is that the propulsion and lift systems can be highly optimised for the specific regime they operate in. For example the wing can be sized for cruise speed with no requirement for a high lift system, such as flaps, and the flight propulsion system can be selected for efficient operation at cruise speed. As the vertical lift system needs only to operate briefly during take-off and landing, efficiency can become secondary to reducing the system footprint and thereby limiting the drag penalty associated with the vertical lift system during cruise.

The heavy optimisation of MRB3 results in a platform with a very confined flight envelope. For example the stall speed is 144 kph, and the vertical lift system can only sustain the required thrust level for approximately 10 seconds before overheating. In addition, the high power requirements of the vertical lift system require a high current draw from the battery power source which will cause a drop in voltage due to the internal resistance of the battery. This has a knock-on effect of lowering the maximum achievable RPM of any motors sharing the same power source. These operational constraints mean that the transition from hover to forward flight must be carefully handled, and it is therefore important that the designers understand all aspects of the system design that will effect thrust generation.

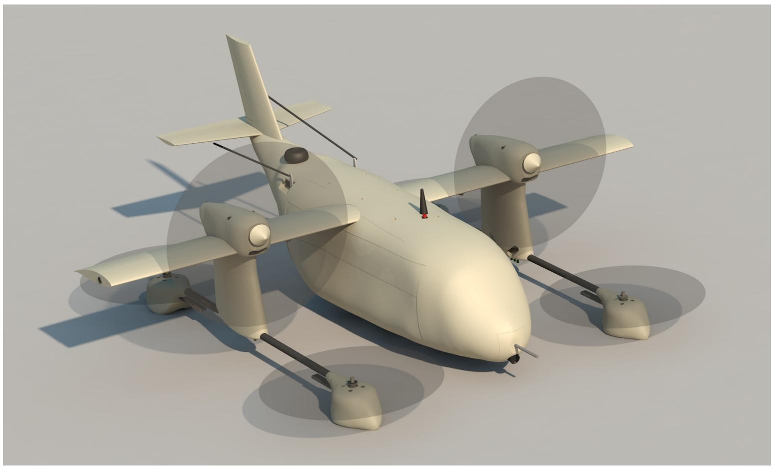

Figure 6.8: MRB3 VTOL aircraft.

A preliminary analysis performed on MRB2, a reduced weight testing version of MRB3, uses the data generated during the experimental investigation to assess the significance of the interaction between the vertical lift and forward flight rotors of the aircraft. It should be noted that the comparison is limited as the experiments did not consider any external flow field, however the period of transition of most interest is at very low airspeed so this is an acceptable limitation.

Figure 6.9 shows the anticipated flow field around the lift rotors during hovering flight. Figure 6.10 shows the changing flow field during the transition phase of flight as both the lift rotors and forward flight rotors are operating at full power. Finally, Figure 6.11 shows the flow field when the aircraft is in forward flight, with the flight motor operating in isolation.

The variation in lift thrust as flight thrust level changes is shown in Figure 6.12a. Figure 6.12b shows the variation in flight thrust as lift thrust level is changed. Whilst a slight trend can be discerned in both figures, the variation is not significant.

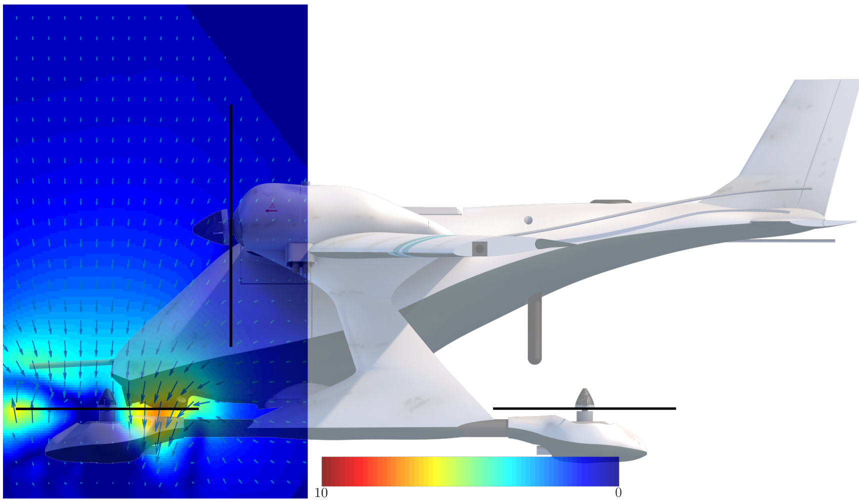

Figure 6.9: Vector flow field and velocity magnitude contour for MRB2 during hover.

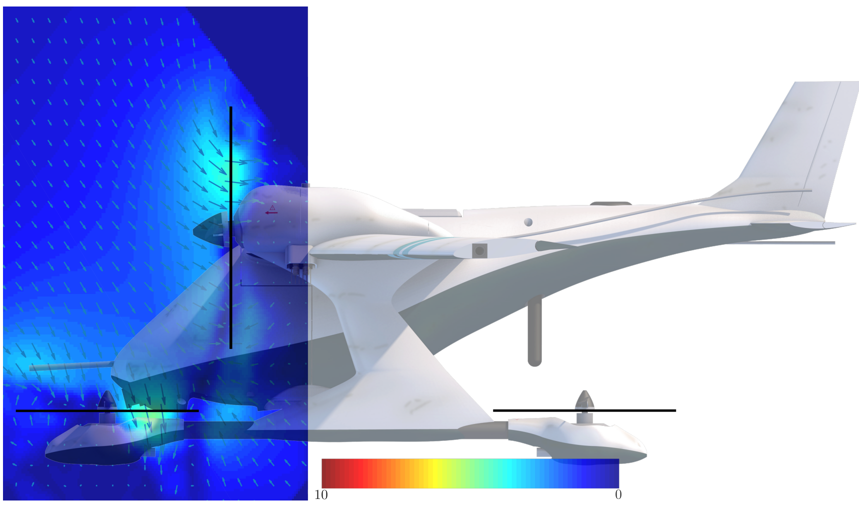

Figure 6.10: Vector flow field and velocity magnitude contour for MRB2 during transition.

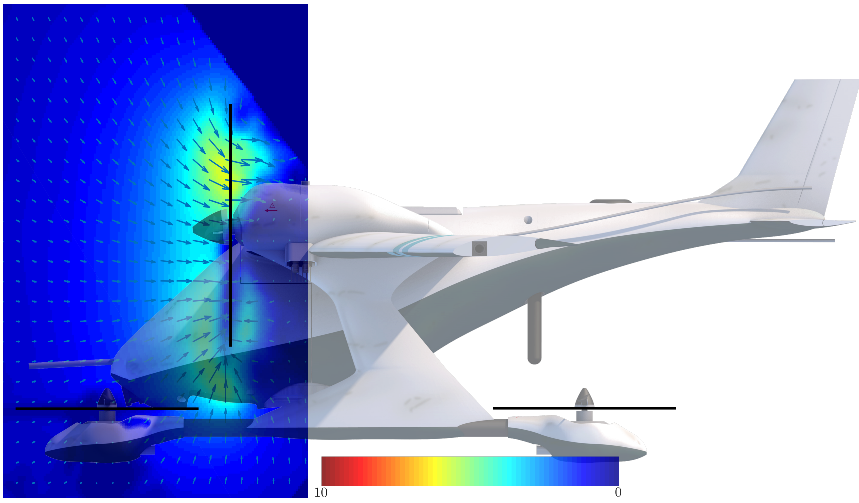

Figure 6.11: Vector flow field and velocity magnitude contour for MRB2 during flight.

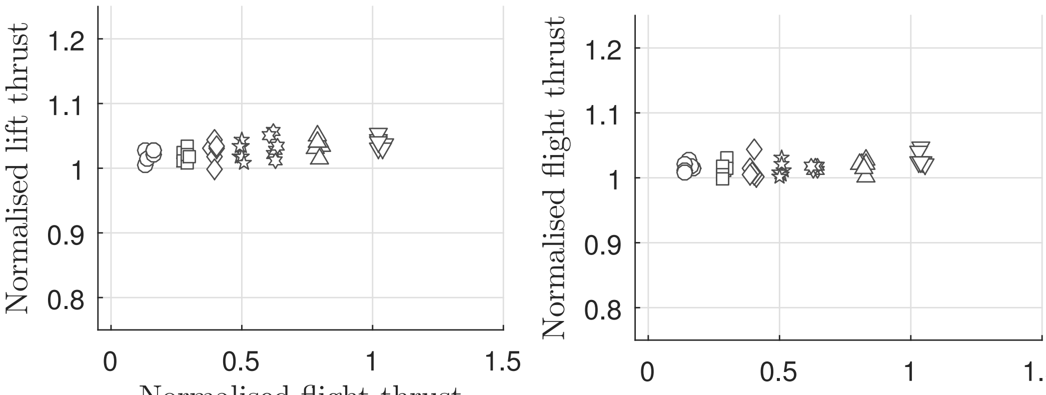

(a) Lift thrust as flight thrust varies. **(b)** Flight thrust as lift thrust varies.

Figure 6.12: Variation in normalised thrust during transitions.

6.1.3 Summary

As discussed Chapter 1 non-planar multirotor systems enable some interesting and novel vehicle designs. A fully non-planar configuration such as TumbleWeed results in a holonomic vehicle that can translate and rotate through all axes, a useful trait for a utility vehicle designed to place a sensor or tool against some object. There is also value in simpler non-planar rotor systems, with the quadplane concept benefiting from an ability to take-off and land vertically whilst retaining the cruise characteristics and endurance of a fixed wing aircraft.

Whilst it is entirely feasible to design a multirotor aircraft whilst ignoring rotor-rotor interactions, as discussed in Section 2.1.3, it becomes an important consideration when a design results in a significantly low thrust to weight ratio. In such cases any loss in thrust generation can severely limit performance or even prevent flight.

In the case of TumbleWeed, the design requires each pair of rotors to have sufficient thrust to lift the entire aircraft. However once built, slight gains in weight and losses in thrust eroded the small thrust margin of the vehicle and left it with inadequate performance. It is not unusual to see such a problem result in a design 'stall' until a sufficient change in battery energy density allows for a slight reduction in vehicle weight. By applying the results of the experimental investigation to this vehicle, as discussed in this chapter, the sensitivity of the design to rotor-rotor interactions can be analysed. It was found that for the TumbleWeed configuration, the variations in thrust seen due to interactions are relatively low, under 5%, and could be adequately handled by a flight controller in a responsive manner. However, the potential reductions in thrust have more significance when considering the relationship between total thrust and thrust required for hover presented in Figure 6.13, where peak static thrust is only 6%

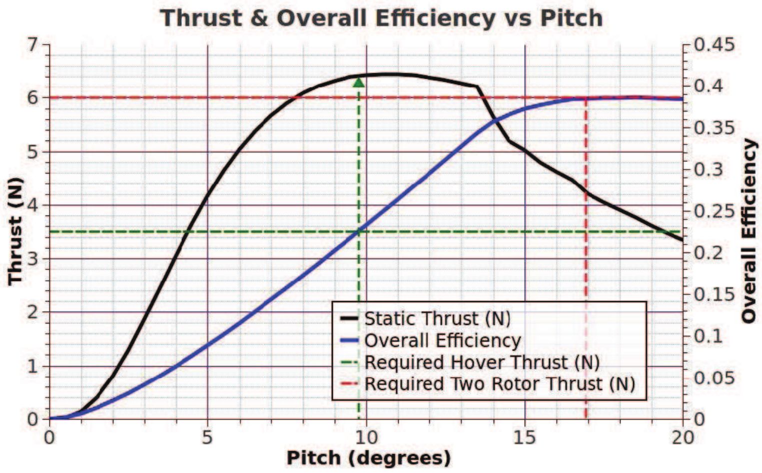

Figure 6.13: Hover performance of TumbleWeed design (Langkamp et al., 2011).

greater than the the required two rotor hover thrust.

The analysis indicates that, whilst there is enough thrust margin to account for the loss in thrust due to interaction, the aircraft performance will be significantly limited. In its current configuration the vehicle would be capable of a two rotor hover only if it was free from all outside disturbances. It is therefore recommended that the thrust to weight ratio of the vehicle is increased to enable a larger flight envelope.

For the Marble quadplane concepts the vertical lift system of the aircraft is operated at the limit of its power handling ability, with little excess thrust available. The first iterations of the aircraft hovered and cruised adequately, but were unable to transition between hover and cruise. By applying the performance data gathered in this investigation to the quadplane design it was possible to assess the impact on thrust of having two perpendicular rotors operating so closely.

The results of the analysis indicate that the Marble design is not sensitive to aerodynamic interaction between the lift and flight propulsion systems. It follows that the drop in maximum thrust seen during transition are likely due to the voltage sag of the battery under high load, reducing the maximum achievable

RPM of the lift and flight rotors. It is recommended that Marble consider ways to alleviate the voltage sag, or alternatively re-specify the flight propulsion system so that the required levels of thrust can be achieved at a lower supply voltage.

6.2 Recommendations for non-planar designs

6.2.1 Disc angles of 180 to 90 degrees

For disc angles between 180 and 90 degrees, minimal losses in thrust or efficiency are seen. This means that non-planar designs such as the *Dextrous Hexrotor* Jiang and Voyles (2013) will not experience any significant performance changes due to the rotor interactions. As the disc angle approaches 90 degrees the thrust losses become slightly more significant. For designs with marginal thrust to weight ratios, such as TumbleWeed, the loss in thrust from rotor interaction may critically limit the aircraft performance. It is therefore recommended that for vehicles with a disc angle of 90 degrees, a 10% thrust margin for hover is used during the design phase to ensure that there is sufficient performance available. This margin may need to be increased if the vehicle is to be subject to external disturbances, such as wind.

For quadplane type configurations the losses in thrust from the rotor interactions can be mitigated through slower transitions from hover to forward flight, allowing wing lift to make up for the lift reduction in the vertical lift motor.

6.2.2 Disc angles of 90 to 0 degrees

As disc angle is reduced past 90 degrees, significant moments are seen around the rotor hub. Such moments can cause undesirable deflections of the rotor blades leading to vibration and asymmetric lift around the rotor disc. The actual significance of these moments depends upon the design of the rotor disc, including the strength of the blades and how they are mounted to the rotor hub. Further, any vibrations will be transmitted through the motor into the structure of the aircraft and could potentially affect the flight control system. It is therefore recommended that for designs with disc angles that fall within this range, a particular emphasis is placed on selecting a rotor system that will minimise an blade deflection. Alternatively the results of significant deflection can by mitigated by taking appropriate measures to strengthen the aircraft structure and dampen vibration for the flight control electronics.

At small disc angles the outflow of two pushing rotors is combined, and both rotors benefit from a significant increase in thrust, reaching a peak of around 40% when the rotors are coaxial. This is a similar condition to a rotor operating in ground effect. Similarly two pulling rotors sharing an inflow benefit from a 'ceiling effect'.

It is not immediately clear what role or function would be of a vehicle that exploited the advantages of these very small disc angles and the ground and ceiling effects, as the net system thrust tends towards zero.

The closest existent vehicle designs are in the hobbyist field, where there are a small number of bespoke 'Y-tail' and 'A-tail' quadrotor configurations that utilise disc angles of less than 90 degrees to provide exceptionally high yaw response, however the application is limited to fun flying and racing where high speed yaw is appreciated and the reduction in hover efficiency is not a significant factor.

Low disc angles are recommended for non-planar rotor vehicles where large and fast changes in orientation are required. Overall vehicle efficiency should not be a primary consideration as there will be a significant weight penalty for such a configuration.

Chapter 7

Conclusions

7.1 Review of contributions

The work detailed in this thesis presents several key contributions.

1. An analysis of the effects of non-planar rotor interactions on thrust, torque, and power requirements of a rotor system.

2. A unique experimental dataset providing time-averaged performance data for small scale fixed pitch rotors operating in co-planar and non-planar states was presented in Chapter 5. Additional instantaneous data is available for use in further studies.

3. Instantaneous and time averaged two dimensional flow field velocity data derived from PIV. This dataset encompasses isolated and interaction cases and is suitable for validation of CFD studies.

4. An extensible adjustable rotor interaction rig and experimental method is developed as described in Section 4.3.1. The rig is designed to use COTS components where possible, and allows for additional rotor systems to be added as required.

5. The results of the investigation are applied to two existent non-planar multirotor vehicle designs in Chapter 6 and recommendations are made for consideration of the designers of non-planar multirotor vehicles.

7.2 Performance of non-planar rotors

- Rotor performance changes minimally for disc angles between 90 degrees and 180 degrees.
- Significant thrust increases are seen for 'Push Push' and 'Pull Pull' rotor configurations at low disc angles of less than 90 degrees.
- The symmetry of 'Push Push' and 'Pull Pull' configurations makes them similar to a rotor operating in ground or ceiling effect.
- In 'Push Pull'/'Pull Push' configurations with disc angles lower than 30 degrees, the pulling rotor exhibits similar performance to that of the lower rotor in a coaxial rotor system. This corresponds with the pulling rotor operating entirely in the wake of the pushing rotor.
- In all cases pitching moments are generated as the flow fields of the rotors interact.
- In 'Push Pull'/'Pull Push' configurations considerable pitching moments are measured on the pulling rotor for disc angles between 30 and 75 degrees. This corresponds with the pulling rotor operating partially in the wake of the pushing rotor.

7.3 Design of non-planar multirotor vehicles

- By keeping the angle between adjacent discs greater than 90 degrees, rotor interaction effects can be kept to a minimum.
- Analysis of a number of existing non-planar configurations show that many of these designs have sufficiently high disc angles and so avoid significant interaction effects.
- Designs with more acute disc angles, like 'Tumbleweed', see significant changes in rotor performance due to rotor-rotor interactions.
- Variable pitch props add an extra dimension, with the potential for rapid and significant changes in rotor performance.

7.4 Recommendations for future research

- Investigate dynamic interaction effects using the instantaneous data acquired in this investigation.
- Extend the PIV investigation through the use of a stereoscopic PIV system. This will allow the derivation of the third velocity component of the flow field, improving understanding of the highly three dimensional flow around interacting rotor systems.
- Implementation of a CFD study utilising the data presented in this thesis for validation.
- Expand the experimental and CFD investigation to include rotor-body interactions.

- Investigate the effects of the measured force moments and flow asymmetry on conventional COTS rotor blades.
- Development of a non-planar multirotor propulsion system specification based on the results of this thesis.

Bibliography

Barakos, G. N. and Jimenez-Garcia, A. CFD analysis of hover performance of rotors at full- and model-scale conditions. *The Aeronautical Journal*, 120(1231):1386–1424, 2016. ISSN 0001-9240. doi: 10.1017/aer.2016.58. URL `https://www.cambridge.org/core/product/identifier/S0001924016000580/type/journal_article`.

Beharie, M. Mechatronic Design of a Quadrotor Test Rig for System Identification. Technical report, University of the Witwatersrand, Johannesburg, 2013.

Borenstein, J. The HoverBot–An electrically powered flying robot. *Ann Arbor*, pages 4–17, 1992. URL `ftp://ftp.eecs.umich.edu/people/johannb/paper99.pdf`.

Bouabdallah, S. *Design and control of quadrotors with application to autonomous flying*. PhD thesis, École Polytechnique Fédérale De Lausanne, 2007. URL `http://www.es.ele.tue.nl/education/5HC99/wiki/images/3/39/EPFL_TH3727.pdfhttp://biblion.epfl.ch/EPFL/theses/2007/3727/EPFL_TH3727.pdf`.

Bouabdallah, S. and Siegwart, R. Backstepping and sliding-mode techniques applied to an indoor micro Quadrotor. In *Proceedings - IEEE International Conference on Robotics and Automation*, pages 2247–2252, 2005. ISBN 078038914X. doi: 10.1109/ROBOT.2005.1570447.

Bouabdallah, S. and Siegwart, R. Full control of a quadrotor. In *2007 IEEE/RSJ International Conference on Intelligent Robots and Systems*, pages 153–158, San Diego, CA, USA, 10 2007. IEEE. ISBN 978-1-4244-0911-2. doi: 10.1109/IROS.2007.4399042. URL `http://ieeexplore.ieee.org/document/4399042/`.

Bouabdallah, S., Murrieri, P., and Siegwart, R. Design and control of an indoor micro quadrotor. In *IEEE International Conference on Robotics and Automation, 2004. Proceedings. ICRA '04. 2004*, pages 4393–4398, 2004a. ISBN 0-7803-8232-3. doi: 10.1109/ROBOT.2004.1302409.

Bouabdallah, S., Noth, A., and Siegwart, R. PID vs LQ Control Techniques Applied to an Indoor Micro Quadrotor. In *IEEE/RSJ International Conference on Intelligent Robots and Systems*, volume 3, pages 2451–2456, 2004b. ISBN 0-7803-8463-6. doi: 10.1109/IROS.2004.1389776.

Bouabdallah, S., Murrieri, P., and Siegwart, R. Towards Autonomous Indoor Micro VTOL. *Autonomous Robots*, 18(2):171–183, 3 2005. ISSN 0929-5593. doi: 10.1007/s10514-005-0724-z. URL `http://link.springer.com/10.1007/s10514-005-0724-z`.

Bouabdallah, S., Siegwart, R., and Caprari, G. Design and control of an Indoor Coax Helicopter. In *IEEE International Conference on Intelligent Robots and Systems*, pages 2930–2935, 2006. ISBN 142440259X. doi: 10.1109/IROS.2006.282146.

Brazinskas, M., Prior, S., and Scanlan, J. An Empirical Study of Overlapping Rotor Interference for a Small Unmanned Aircraft Propulsion System. *Aerospace*, 3(4):32, 10 2016. ISSN 2226-4310. doi: 10.3390/aerospace3040032. URL `http://www.mdpi.com/2226-4310/3/4/32`.

Brescianini, D. and D'Andrea, R. Design, modeling and control of an omnidirectional aerial vehicle. *Proc. IEEE Int'l Conference on Robotics and Automation*, pages 3261–3266, 2016. ISSN 10504729. doi: 10.1109/ICRA.2016.7487497.

Bristeau, P.-j., Martin, P., Salaün, E., and Petit, N. The role of propeller aerodynamics in the model of a quadrotor UAV. *European Control Conference Proceedings*, pages 683–688, 2009. URL `http://cas.ensmp.fr/~petit/papers/ecc09/PJB.pdf`.

Crowther, B., Lanzon, A., Maya-Gonzalez, M., and Langkamp, D. Kinematic Analysis and Control Design for a Nonplanar Multirotor Vehicle. *Journal of Guidance, Control, and Dynamics*, 34(4):1157–1171, 7 2011. ISSN 0731-5090. doi: 10.2514/1.51186. URL `http://arc.aiaa.org/doi/abs/10.2514/1.51186`.

Crowther, W. J., Pilmoor, M., Lanzon, A., and Geoghegan, P. GB2462452A - A rotary wing vehicle, 2008.

Cutler, M. J. *Design and Control of an Autonomous Variable-Pitch Quadrotor Helicopter*. PhD thesis, Massachusettes Institute of Technology, 2012.

Dehaeze, F., Allen, C. B., and Barakos, G. N. The Collaborative Development of New CFD Methods Adapted for Tilt Rotor Aircraft in the HiPerTilt Project. *35th AIAA Applied Aerodynamics Conference*, 2017. doi: 10.2514/6.2017-3919. URL `https://arc.aiaa.org/doi/10.2514/6.2017-3919`.

Dingeldein, R. C. Wind-tunnel Studies of the Performance of Multirotor Configurations. *National Advisory Committee for Aeronautics, NACA-TN-3236*, page 12, 1954. URL `https://ntrs.nasa.gov/search.jsp?R=19930083899`.

Foster, J. V. and Hartman, D. High-Fidelity Multi-Rotor Unmanned Aircraft System (UAS) Simulation Development for Trajectory Prediction Under Off-Nominal Flight Dynamics. *17th AIAA Aviation Technology, Integration, and Operations Conference*, pages 1–19, 2017. doi: 10.2514/6.2017-3271. URL `https://arc.aiaa.org/doi/10.2514/6.2017-3271`.

Halliday, A. S. and Cox, D. K. Wind Tunnel Experiments on a Model of a Tandem Rotor Helicopter. Technical report, Ministry of Aviation, 1961.

Harrington, A. M. *OPTIMAL PROPULSION SYSTEM DESIGN FOR A MICRO QUAD ROTOR*. PhD thesis, University of Maryland, 2011.

Heredia, G. and Ollero, A. Multirotor UAS for bridge inspection by contact using the ceiling effect. In *2017 International Conference on Unmanned Aircraft Systems*, pages 767–774, Miami, FL, 2017. ISBN 9781509044948.

Hoffmann, G., Rajnarayan, D., Waslander, S., Dostal, D., Jang, J., and Tomlin, C. The Stanford testbed of autonomous rotorcraft for multi agent control (STARMAC). *The 23rd Digital Avionics Systems Conference (IEEE Cat. No.04CH37576)*, 2(23):1–10, 2004. doi: 10.1109/DASC.2004.1390847.

Hoffmann, G., Huang, H., Waslander, S., and Tomlin, C. Quadrotor Helicopter Flight Dynamics and Control: Theory and Experiment. In *AIAA Guidance, Navigation and Control Conference and Exhibit*, pages 1–20, Reston, Virigina, 8 2007. American Institute of Aeronautics and Astronautics. ISBN 978-1-62410-015-4. doi: 10.2514/6.2007-6461. URL `http://arc.aiaa.org/doi/10.2514/6.2007-6461`.

Hoffmann, G. M. *Autonomy for sensor-rich vehicles: Interaction between sensing and control actions*. PhD thesis, Stanford Unviersity, 2008.

Hrishikeshavan, V., Black, J., and Chopra, I. Development of a Quad Shrouded Rotor Micro Air Vehicle and Performance Evaluation in Edgewise Flow. *Journal of Aircraft*, 49, 2012. ISSN 15522938. URL `http://terpconnect.umd.edu/~vikramh/quadshroud/hoverandedgewiseflowperformance.pdf`.

Huang, H., Hoffmann, G. M., Waslander, S. L., and Tomlin, C. J. Aerodynamics and control of autonomous quadrotor helicopters in aggressive maneuvering. *Proceedings - IEEE International Conference on Robotics and Automation*, pages 3277–3282, 2009. ISSN 10504729. doi: 10.1109/ROBOT.2009.5152561.

Jcgm, J. C. F. G. I. M. Evaluation of measurement data — Guide to the expression of uncertainty in measurement. *International Organization for Standardization Geneva ISBN*, 50(September):134, 2008. ISSN 00099147. doi: 10.1373/clinchem.2003.030528. URL `http://www.bipm.org/en/publications/guides/gum.html`.

Jiang, G. *Dexterous Hexrotor UAV Platform*. PhD thesis, University of Denver, 2013.

Jiang, G. and Voyles, R. Hexrotor UAV platform enabling dextrous interaction with structures-flight test. In *2013 IEEE International Symposium on Safety, Security, and Rescue Robotics (SSRR)*, pages 1–6. IEEE, 10 2013. ISBN 978-1-4799-0880-6. doi: 10.1109/SSRR.2013.6719377. URL `http://ieeexplore.ieee.org/lpdocs/epic03/wrapper.htm?arnumber=6719377`.

Jimenez-Garcia, A. and Barakos, G. N. Numerical Simulations of Rotors Using High Fidelity Methods. *35th AIAA Applied Aerodynamics Conference*, 9781624105(March):5–9, 2017. doi: 10.2514/6.2017-3053. URL https://arc.aiaa.org/doi/10.2514/6.2017-3053.

Jimenez-Garcia, A., Barakos, G. N., and Gates, S. Tiltrotor CFD part I: validation. *The Aeronautical Journal*, 121, 2016. ISSN 0001-9240. doi: 10.1017/aer.2016.1. URL https://www.cambridge.org/core/product/identifier/S0001924016000014/type/journal_article.

Kroo, I., Prinz, F., Shantz, M., Kunz, P., Fay, G., Cheng, S., Fabian, T., and Partridge, C. The Mesicopter : A Miniature Rotorcraft Concept Phase II Final Report. Technical report, Stanford University, 2000.

Langkamp, D. S. *Quadrotor Flight Performance*. PhD thesis, Unviersity of Manchester, 2011.

Langkamp, D. S., Roberts, G., Scillitoe, A. D., Lunnon, I., Llopis Pascual, A., Zamecnik, J., Proctor, S., Rodriguez-Frias, M., Turner, M., Lanzon, A., Crowther, W. J., and Llopis-Pascual, A. An engineering development of a novel hexrotor vehicle for 3D applications. *... Micro Air Vehicles ...*, pages 32–39, 2011. URL http://repository.tudelft.nl/view/conferencepapers/uuid:d7bdec21-938d-426b-9553-59cf834e8061/.

Lei, Y., Ji, Y., and Wang, C. Numerical Simulation and Experimental Validation of Small-rotor Aerodynamic Characteristics. In *Proceedings of the 2016 International Conference on Mechatronics Engineering and Information Technology*, page 339, Paris, France, 1 2016. Atlantis Press. ISBN 978-94-6252-222-0. doi: 10.2991/icmeit-16.2016.11. URL http://www.atlantis-press.com/php/paper-details.php?id=25860409.

Leishman, J. G. The breguet-richet quad-rotor helicopter of 1907. *Vertiflite*, pages 1–4, 2002. URL http://aero.umd.edu/~leishman/Aero/Breguet.pdf.

Leishman, J. G. *Principles of helicopter aerodynamics*. Cambridge University Press, Cambridge, 2006.

Leishman, J. G. and Syal, M. Figure of merit definition for coaxial rotors. *Journal of the American Helicopter Society*, 53(3):290–300, 2008. ISSN 00028711. doi: 10.4050/JAHS.53.290.

Llopis Pascual, A. Carbon Air-Frame for Tumbleweed. Technical report, University of Manchester, 2011.

Martinez, V. *Modelling of the Flight Dynamics of a Quadrotor Helicopter*. PhD thesis, Cranfield University, 2007.

McVeigh, M. A., Grauer, W. K., and Paisley, D. J. Rotor/Airframe Interactions on Tiltrotor Aircraft. *Journal of the American Helicopter Society*, 35(3):43–51, 7 1990. ISSN 21616027. doi: 10.4050/JAHS.35.43. URL `http://www.ingentaconnect.com/content/ahs/jahs/1990/00000035/00000003/art00005http://openurl.ingenta.com/content/xref?genre=article&issn=2161-6027&volume=35&issue=3&spage=43`.

Ning, Z. and Hu, H. An Experimental Study on the Aerodynamics and Aeroacoustic Characteristics of Small Propellers. In *54th AIAA Aerospace Sciences Meeting*, pages 1–17, Reston, Virginia, 1 2016. American Institute of Aeronautics and Astronautics. ISBN 978-1-62410-393-3. doi: 10.2514/6.2016-1785. URL `http://arc.aiaa.org/doi/10.2514/6.2016-1785`.

Ning, Z. and Hu, H. An Experimental Study on the Aerodynamic and Aeroacoustic Performances of a Bio-Inspired UAV Propeller. In *35th AIAA Applied Aerodynamics Conference*, Reston, Virginia, 2017. American Institute of Aeronautics and Astronautics. ISBN 978-1-62410-501-2. doi: 10.2514/6.2017-3747. URL `https://arc.aiaa.org/doi/10.2514/6.2017-3747`.

Nowicki, N. Measurement and Modeling of Multicopter Uas Rotor Blade Deflection in Hover. Technical report, KTH - Royal Institute of Technology, 2016.

Otsuka, H. and Nagatani, K. Thrust loss saving design of overlapping rotor arrangement on small multirotor unmanned aerial vehicles. *Proceedings - IEEE International Conference on Robotics and Automation*, 2016-June:3242–3248, 2016. ISSN 10504729. doi: 10.1109/ICRA.2016.7487494.

Pounds, P., Mahony, R., Gresham, J., Corke, P., and Roberts, J. Towards Dynamically-Favourable Quad-Rotor Aerial Robots. In *Australasian Conference on Robotics and Automation*, 2004. doi: 10.1.1.124.8460.

Pounds, P., Mahony, R., and Corke, P. Modelling and control of a large quadrotor robot. *Control Engineering Practice*, 18(7):691–699, 2010. ISSN 09670661. doi: 10.1016/j.conengprac.2010.02.008. URL `http://dx.doi.org/10.1016/j.conengprac.2010.02.008`.

Pounds, P. E. I. *Design, Construction and Control of a Large Quadrotor Micro Air Vehicle*. PhD thesis, Australian National University, 2007.

Quinn, M. K. Particle Image Velocimetry, 2016.

Raffel, M., Bauknecht, A., Ramasamy, M., Yamauchi, G. K., Heineck, J. T., and Jenkins, L. N. Contributions of Particle Image Velocimetry to Helicopter Aerodynamics. *AIAA Journal*, pages 1–16, 2017. ISSN 0001-1452. doi: 10.2514/1.J055571. URL `https://arc.aiaa.org/doi/10.2514/1.J055571`.

Russell, C., Jung, J., Willink, G., and Glasner, B. Wind Tunnel and Hover Performance Test Results for Multicopter UAS Vehicles. *AHS International 72nd Annual Forum*, 2016. ISSN 15522938.

Salazar, S., Romero, H., Lozano, R., and Castillo, P. Modeling and Real-Time Stabilization of an Aircraft Having Eight Rotors. *Journal of Intelligent and Robotic Systems*, 54(1-3):455–470, 9 2008. ISSN 0921-0296. doi: 10.1007/s10846-008-9274-x. URL `http://link.springer.com/10.1007/s10846-008-9274-x`.

Schafroth, D. M. *Aerodynamics, modeling and control of an autonomous micro helicopter*. PhD thesis, ETH ZÜRICH, 2010. URL `http://e-collection.library.ethz.ch/view/eth:1573`.

Seddon, J. *Basic Helicopter Aerodynamics: First Edition*. BSP Professional Books, 1990. ISBN 0632020326.

Stepaniak, M. J. *A Quadrotor Sensor Platform*. PhD thesis, Ohio Unviersity, 2008.

Vulcan UAV Ltd, . VulcanUAV Airlift, 2017. URL `http://vulcanuav.com/aircraft/`.

Waslander, S. L., Hoffmann, G. M., and Tomlin, C. J. Multi-agent quadrotor testbed control design: integral sliding mode vs. reinforcement learning. *2005 IEEE/RSJ International Conference on Intelligent Robots and Systems*, pages 3712–3717, 2005. doi: 10.1109/IROS.2005.1545025. URL `http://ieeexplore.ieee.org/lpdocs/epic03/wrapper.htm?arnumber=1545025`.

Yeo, D., Shrestha, E., Paley, D. A., and Atkins, E. M. An Empirical Model of Rotorcrafy UAV Downwash for Disturbance Localization and Avoidance. In *AIAA Atmospheric Flight Mechanics Conference*, pages 1–14, Reston, Virginia, 1 2015. American Institute of Aeronautics and Astronautics. ISBN 978-1-62410-340-7. doi: 10.2514/6.2015-1685. URL `http://dx.doi.org/10.2514/6.2015-1685http://arc.aiaa.org/doi/10.2514/6.2015-1685`.

Yeo, D. W., Sydney, N., Paley, D. A., and Sofge, D. Downwash Detection and Avoidance with Small Quadrotor Helicopters. *Journal of Guidance, Control, and Dynamics*, 40(3):692–701, 3 2017. ISSN 0731-5090. doi: 10.2514/1.G001465. URL `http://arc.aiaa.org/doi/10.2514/1.G001465`.

Yoon, S., Lee, H. C., and Pulliam, T. H. Computational Analysis of Multi-Rotor Flows. In *54th AIAA Aerospace Sciences Meeting*, pages 1–11, Reston, Virginia, 1 2016. American Institute of Aeronautics and Astronautics. ISBN 978-1-62410-393-3. doi: 10.2514/6.2016-0812. URL `http://arc.aiaa.org/doi/10.2514/6.2016-0812`.

Zhou, W., Ning, Z., Li, H., and Hu, H. An Experimental Investigation on Rotor-to-Rotor Interactions of Small UAV Propellers. In *35th AIAA Applied Aerodynamics Conference*, pages 1–16, Reston, Virginia, 6 2017. American Institute of Aeronautics and Astronautics. ISBN 978-1-62410-501-2. doi: 10.2514/6.2017-3744. URL `https://arc.aiaa.org/doi/10.2514/6.2017-3744`.

Appendix A

MATLAB Code Listing

A.1 Run_Thrust_Test.m

Run_Thrust_Test is the overarching MATLAB script that manages each thrust testing run. The script loads the appropriate configuration files, iterates through the prescribed test points, and stores the acquired data.

```
%% Configuration
% Load in Labjack (DAQ) Configuration
configure_labjack;
global config_values;
% Load in data structure
load('library/Run_Data_Struct', 'RunData');
%% Run Details
Run_Name = '⟨Run ID⟩';
% Save Dir
save_dir = fileparts('⟨Save Directory⟩');
% Disk position data
RunData.Disk_1_Position = [⟨Disk X,Y location⟩];
```

```
RunData.Disk_1_Angle = ⟨Disk Angle⟩;
RunData.Disk_1_Pitch = ⟨Disk Pitch⟩;
RunData.Disk_2_Position = [⟨Disk X,Y location⟩];
RunData.Disk_2_Angle = ⟨Disk Angle⟩;
RunData.Disk_2_Pitch = ⟨Disk Pitch⟩;
% Run test - Iterating through test points
for i = 1:length(RunData.TestPoints)
    pwm_set(RunData.TestPoints(i,1),RunData.TestPoints(i,2));
    disp(sprintf('\n PWM Set %i, %i',...
        RunData.TestPoints(i,1),RunData.TestPoints(i,2)))
    if any(i == [0:28:448])
        pause(10)
    elseif any(RunData.TestPoints(i,:) == 0)
        pause(5)
    else
        pause(1);
    end
    [data,rpm] = Loadcell_Capture(1);
    RunData.Disk_1_Raw(:,:,i) = data(:,1:9);
    RunData.Disk_2_Raw(:,:,i) = data(:,10:18);
    RunData.Counter_RPM(i,:,1) = rpm(1,:);
    RunData.Counter_RPM(i,:,2) = rpm(2,:);
    disp(sprintf('\n Test point %i complete', i))
end
pwm_set(0,0);
%% Output data
```

```
eval([Run_Name '_Data = RunData;'])
savefile = fullfile(save_dir, [Run_Name '_Data.mat']);
save(savefile, [Run_Name '_Data']);
```

A.2 configure_labjack.m

The configure_labjack.m function configures the LabJack correctly for the data acquisition. This includes configuring the acquisition stream, RPM counters, and PWM generation settings. Whilst these settings can be stored internally on the LabJack, the function is called at the start of every test to ensure all settings are correct.

```
function [ ] = configure_labjack()
% Set up LJM Environment
ljmAsm = NET.addAssembly('LabJack.LJM'); %Make the LJM .NET assembly visible in MATLAB
t = ljmAsm.AssemblyHandle.GetType('LabJack.LJM+CONSTANTS');
LJM_CONSTANTS = System.Activator.CreateInstance(t); %creating an object to nested class LabJack.LJM.CONSTANTS
% Initalise LabJack handle
global handle
handle = 0;

% Connect to LabJack (defined by IP address) and configure RPM counters and PWM outputs
try
    [ljmError, handle] = LabJack.LJM.OpenS('T7', 'Ethernet', '⟨IP_Address⟩', handle);

    % Configure stream settings
    LabJack.LJM.eWriteName(handle, 'STREAM_BUFFER_SIZE_BYTES', 32768);
```

```
    LabJack.LJM.eWriteName(handle, 'AIN_ALL_RANGE', 10);
    LabJack.LJM.eWriteName(handle, 'STREAM_RESOLUTION_INDEX', 1);
    LabJack.LJM.eWriteName(handle, 'STREAM_SETTLING_US', 5);

    % Configure Clock0 for RPM counters
    LabJack.LJM.eWriteName(handle, 'DIO_EF_CLOCK1_ENABLE', 0);
    LabJack.LJM.eWriteName(handle, 'DIO_EF_CLOCK1_DIVISOR', 1);
    LabJack.LJM.eWriteName(handle, 'DIO_EF_CLOCK1_ROLL_VALUE', 0);
    LabJack.LJM.eWriteName(handle, 'DIO_EF_CLOCK1_ENABLE', 1);

    % Cycle FIO0 and FIO1 for RPM counters
    LabJack.LJM.eWriteName(handle, 'DIO0_EF_ENABLE', 0);
    LabJack.LJM.eWriteName(handle, 'DIO0_EF_INDEX', 11);
    LabJack.LJM.eWriteName(handle, 'DIO0_EF_CONFIG_A', 11);
    LabJack.LJM.eWriteName(handle, 'DIO1_EF_ENABLE', 0);
    LabJack.LJM.eWriteName(handle, 'DIO1_EF_INDEX', 11);
    LabJack.LJM.eWriteName(handle, 'DIO1_EF_CONFIG_A', 11);

    % Configure Clock1 for PWM outputs
    LabJack.LJM.eWriteName(handle, 'DIO_EF_CLOCK2_ENABLE', 0);
    LabJack.LJM.eWriteName(handle, 'DIO_EF_CLOCK2_DIVISOR', 64);
    LabJack.LJM.eWriteName(handle, 'DIO_EF_CLOCK2_ROLL_VALUE',
       50000);
    LabJack.LJM.eWriteName(handle, 'DIO_EF_CLOCK2_ENABLE', 1);

    % Configure PWM output on FIO2
```

```
    LabJack.LJM.eWriteName(handle, 'DIO2_EF_ENABLE', 0);
    LabJack.LJM.eWriteName(handle, 'DIO2_EF_INDEX', 0);
    LabJack.LJM.eWriteName(handle, 'DIO2_EF_OPTIONS', 2);
    LabJack.LJM.eWriteName(handle, 'DIO2_EF_CONFIG_A', 0);
    LabJack.LJM.eWriteName(handle, 'DIO2_EF_ENABLE', 1);
    % Configure PWM output on FIO3
    LabJack.LJM.eWriteName(handle, 'DIO3_EF_ENABLE', 0);
    LabJack.LJM.eWriteName(handle, 'DIO3_EF_INDEX', 0);
    LabJack.LJM.eWriteName(handle, 'DIO3_EF_OPTIONS', 2);
    LabJack.LJM.eWriteName(handle, 'DIO3_EF_CONFIG_A', 0);
    LabJack.LJM.eWriteName(handle, 'DIO3_EF_ENABLE', 1);

catch
    showErrorMessage(e)
end
try
    LabJack.LJM.Close(handle);
catch
    showErrorMessage(e)
end

% Load in Calibration Constants
⟨Cal_1⟩ = [⟨Calibration Matrix⟩];
⟨Cal_2⟩ = [⟨Calibration Matrix⟩];
⟨Cal_3⟩ = [⟨Calibration Matrix⟩];

```

```
global config_values;
config_values.⟨Cal_1⟩ = ⟨Cal_1⟩;
config_values.⟨Cal_2⟩ = ⟨Cal_2⟩;
config_values.⟨Cal_3⟩ = ⟨Cal_3⟩;
end
```

A.3 Loadcell_Capture.m

The Loadcell_Capture function manages the LabJack data acquisition system and returns the acquired data to Run_Thrust_Test.m. The function acquires load cell, current sensor, voltage, and RPM data. Data sampling rate is defined inside the function, however the acquisition period is passed to the function when called.

```
function [output, rpm] = Loadcell_Capture( timeperiod )
ljmAsm = NET.addAssembly('LabJack.LJM');
t = ljmAsm.AssemblyHandle.GetType('LabJack.LJM+CONSTANTS');
LJM_CONSTANTS = System.Activator.CreateInstance(t); %creating an object to nested class LabJack.LJM.CONSTANTS
dispErr = true;
global handle
try
    [ljmError, handle] = LabJack.LJM.OpenS('T7', 'ETHERNET', '192.168.1.201', handle);
    LabJack.LJM.eWriteName(handle, 'DIO0_EF_ENABLE', 1);
    LabJack.LJM.eWriteName(handle, 'DIO1_EF_ENABLE', 1);
    maxRequests = timeperiod*10; %
    numAddresses = 18;
    aScanListNames = NET.createArray('System.String', numAddresses);
    % Loadcell SG1
    aScanListNames(1) = 'AIN48';
    aScanListNames(2) = 'AIN49';
    aScanListNames(3) = 'AIN50';
```

```
aScanListNames(4) = 'AIN51';
aScanListNames(5) = 'AIN52';
aScanListNames(6) = 'AIN53';
% Loadcell SG2
aScanListNames(10) = 'AIN96';
aScanListNames(11) = 'AIN97';
aScanListNames(12) = 'AIN98';
aScanListNames(13) = 'AIN99';
aScanListNames(14) = 'AIN100';
aScanListNames(15) = 'AIN101';
% Power
aScanListNames(7) = 'AIN120';       % Current 1
aScanListNames(16) = 'AIN121';      % Current 2
aScanListNames(8) = 'AIN122';       % Voltage 1
aScanListNames(17) = 'AIN123';      % Voltage 2
% Rippems
aScanListNames(9) = 'AIN124';       % RPM 1
aScanListNames(18) = 'AIN125';      % RPM 2
aScanList = NET.createArray('System.Int32', numAddresses);
aTypes = NET.createArray('System.Int32', numAddresses);
LabJack.LJM.NamesToAddresses(numAddresses, aScanListNames,
    aScanList, aTypes);
scanRate = double(5000);
scansPerRead = int32(scanRate/10);
aData = NET.createArray('System.Double', numAddresses*
    scansPerRead);
```

```
    %Configure the negative channels for single ended readings.
    aNames = NET.createArray('System.String', numAddresses);
    aValues = NET.createArray('System.Double', numAddresses);
    for i=1:numAddresses,
        aNames(i) = [char(aScanListNames(i)) '_NEGATIVE_CH'];
    end
    aValues = double([56 57 58 59 60 61 199 199 199 104 105 106 107
         108 109 199 199 199]);
    LabJack.LJM.eWriteNames(handle, numAddresses, aNames, aValues,
       0);
    try
        [ljmError, scanRate] = LabJack.LJM.eStreamStart(handle,
            scansPerRead, numAddresses, aScanList, scanRate);
    catch e
        showErrorMessage(e)
    end
    pause(0.1)
    try
        output = zeros(1,numAddresses);
        period = 0;
        for i=1:maxRequests,
            [ljmError, deviceScanBacklog, ljmScanBacklog] = LabJack
                .LJM.eStreamRead(handle, aData, 0, 0);
            [ljmerror, period] = LabJack.LJM.eReadName(handle, '
                DIO0_EF_READ_A_F', period);
            rpm(1,i) = 1/period*60;
```

```
            [ljmerror, period] = LabJack.LJM.eReadName(handle, '
               DIO1_EF_READ_A_F', period);
            rpm(2,i) = 1/period*60;
            output = vertcat(output, reshape(double(aData),
               numAddresses, [])');
        end
        output(1,:) = [];
    catch e
        showErrorMessage(e)
    end
    LabJack.LJM.eWriteName(handle, 'DIO0_EF_ENABLE', 0);
    LabJack.LJM.eWriteName(handle, 'DIO1_EF_ENABLE', 0);
    LabJack.LJM.eStreamStop(handle);
catch e
    if dispErr
        showErrorMessage(e)
    end
end
try
    % Close handle
    LabJack.LJM.Close(handle);
catch e
    showErrorMessage(e)
end
end
```

A.4 pwm_set.m

The pwm_set.m function generates the PWM signal required to control the ESCs, based on the values passed to the function when called.

```
function [ period ] = pwm_set( pwm1, pwm2 )
ljmAsm = NET.addAssembly('LabJack.LJM'); %Make the LJM .NET assembly visible in MATLAB
t = ljmAsm.AssemblyHandle.GetType('LabJack.LJM+CONSTANTS');
LJM_CONSTANTS = System.Activator.CreateInstance(t); %creating an object to nested class LabJack.LJM.CONSTANTS
period(1) = 0;
global handle
[ljmError, handle] = LabJack.LJM.OpenS('T7', 'ETHERNET', '192.168.1.201', handle);
pwm(1) = 250*((pwm1/2)+5);
LabJack.LJM.eWriteName(handle, 'DIO2_EF_CONFIG_A', pwm(1));
if exist('rpm2')
    period(2) = 0;
    pwm(2) = 250*((pwm2/2)+5);
    LabJack.LJM.eWriteName(handle, 'DIO3_EF_CONFIG_A', pwm(2));
end
LabJack.LJM.Close(handle);
end
```